Understanding and Predicting Temperatures in Municipal Solid Waste Landfills

Morton A. Barlaz[a], Zisu Hao[a], Craig H. Benson[b], Marco J. Castaldi[c], Joel Ducoste[a], and Scott Luettich[d]

a. Department of Civil, Construction, and Environmental Engineering, North Carolina State University, Raleigh, NC 27695; 919-515-7212; barlaz@ncsu.edu

b. School of Engineering, University of Virginia, Charlottesville, VA 22904

c. Chemical Engineering Department, The City College of New York, City University of New York, New York, NY 10031

d. Geosyntec Consultants, 289 Great Rd, Suite 202, Acton, MA 01720

KEYWORDS: elevated temperature landfills, heat, chemical processes, biological processes.

FINAL REPORT

Prepared for the

Environmental Research and Education Foundation

2022

I. Executive Summary

The overall objective of this study was to develop a comprehensive understanding of heat generation, release and accumulation in municipal solid waste (MSW) landfills so to understand and explain why some landfills accumulate excessive heat. The research included several interrelated components including (1) development of a mathematical model to describe heat generation, release and accumulation in landfills, (2) process research on thermochemical reactions that may occur in MSW at elevated temperatures, (3) research to quantify the thermal properties of MSW, and (4) a review of field instrumentation that has been used successfully to monitor temperatures in full-scale landfills.

Two predictive models were developed, a batch reactor model that treats a landfill as a uniform waste mass, and a three-dimensional finite element model (FEM-3DM) that better represents an actual landfill by incorporating a waste placement strategy and schedule, waste heterogeneity, boundary conditions, fluid flow, and physical, chemical and biological heat sources and sinks. The batch reactor model showed that the presence of ash and aluminum (Al) have the potential to contribute significantly to heat accumulation in landfills and also identified areas where additional research was needed to understand ash and Al behavior in landfills, an area where there is almost no experience (Figure ES-1).

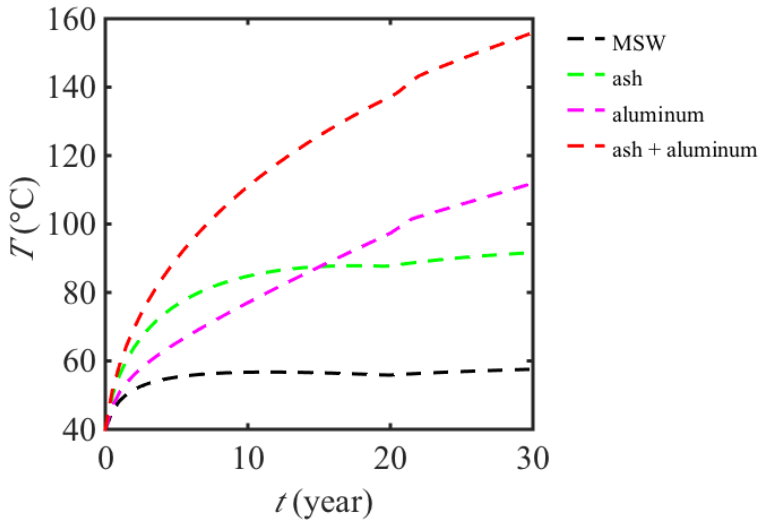

Figure ES-1 Batch reactor model simulations that show the importance of Al corrosion reactions and ash hydration and carbonation. Simulations assume 20% ash at 19% Ca, and the presence of 1.7% Al in MSW.

The FEM-3DM documented the impact of landfill height on heat retention and was able to predict the convex temperature depth profile that has been observed in ETLFs (Figure ES-2). The impacts of waste composition and disposal strategies were quantified using the cumulative normalized landfill volume (CNLV). The CNLV is the volume of the landfill with a temperature exceeding a given value. Here, temperatures greater than 65 and 80 °C were considered (Table ES-1). Simulations included the impacts of segregated ash disposal in the corner or center of a landfill as well as mixing the ash and evenly distributing it with the municipal solid waste (MSW). Simulations showed that a smaller fraction of the MSW

mass is impacted when ash is segregated within an MSW landfill. The CNLV of the ash-in-center scenario is slightly greater than that of the ash-in-corner scenario, indicating that the corner scenario has a smaller elevated temperature region. However, differences are small enough that other operational factors will likely influence the location of ash disposal.

The decrease in CNLV from hydration and carbonation to the carbonation only scenarios suggests that pre-hydrating ash (prior to disposal) is one approach to reduce the energy in the ash. In fact, ash may be wet before leaving the point of generation in which case some or all hydration will occur prior to burial. For the cases with reactive waste evenly distributed in landfills, the CNLV > 65 ℃ is significantly greater than ash-in-center and ash-in-corner scenarios. When the concentration of reactive waste is relatively low (10% ash and 1.7% Al), the CNLVs > 80 ℃ are close to 0. However, when these waste disposal quantities are doubled, there is a marked increase in CNLV.

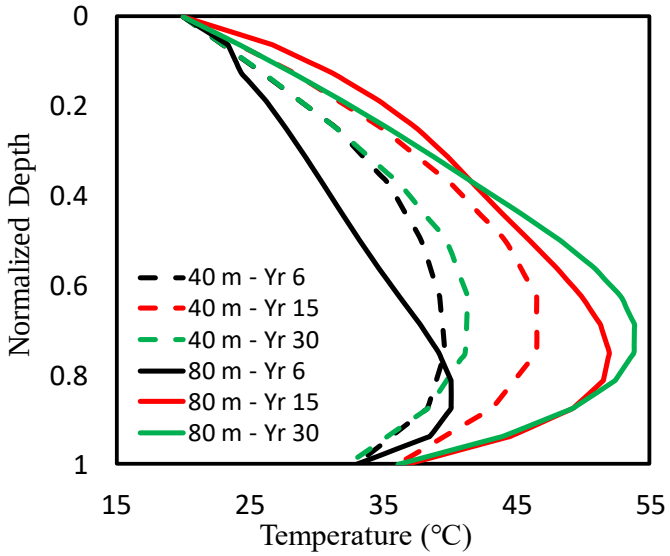

Figure ES-2. Temperature profiles for 40 m and 80 m high landfills show that more heat is retained n the deeper landfill.

Table ES-1. Cumulative normalized landfill volume (CNLV) with temperatures greater than 65 and 80 ℃ and maximum temperature at waste bottom zone in Year 20

Case	CNLV > 65 ℃	CNLV > 80 ℃	Max T at waste bottom (℃)
MSW only	0	0	37
ash-in-center[a]	0.07	0.05	139
ash-in-corner[a]	0.06	0.04	173
ash-in-center[a] **(carbonation only)**	0.03	0.02	85
10% ash	0.47	0	49
20% ash[a]	0.81	0.63	65
1.7% Al[a]	0.59	0	54
3.4% Al[a]	0.86	0.71	86

a. For the ash-in-center and ash-in-corner scenarios, the ash comprises 2.3% of the total landfill volume and is segregated. For the 10 and 20% ash and the 1.7 and 3.4% aluminum cases, the waste is uniformly mixed with MSW in the landfill. The CNLVs are thus not comparable but each case represents hypothetical landfill practice

The models have been used to assist EREF stakeholders with the development of waste acceptance strategies such that appropriate quantities of heat-generating wastes can be accepted in consideration of heat accumulation. The model also showed the benefits of hydrating ash before burial in a landfill to eliminate the heat of hydration. This led to a field-test of this concept in which the landfill and combustion industries worked together to evaluate operational aspects of ash hydration prior to burial. By allowing ash to remain above ground for ~60 days, considerable ash carbonation occurred prior to burial, further reducing the release of heat from ash after burial.

The process research on thermal reactions showed that the primary gas ratio (CH_4/CO_2) changes under elevated conditions in the absence of biological activity, although it was unclear whether the change was due to CH_4 consumption, CO_2 production or both, and the reaction mechanism(s) were not clear. In addition, H_2, CO and volatile organics were produced in MSW at elevated temperatures under abiotic conditions, though here too, the mechanism could not be elucidated from the available data. Tests conducted at atmospheric and at elevated pressure (382 kPa) showed greater H_2 production at elevated pressure. This research also demonstrated the charring of wood in an anoxic reactor at temperatures below 120 °C. The energetics that were observed in the reactor experiments suggest that exothermic reactions may occur in ETLFs, but they are modest. Thus, other sources of energy likely are responsible for heat accumulation leading to elevated temperatures in ETLFs.

Research on the thermal properties of MSW was conducted to provide the engineering community with a method to estimate thermal properties for use in models like those developed in this study. Thermal properties of fresh and decomposed MSW were measured at gravimetric water contents of 6, 25, 45, 60% water content and confining stresses ranging from 2 to 400 kPa to systematically evaluate how thermal properties vary within a landfill and throughout the landfill lifecycle. Both fresh and decomposed MSW were tested to brackets the range of waste decomposition status. A synthetic MSW was used for this work and a decomposed sample was generated by incubation of the synthetic MSW in laboratory

reactors. Thermal conductivity was measured using a guarded hot-plate apparatus and specific heat capacity was measured using a dual-needle probe.

Thermal conductivity of the waste increased with an increase in water content and with higher overburden stress, the latter contributing to higher dry unit weight. Thermal conductivity of the decomposed waste was comparable to or slightly higher than the thermal conductivity of fresh waste under similar conditions, largely due to loss of food waste with low thermal conductivity during decomposition. The specific heat capacity of the waste was larger at higher water content due to the higher specific capacity of the water phase. The results indicated that waste deeper in a landfill is expected to be more thermally conductive than shallower waste.

The efficacy of geometric mean and mixing models to predict thermal conductivity was assessed. Similar comparisons were made between specific heat capacity predicted with a mass-weighted model and measured specific heat capacities. Thermal conductivity was under-predicted by the geometric-mean thermal conductivity model. The mixing model over-predicted thermal conductivities modestly in the low range, and was essentially unbiased in the high thermal conductivity range. The mass-weighted model predicted specific heat capacity accurately. The mixing model is recommended for predicting thermal conductivity in practice while the mass-weighted model is recommended for predicting specific heat capacity.

Experience with field instrumentation demonstrated that fiber optic distributed temperature sensing (FODTS) systems are effective for the continuous monitoring of waste temperatures with 0.25-m vertical resolution. When combined with the use of vibrating-wire (VW) transducers to measure in-situ pressure, a landfill operator can obtain a 3-dimensional picture of landfill temperature and pressure, and how the landfill is changing with time. Primary gas ratio (CH_4/CO_2) data, coupled with temperature and pressure data, can be valuable for identifying heat sources, visualizing how the heat is distributed throughout the landfill, assessing how the distribution of temperatures within the landfill changes with time, evaluating stability, and understanding inhibition of gas collection

The research also resulted in some more general findings. The research team emphasized the importance of (1) reviewing landfill monitoring data for trends that suggest the potential for widespread elevated temperatures and (2) aggressive management of liquids and gases. Liquid accumulation results in elevated hydrostatic pressure that is reported to increase the energetics of pyrolytic reactions. While the impact of increased pressure on thermal reactions could not be quantified, high hydrostatic pressure may also result in leachate seeps and flooded gas wells, both of which interfere with good management practice. Gases serve as volatile substrates for heat-generating reactions. Extracting gas aggressively removes a potential energy source in a landfill undergoing thermal abiotic reactions.

While the initial hypothesis focused on a trigger causing a self-propagating exothermic reaction, the findings of this study suggest that heat generating wastes can result in elevated temperatures and likely are the primary cause of ETLFs. For example, the modeling work highlighted the potential of ash, a waste commonly accepted in MSW landfills, as a heat source that could result in elevated temperatures similar to those observed in ETLFs. Strategies are needed to safely dispose of heat-generating waste based on the reactivity of the waste and the relative quantity disposed

II. Table of Contents

III. Introduction

Several municipal solid waste (MSW) landfills have been experienced temperatures in excess of 80 − 100°C over the last 15 yr without combustion occurring (Calder and Stark 2010, Luettich and Yafrate 2016, Benson 2017, Jafari et al. 2017). This is well above temperatures commonly associated with MSW landfills, which typically range between 40 and 65 °C and generally are less than 55 °C (Hanson et al. 2010, Yesiller et al. 2015). Landfills exhibiting elevated temperatures over a large surface area are now being referred to as elevated temperature landfills (ETLFs).

In some cases, elevated temperatures have resulted in damage to the landfill's gas collection system, rapid settlement with subsequent implications for the integrity of the landfill cover and slope stability, elevated leachate volume and strength, reduced methane content that may impact landfill gas treatment and energy generation processes, odorous gases, and/or challenges with regulatory compliance (Li et al. 2011, Benson 2017 Jafari et al. 2017). In cases where the elevated temperature extends to the bottom of the landfill, there may also be impacts on the service life of the geomembrane liner. Consequently, ETLFs often require increased monitoring and management. While some ETLF owners have acknowledged receipt of reactive wastes that are a source of excessive heat, other owners are unaware of the burial of such wastes. Moreover, there was considerable uncertainty as to the mechanisms controlling heat accumulation in landfills when this project was initiated.

A number of heat-generating reactions occur when MSW and other non-hazardous wastes are buried in landfills. Reactions include both aerobic and anaerobic biodegradation (Li et al. 2011, Grillo 2014), anaerobic metal corrosion (Calder and Stark 2010), and acid-base neutralization (Rees 1980). Some landfills accept ash from the combustion of coal, MSW, or other carbonaceous materials. Fly ash typically contains oxides (e.g., CaO) that undergo both hydration and carbonation reactions (Speiser et al. 2000, Li et al. 2007). While not documented in landfills, there are reports of thermochemical (pyrolytic) reactions in biomass (Kwon and Castaldi 2012, Ciuta et al. 2014). Pyrolytic reactions may occur in landfills at elevated but as yet undefined temperatures. While the aforementioned reactions generate heat in landfills, understanding the extent to which heat accumulates is critical.

The overall objective of this study was to develop a comprehensive understanding of heat generation, release, and accumulation in landfills to understand and explain why some landfills accumulate excessive heat. The research included several interrelated components, all focused on the overall objective. These components are described individually in the Results section and include (1) the development of a mathematical model to describe heat generation, release and accumulation in MSW landfills, (2) process research on thermochemical reactions that may occur in MSW at elevated temperatures, (3) research to quantify the thermal properties of MSW, and (4) a review of field instrumentation that has been used successfully to monitor temperatures in full-scale MSW landfills. While this last component was not part of the original scope, knowledge of instrumentation became invaluable when considering theory and field observations.

IV. Results and Discussion

The Results and Discussion are organized into four sections including model development and implementation, the role of thermochemical reactions in MSW, thermal properties of MSW, and field instrumentation.

A. Model Development

Landfills are complex engineered systems in which multiple processes that contribute to heat generation, removal and accumulation occur concurrently. As result, quantitatively relating anecdotal field observations to causation with respect to heat accumulation is difficult. A model of heat generation, removal, and accumulation serves to clearly identify all relevant processes and to describe them mathematically. This has the advantages of (1) identifying the extent to which a process is well-understood and (2) evaluating the potential significance of a process. For example, the process of anaerobic metal corrosion is well known and the relevant stoichiometry is given in the Methods section. However, the rate and extent to which aluminum (Al) and iron (Fe) corrode under environmental conditions that are relevant to landfills, the form of a rate equation, appropriate rate constant(s) and the impact of different alloys of these metals on corrosion rates are unknown. Through the process of model development, the level of understanding of each heat generating process is defined.

A batch reactor model was initially developed. The batch reactor model is relatively simple and as is the case with all models, there is a tradeoff between simplicity and the extent to which the model represents a landfill. In the batch reactor model, a mass of MSW is buried initially and allowed to decompose over time. The buried MSW is assumed to be perfectly mixed such that temperatures throughout the buried waste mass are uniform and there is not a temperature gradient or a need to define external boundary conditions. Despite these limitations, as described below, the batch reactor model proved useful in the incorporation of all relevant biological and chemical reactions and in identifying chemical processes that could serve as important sources of heat generation in landfills. The batch reactor model is described in the first subsection.

With the batch reactor model as a foundation, a finite element three-dimensional model (FEM-3DM) was developed. The FEM-3DM was used to simulate the filling of a landfill over time and the burial of different wastes in different locations at different times, e.g., layer(s) of ash of defined thickness(es) in specific location(s) in a landfill. The FEM-3DM includes temperature gradients within the landfill and boundary conditions.

Prior to starting any model development, a review of all published models that describe any aspect of heat generation was developed. This review is presented as Appendix Table A1. As expected, published models did not consider abiotic reactions including metal corrosion, acid-base neutralization, ash hydration and carbonation, or pyrolysis. In addition, many of the models incorporate complex descriptions of biological processes (El-Fadel et al. 1996a, Garg and Achari 2010, White et al. 2004, Fytanidis and Voudrias 2014). While mechanistically accurate, detailed parameterization of biological processes in a landfill context is difficult, adds uncertainty and was judged unnecessary for this research. A second limitation of the aforementioned models is that they neglect other heat flows including the evaporation of water that saturates landfill gas, and moisture condensation.

1. Batch Reactor Model Simulations

The development of a mathematical model to predict temperature impacts associated with a number of biological and chemical reactions that may occur in MSW landfills is described in this section. Modeled heat sources include aerobic and anaerobic biological reactions, anaerobic metal corrosion, acid-base reactions, and ash hydration and carbonation. The model includes convective heat transport and removal mechanisms, including heat that is removed due to leachate collection, gas extraction, and evaporation. The governing equations for each heat source and sink are described in the Methods and the results of selected model simulations are presented in this section. Complete results including sensitivity analysis have been published (Hao et al. 2017).

A number of model simulations were run to individually explore the impacts of aerobic and anaerobic biodegradation only, ash hydration and carbonation, Al and Fe corrosion, acid-base neutralization reactions, and the incorporation of a hypothesized pyrolysis reaction. Simulations were conducted with and without consideration of heat loss via evaporation, convection of landfill gas out of the landfill, and cooling associated with infiltration. While these heat loss processes occur in landfills, they may not be perfectly efficient due to accumulated water and flooded gas wells. Thus, results for an actual landfill are likely bracketed by model simulations with and without heat loss. In addition, conductive heat loss could not be considered in a batch reactor model because the landfill is modeled as a uniform waste mass with no temperature gradients.

Simulations of heat generation due to aerobic and anaerobic biodegradation of MSW are presented in Figure 4-1 which is described as a base case. As described above, simulations were conducted with and without consideration of heat loss processes and simulations without heat loss represent an upper bound. The 2% N_2 cases translates to the availability of ~0.5% O_2. In the base case, the assumed air intrusion results in a ~1 °C increase relative to the temperature resulting from anaerobic decomposition only. When gas collection and leachate removal are the only heat removal processes, the model predicts a slight temperature decrease relative to no heat loss. Similarly, the heat loss due to evaporation is relatively low because temperature inhibition of biological gas production reduces evaporative heat loss. In the absence of the temperature inhibition term, evaporative heat loss dominates (data not shown). When infiltration is added as a heat sink, the temperature decrease between years 12 and 20 reflects heat loss associated with the infiltration of cooler water and leachate removal from the system. The temperature increase after year 20 is due to the assumed placement of a final cover with the subsequent cessation of infiltration and leachate removal, and the dynamic equilibrium between heat generation from biodegradation and heat removal processes.

When the infiltration rate was increased by 50% relative to the base case, there is some additional cooling and the effect is most pronounced between years 10 and 20 at which time infiltration is constant but heat generation from biodegradation is decreasing. The case of evaporation plus convection is also a case of no infiltration (e.g., arid conditions) and the maximum temperature difference between no infiltration and infiltration at 150% of the base case infiltration rate is ~8 °C.

When the CH_4 generation rate constant is doubled, the predicted temperature is most sensitive to the rate about 5 years after waste burial at which time methane generation is not completely inhibited due to high temperature.

As noted above, aerobic decomposition was considered based on a user-specified N_2 concentration in LFG and calculation of the available O_2 from the ratio of O_2 to N_2 in air. In additional work, we compared the temperature increase due to the consumption of either CH_4 or cellulose as the biodegradable substrate. The difference was less than 0.6°C and cellulose was adopted as the substrate for aerobic biodegradation.

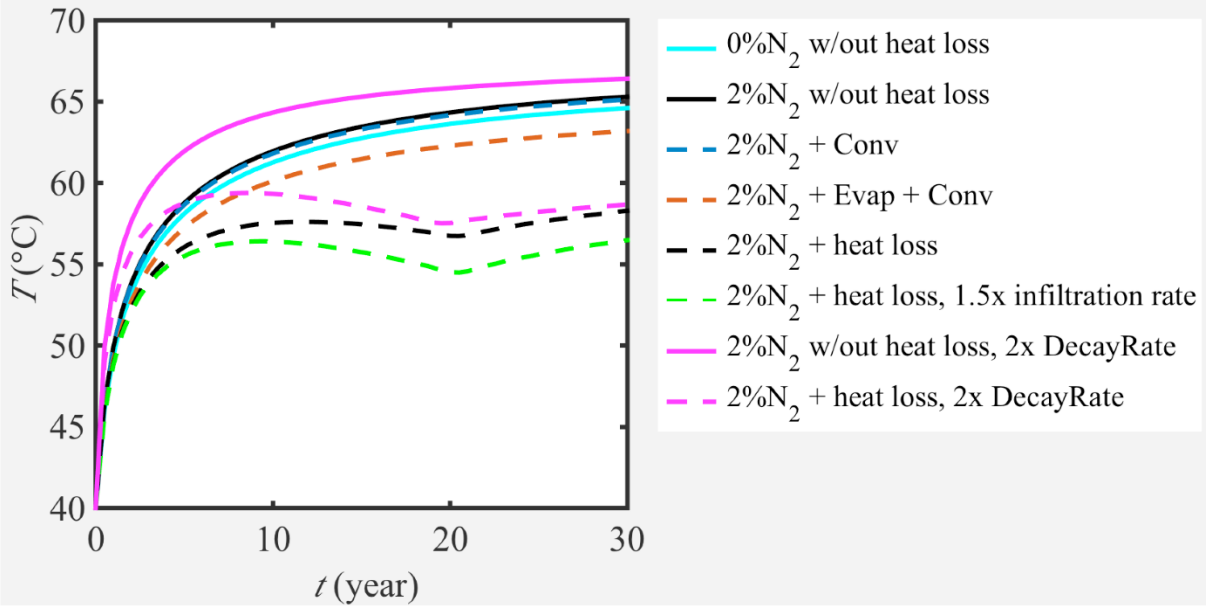

Figure 4-1. Heat accumulation associated with MSW biodegradation in the presence and absence of O_2. Solid lines represent cases without heat removal. Dashed lines consider heat removal process (Conv = convection, Evap = evaporation, heat loss = evaporation + convection + infiltration), 2x Decay Rate = decay rate constant doubled for each biodegradable component.

Multiple simulations were conducted to build on the base case and the most important results are summarized in Figure 4-2 which presents selected results of simulations with ash, aluminum and ash plus aluminum. Acid base reactions and Fe corrosion were also considered, but their impacts on heat generation were negligible so they are not discussed here. In addition, simulations were done based on a hypothesized pyrolysis reaction. However, there is so much uncertainty associated with the level of heat that could be released from exothermic pyrolysis that these results are not presented in this section. Addition discuss of pyrolysis is presented in the following section of the Results.

With reference to Figure 4-2, all results include heat loss and the MSW only base case reaches a temperature of about 58 °C. The addition of 20% ash with a Ca content of 19%, with the Ca assumed to be in the form of CaO results in a maximum temperature of about 90 °C while the presence of 1.7% Al results in a temperature of about 115 °C. The results in Figure 4-2 indicate that reactions that involve ash hydration plus carbonation as well as

Al corrosion can results in significant (32 – 57 ℃) heat accumulation relative to a case with MSW only and 2% N_2 in LFG. There are of course many variables that affect these results, examples of which include (1) the mass of ash disposed, (2) the actual % Ca in the ash which is material specific, (3) whether the ash is hydrated before it is buried in which case only the heat of carbonation would be released in the landfill, (4) the actual reactivity of Al in a landfill which will be a function of the form of Al (sheet vs foil) and the specific alloy, and (5) the form of the governing rate equation and kinetic constants for each reaction. Thus, the impacts of ash and Al as opposed to the precise temperature predictions are the most important results of the batch reactor model simulations.

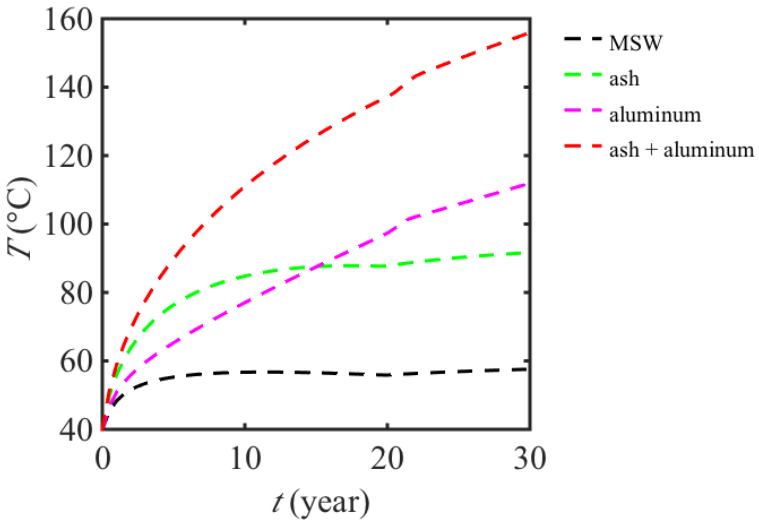

Figure 4-2 Batch reactor model simulations that show the importance of Al corrosion reactions and ash hydration and carbonation. Simulations assume 20% ash at 19% CaO, and the presence of 1.7% Al in MSW.

The batch reactor model showed that the presence of ash and Al have the potential to contribute significantly to heat accumulation in landfills. This finding stimulated considerable additional research including an additional EREF-funded project to evaluate the rate of hydration, carbonation and metal corrosion under landfill-relevant conditions, we well as field tests in which the landfill and combustion industries worked together to evaluate operational aspects of ash hydration prior to burial (results presented at 2020 GWMS).

The batch reactor model is not without limitations. Specifically, the model does not represent an actual landfill in several respects including (1) landfills fill over time as opposed to all at once, (2) boundary conditions, which cannot be incorporated into a batch reactor model, result in conductive heat loss, (3) waste composition varies with time and subsequently with space in a landfill. These limitations and others stimulated the next step in the overall research program which was to develop a transient three-dimensional finite element model (FEM-3DM) to better represent an actual landfill. Results from FEM-3DM simulations are described in the following section.

2. Finite Element Model Simulations

To represent the temperature distribution and evolution in landfills, a transient FEM-3DM was developed by incorporating waste placement strategy, waste heterogeneity, boundary conditions, fluid flow, and physical, chemical and biological heat sources and sinks. A manuscript documenting model development and simulation results has been submitted for publication and the citation will be updated before this report is finalized (Hao et al., 2020).

Heat generation and accumulation for a "base case" with biological reactions only are described first, followed by sensitivity analyses for the evaluation of the impacts of boundary conditions, landfill height, and biodegradation rates. Next, heat accumulation and propagation for scenarios in which ash buried in the center and corner of a landfill are compared, followed by simulations with evenly distributed ash-MSW or Al-MSW mixtures. Finally, model simulations and published field temperature data are compared.

Model simulations for the MSW only base case are presented in Figure 4-3. In contrast to batch reactor simulations, LFG was assumed to contain 4% N_2 for FEM-3DM simulations based on stakeholder input. Results show that the temperature at the top of the landfill is always cooler than at the center and bottom boundary. The maximum temperature increases over time in response to the biological reactions and reduced heat loss as the landfill fills. A temperature gradient forms from the center to the top of the landfill, indicating heat loss due to conduction. The maximum temperature in Year 15 is ~50 °C (Figure 4-3c), which is within the reported temperature range of actual landfills (Hanson et al., 2010). The center-to-top temperature gradient increases with increasing center temperatures. The center-to-side and center-to-bottom temperature gradients are lower due to the convective heat transfer from the top surface to the environment. By Year 30 (Figure 4-3d), the maximum predicted temperature has increased to ~55 °C at a depth of 50 m. Biological heat production is reduced based on temperature inhibition above 50 °C (inhibition function described in the Methods) so the anaerobic biodegradation rate decreases with time.

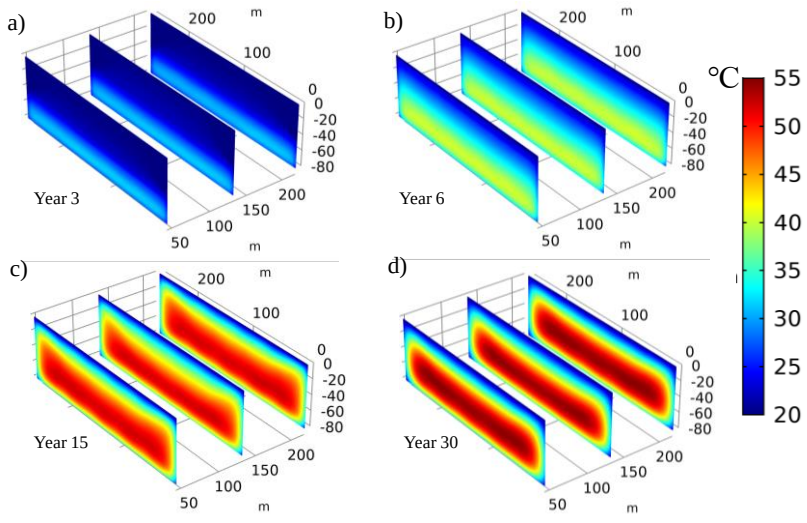

Figure 4-3. Temperature contours for a landfill receiving MSW only at Years 3, 6, 15 and 30 in parts a, b, c and d, respectively.

Simulated center and edge temperature profiles for the MSW only case are shown in Figure 4-4. The temperature decreases from 70 to 80 m due to the impacts of conductive heat transfer at the bottom boundary. From Years 6 to 20, the maximum temperature increases from 35 to 40 ℃, indicating that the biotic heat generation rate is greater than the heat loss rate. In addition, a convex temperature profile forms and the maximum temperature occurs at a depth of 50 m. A similar profile has been observed in a number of field studies (Yoshida et al., 1997; Hanson et al., 2010; Yeşiller et al., 2015; Jafari et al., 2017), suggesting heat accumulation in the center of landfills and conductive/convective heat loss from the top and bottom boundaries. The temperature increase is sustained from Years 6 to 20, followed by a decrease due to the modeled asymptotic decrease in substrate consumption and gas production. The maximum temperatures in the center of the landfill are 15 ℃ (Year 20) higher than temperatures on the edge due to the impact of conductive heat transfer at the side boundaries (Figure 4-4). In actual landfills, some fraction of the landfill sides will be above the surface which will result in increased heat loss. Moreover, the temperature profiles in Years 30 and 20 are close (Figure 4-4b), indicating that heat generation and loss are balanced in the center of the landfill over this time period. Figure 4-4 illustrates the extent to which the heat loss rate in the center of the landfill is lower than the rate at the edge.

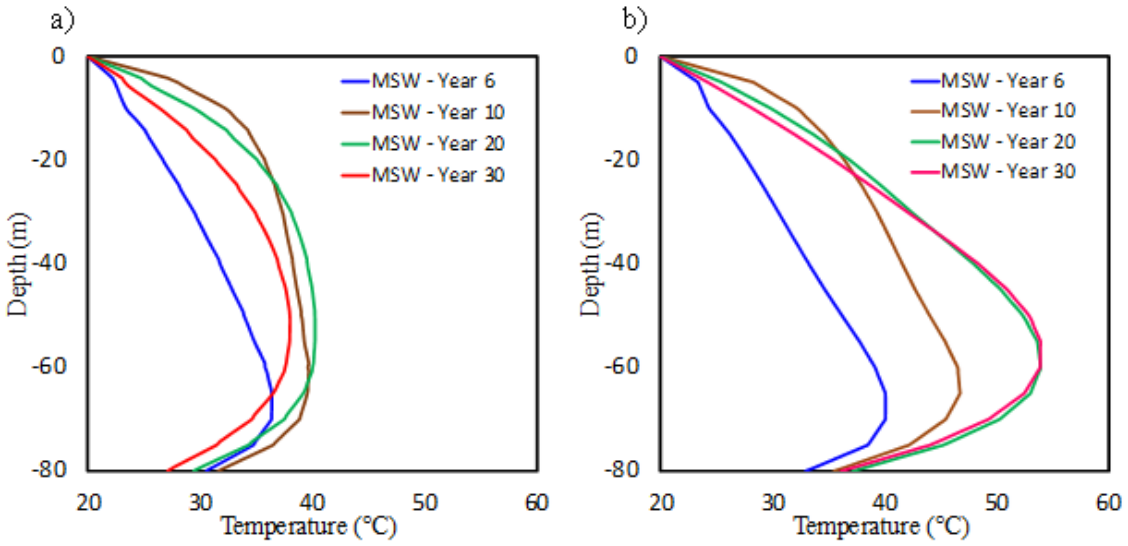

Figure 4-4. Temperature profiles for MSW only in the central cross section. A. vertical profiles 5 m from the landfill edge; B. vertical profiles in the center

a. Sensitivity to boundary conditions

The impact of top boundary conditions is presented in Figure 4-5 in which the boundary temperature was increased from 20 to 30 ℃ as might occur in southern regions of the U.S. in the summer. Figure 4-5a shows that the increase of the top boundary temperature increases landfill temperatures by 2 to 10 ℃ at depths from 0 to 50 m due to reduced conductive heat transfer. We explored the sensitivity of the bottom boundary condition on

heat transport and noted that shorter distances between the bottom of the waste and the boundary result in greater heat release and lower temperatures at the landfill bottom.

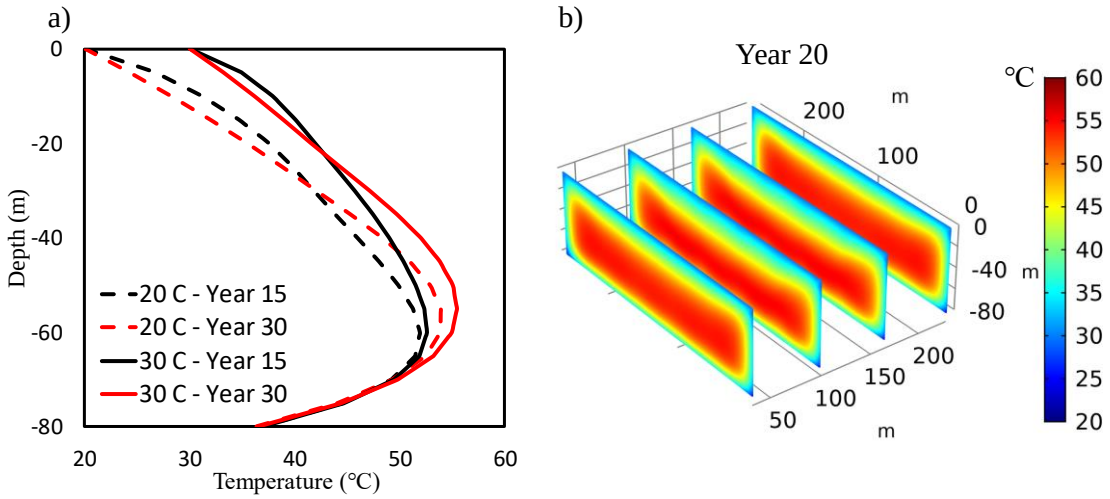

Figure 4-5. Temperature profiles and contours for MSW only with 20 and 30 ℃ at the top boundary. A. vertical profiles in the center at 20 and 30 ℃; B. temperature contours in Year 20 with a 30 ℃ boundary

b. Sensitivity to landfill height

The impact of landfill height is illustrated by comparing the normalized temperature profiles for 40 and 80 m high landfills (Figure 4-6). The 40 and 80 m landfills are full in 3 and 6 years, respectively. For the 40 m landfill, the maximum temperature in Year 15 is ~10 °C higher than in Year 6, but the predicted maximum temperature (~ 47 °C) does not reach the inhibitory range. From Years 15 to 30, the maximum temperature in the 40 m landfill decreases from 47 °C to 41 °C, which indicates that heat loss is exceeding heat generation as described with respect to Figure 4-3. For the 80 m landfill, the maximum temperature increases 13 °C from Years 6 to 15 and an additional 2 °C from Years 15 to 30, demonstrating how the impact of conductive heat transfer is reduced with increasing landfill height. The convex shape of the temperature-depth relationship is predicted for both landfills. As the 80 m landfill is only full at the end of Year 6, the deeper maximum temperature for the 80 m landfill at Year 6 is likely because the landfill was not full until Year 6, hence there was a steeper temperature gradient from the center of the landfill to the surface. In addition, the 80 m landfill has more waste with a wider age range compared to the shallow landfill, resulting in a shift in elevation of the maximum temperature location with time. Of course, the geometry used for these simulations neglects the fact that landfills have side slopes that represent additional surface area for heat loss.

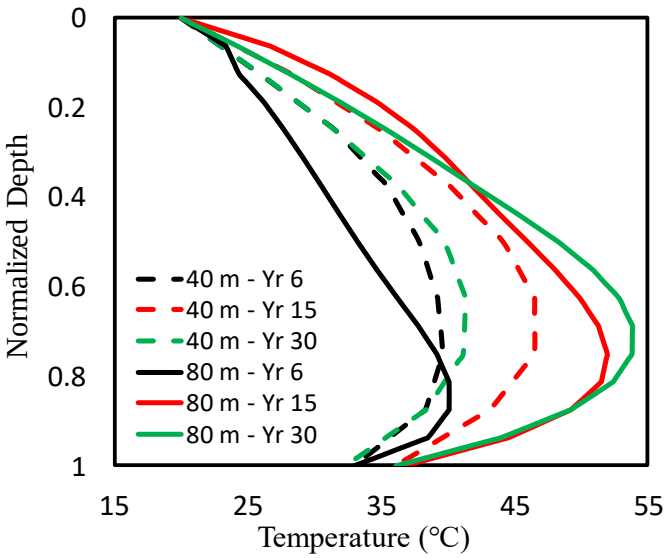

Figure 4-6. Temperature profiles for 40 m and 80 m high landfills

c. Sensitivity to MSW biodegradation rate

To investigate the impact of biodegradation rate on heat accumulation, a simulation was conducted with the methane decay rate constant doubled (Figure A1). Note that waste component specific decay rates were used (Table 6-2). In Years 6, 15 and 30, the maximum temperatures increased 8, 4, and 2 °C, respectively, when the decay rates were doubled. The slight temperature decrease from Years 15 to 30 is attributed to the inhibition of biodegradation. Figure A1b shows that the maximum temperatures are ~5 °C higher and reached faster than the base case as more heat is generated at increased decay rates.

d. Impact of ash and metal corrosion

Figure 4-7 illustrates scenarios in which columns of pure ash are buried in the center and corner of a landfill. In both scenarios, ash was buried in Layers 2 to 15 and the first ash-containing cells are Cell 14 (ash in center) and 10 (ash in corner) in Layer 2 (Please see Section VI.6 and Figure 6-2c for a description of the hypothetical landfill geometry). The mass of ash disposed did not fill a complete column so the ash is surrounded by MSW. The overall volume ratio of ash to MSW in each ash-containing cell is 1:5. All simulations assume the availability of CO_2. To the extent that CO_2 does not penetrate into the ash column, heat generation attributable to carbonation will be reduced.

For the ash-in-center scenario, heat accumulation attributable to ash hydration/carbonation results in more heat accumulation than the MSW only case (Figure 4-7 vs Figure 4-3). The results show that the maximum temperature in the center of the ash column exceeds 100 °C in Year 2 and further increases to 200 °C in Year 6 when ash disposal stops. The similar temperature profiles for Years 6 to 15 indicate that the heat generation rate (ash hydration and carbonation) is approximately equal to the heat loss rate in which heat conduction is dominant due to the extreme temperature gradient to the top and bottom boundaries. In addition, the maximum temperature in the ash column occurs at 10 to 30 m above the bottom boundary, suggesting that the conductive heat transfer rate from the hottest zone to

the bottom boundary is lower than the heat transfer rate to the top boundary. Heat propagation from the ash column to the adjacent MSW is also illustrated in Figures 4-7 and A2 and illustrates the importance of heat transfer through the landfill. In Year 2, the impacted regions due to ash hydration/carbonation are confined to the location of ash column. However, after Year 10, the maximum temperature in the ash column decreases while temperatures in the adjacent MSW increase.

For the ash-in-corner scenario, Figures 4-7g to 4-7l illustrates an expanding elevated temperature region (> 200 °C). The maximum temperature for the ash-in-corner scenario is 10 to 20 °C higher than the ash-in-center scenario, indicating a lower heat loss rate due to the restricted evaporation/condensation as water vapor cannot transfer out of the landfill walls.

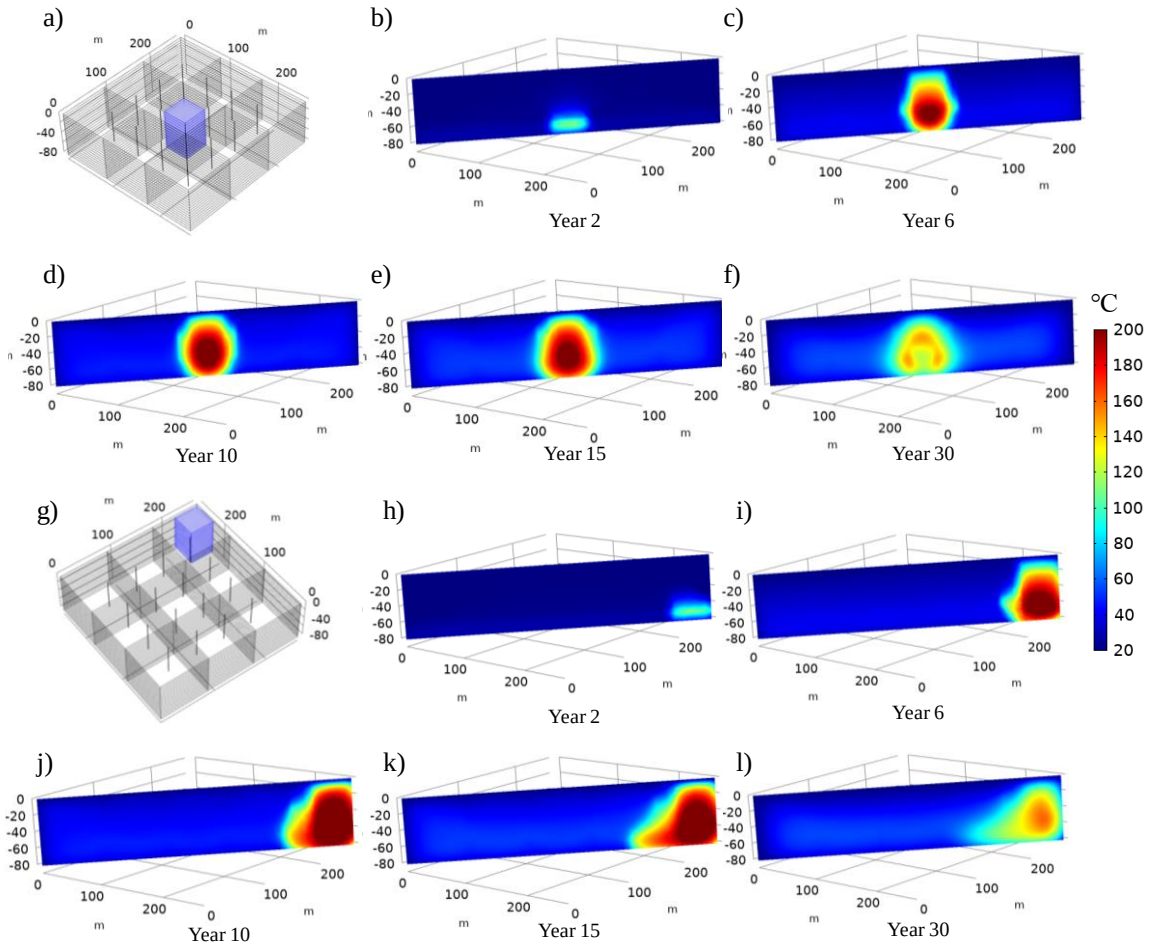

Figure 4-7. Temperature contours for the landfill with ash columns in the center (a to f) and in the corner (g to l) (the disposal scenarios are illustrated in part a and g)

To illustrate the impact of the disposal location of the pure ash column, the volume fraction of regions with elevated temperatures (> 65 °C and > 80 °C) for the ash-in-center and ash-in-corner scenarios are presented in Table 4-1. For the ash containing cases, the higher volume fraction for the ash-in-center scenario indicates larger elevated-temperature affected regions. In contrast, the lower volume fractions for the ash-in-corner scenario

denotes less elevated-temperature affected regions with greater maximum temperatures. While minimizing the temperature impacts of ash is an appropriate objective, ash placement must also consider temperature impacts on a geomembrane such that placement in a true corner adjacent to a liner would not be appropriate. In reality, the difference in affected volume fraction between the center and corner disposal scenarios is small enough that operational considerations may dictate ash placement.

Two additional simulations with ash were conducted. First, a case was analyzed in which the ash was hydrated prior to burial and the FEM-3DM predicted that pre-hydration would reduce the maximum temperature by ~40 ℃ (Figure A2). Second, 10 and 20% ash were mixed with MSW and the results are illustrated in Figure A3. The temperature profiles are much cooler than cases in which the ash is segregated. At 10% and 20% ash, the maximum temperature never exceeds 80 and 120 ℃, respectively. However, at 20% ash, 63% of the total MSW volume exceeds 80 ℃ in Year 20. This affected volume is considerably higher than the segregated ash scenarios and indicates the need to carefully evaluate ash disposal quantities.

Metals are an additional reactive waste that may be mixed with MSW. The temperature contours in MSW landfills with 1.7% and 3.4% Al content are illustrated in Figure A4. The disposal of Al-MSW mixtures leads to maximum temperature of 90 and 135 ℃ for 1.7 and 3.4% Al content, respectively. Given the potential importance of both ash and Al as heat sources, research is needed to evaluate rate constants and the extent of reaction applicable to landfills.

e. Simulation Summary

The impacts of waste composition and disposal strategies were quantified using the cumulative normalized landfill volume (CNLV) with temperatures greater than 65 and 80 ℃ (Table 4-1). In Table 4-1, the CNLV of the ash-in-center scenario is slightly greater than that of the ash-in-corner scenario, indicating that the corner scenario has a smaller elevated temperature region. The decrease in CNLV from the hydration and carbonation to carbonation only scenarios suggests that pre-hydrating ash (prior to disposal) is one approach to reduce the energy in the ash. In fact, ash may be wet before leaving the point of generation in which case some or all hydration will occur prior to burial. For the cases with reactive waste evenly distributed in landfills, the CNLV > 65 ℃ is significantly greater than ash-in-center and ash-in-corner scenarios. When the concentration of reactive waste is relatively low (10% ash and 1.7% Al), the CNLVs > 80 ℃ are close to 0. However, when these waste disposal quantities are doubled, there is a marked increase in CNLV. Finally, in subsequent field work, it was demonstrated that by allowing ash to remain above ground for ~60 days, considerable ash carbonation occurred prior to burial, further reducing the release of heat from ash after burial (Van Brundt et al., 2020).

Table 4-1. Cumulative normalized landfill volume (CNLV) with temperatures greater than 65 and 80 ℃ and maximum temperature at waste bottom zone in Year 20

Case	CNLV > 65 ℃	CNLV > 80 ℃	Max T at waste bottom in Year 20 (℃)
MSW only	0	0	37
ash-in-center[a]	0.07	0.05	139
ash-in-corner[a]	0.06	0.04	173
ash-in-center[a] **(carbonation only)**	0.03	0.02	85
10% ash[a]	0.47	0	49
20% ash[a]	0.81	0.63	65
1.7% Al[a]	0.59	0	54
3.4% Al[a]	0.86	0.71	86

b. For the ash-in-center and ash-in-corner scenarios, the ash comprises 2.3% of the total landfill volume and is segregated. For the 10 and 20% ash and the 1.7 and 3.4% aluminum cases, the waste is uniformly mixed with MSW in the landfill. The CNLVs are thus not comparable but each case represents hypothetical landfill practice

f. Comparison of model simulations to field data

Model simulations were compared to field temperature data published by Hanson et al. (2010) by comparing the temperature profiles for the 40 m depth simulation to published data (Figure 4-8). Hanson et al. (2010) investigated long-term spatial and temporal variations of temperatures at landfills in different climatic regions including Alaska, British Columbia, Michigan, and New Mexico. Hanson et al.'s data are compared to our Year 10 simulation, allowing that the simulated landfill required three years to fill. In Figure 4-8, our simulation temperature profile at the doubled biological decay rate is closer to the profiles of the Michigan landfill than the base case. Michigan is likely most typical of an eastern US landfill in terms of rainfall, leading to a potentially higher biological degradation rate than the default. Of course, a proper comparison between our model and field data would require extensive site-specific information. Nonetheless, model simulations and the field data are comparable and both illustrate maximum temperatures deep in the landfill.

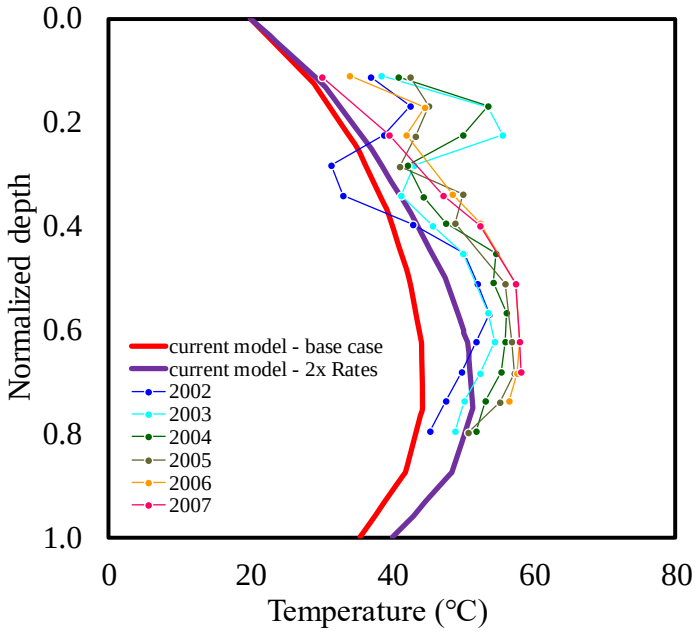

Figure 4-8. Normalized temperature profiles for simulation results and field data (Hanson et al. 2010)

B. Thermal Reactions of MSW under Abiotic Conditions

An experimental program was conducted to evaluate whether exothermic reactions could be measured with synthetic MSW as a substrate under abiotic conditions at elevated temperatures. Four phases of laboratory testing were conducted on synthetic MSW (Table 4-2). Phases 1 and 2 were conducted at a pressure of 382 kPa in a N_2 environment, spanning a temperature range from 70 to 120 °C (158 to 248 °F). Phases 1 and 2 provided initial insights into possible processes that can occur in an inert (N_2) headspace, and resulted in a finding that wood (biomass) charring occurs analogous to field observations made at some ETLFs. In Phase 3, single reactors were operated at 0 and 382 kPa with an initial headspace composition of 50% CH_4 and 50% CO_2. Biological inhibitors were added to the synthetic MSW to ensure abiotic conditions. Temperatures were gradually increased in Phase 3 from 70 to 200 °C (158 to 392 °F). In Phase 4, testing was conducted in the high pressure (382 kPa) reactor under the same conditions as in Phase 3, except with constant heat flux as opposed to constant temperature. The testing in Phase 4 was to quantify the energy input required to maintain a specific temperature.

Table 4-2 Experimental Design for Waste Undergoing Abiotic Thermal Reactions

Phase	Temperature	Pressure (kPa) (atm)	Head-space	Bio-logical Inhibitor	Duration	Objective
1	70 to 120 °C (158 to 248 °F)	382 (3.77)	N_2	No	4 months	Establish initial understanding of MSW reactions in inert atmosphere at temperatures relevant to ETLFs
2	50 to 200 °C (122 to 392 °F)	382 (3.77)	N_2	Yes	3 months	Explore wider temperature range relevant to ETLFs.
3	50 to 200 °C (122 to 392 °F)	0 & 382 (1 & 3.77)	50% CO_2, 50% CH_4	Yes	~1 year	Evaluate potential for pyrolysis to occur under simulated landfill conditions including elevated pressure
4	Variable	382 (3.77)	50% CO_2, 50% CH_4	Yes	~1 year	Constant wattage input to calculate the energy change during reaction

1. Char Formation

Phase 1 confirmed the formation of char in a pyrolytic environment in the absence of oxygen and biological activity. Figure 4-9 shows a sample of the synthetic MSW prior to and after reaction. The original sample contained plastics, textiles, wood, and other non-putrescible waste. Figure 4-9b shows a wood sample recovered from the reactor after being subjected to the anoxic elevated temperature environment for 4 months. The wood is charred throughout (see bottom image of Figure 4-9b showing interior of sample), whereas no charred material was present in the original synthetic MSW. None of the paper in the synthetic MSW charred during this experiment, and none of the other MSW components showed visible signs of degradation after reaction.

Based on this observation, a potential mechanism cannot be postulated. However, the wood began to react at a lower temperature compared to the other MSW components, including the paper. It is possible that the volatile matter in the wood that is not present in paper may be the cause of the charring of the wood and the ability to react at lower temperatures.

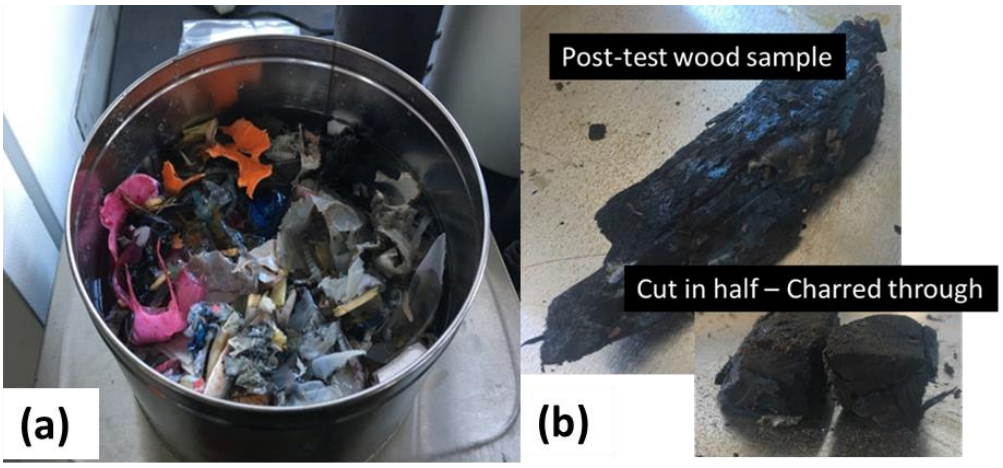

Figure 4-9. (a) Synthetic MSW prior to Phase 1 test and (b) post-test wood sample showing charring

2. Primary Gas Ratio

Testing in Phase 3 demonstrated that elevated temperatures result in a change in the primary gas ratio (CH_4/CO_2) even under abiotic conditions. Changes in the primary ratio gas with temperature for the low- and high-pressure reactor tests in Phase 3 are illustrated in Figure 4-10. During testing, the reactors maintained a constant primary gas ratio of 1.0 for nearly 100 days at temperatures up to 71 °C (160 °F). However, when the temperature was increased to 77 °C (171 °F), the primary gas ratio in both reactors increased from 1.0 to 1.2. Further increasing the temperature to 85 °C (185 °F) had no effect on the primary gas ratio, which remained stable at 1.2 for 11 days (day 113 to 124). On day 125, there was an abrupt decrease in primary gas ratio from 1.2 to 0.9 in both reactors. The processes causing these shifts in the primary gas ratio could not be determined from the experimental data, and whether the ratio shift was due to CH_4 consumption or CO_2 production or both could not be quantified. The changes in primary gas ratio with temperature were not affected by pressure as the ratio was essentially the same for the atmospheric and elevated pressure reactors (Figure 4-10).

The sudden drop in primary gas ratio as the temperature increased above 75 °C is similar to that observed in the field (Figure 4-11). For example, at an ETLF in the midwestern US, the primary gas ratio dropped precipitously from approximately 1.3 to 0.3 as the wellhead temperature spiked from 54 to 68 °C (Benson 2017). The similarity between the laboratory and field findings suggests that abiotic reactions may contribute to a drop in primary gas ratio in ETLFs. An abiotic mechanism for a decrease in the primary gas ratio could occur in parallel with a biological mechanism whereby biological methane generation is inhibited concurrent with both biotic and abiotic CO_2 production.

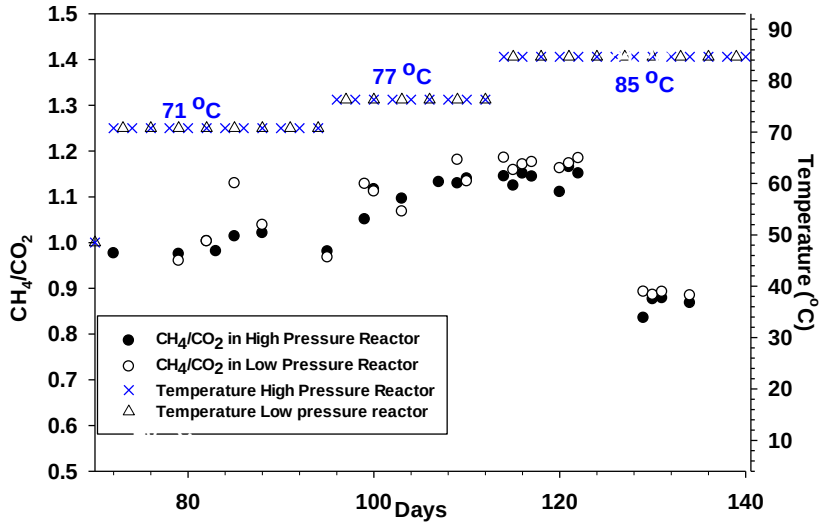

Figure 4-10. Primary gas data for high- and low-pressure laboratory reactors during Phase 3

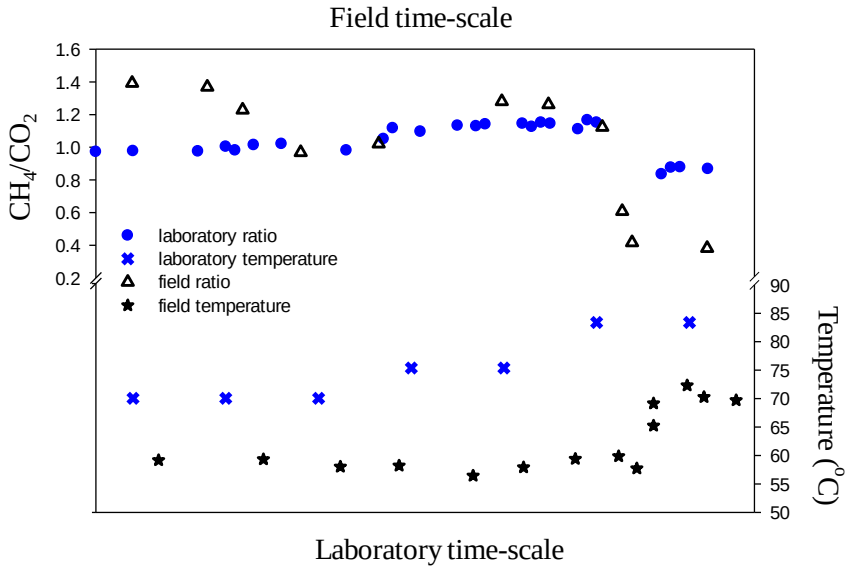

Figure 4-11. Correlation between laboratory and field primary gas ratios and temperature. The time scales for the laboratory and field systems are in days and years, respectively.

3. Hydrogen Production

Hydrogen was produced in both reactors during the Phase 3 tests. H_2 production was nearly four times higher in the high-pressure reactor compared to the low-pressure reactor (Figure 4-12). H_2 generation in the high-pressure reactor began after 10 days at 49 °C (120 °F), whereas the low-pressure reactor did not produce H_2 until 45 days at the same temperature. A subsequent increase in temperature to 71 °C (160 °F) resulted in a pronounced increase in H_2 production at high pressure, whereas the H_2 concentration remained the same (0.13 %) in the low-pressure reactor. A further increase in temperature to 77 °C (170 °F) led to a decrease in H_2 production for both reactors, which was not expected. H_2 decreased from

0.8 to 0.2 % in the high-pressure reactor, and H_2 production ceased in the low-pressure reactor. The mechanism for the shifts in H_2 production and consumption are unclear.

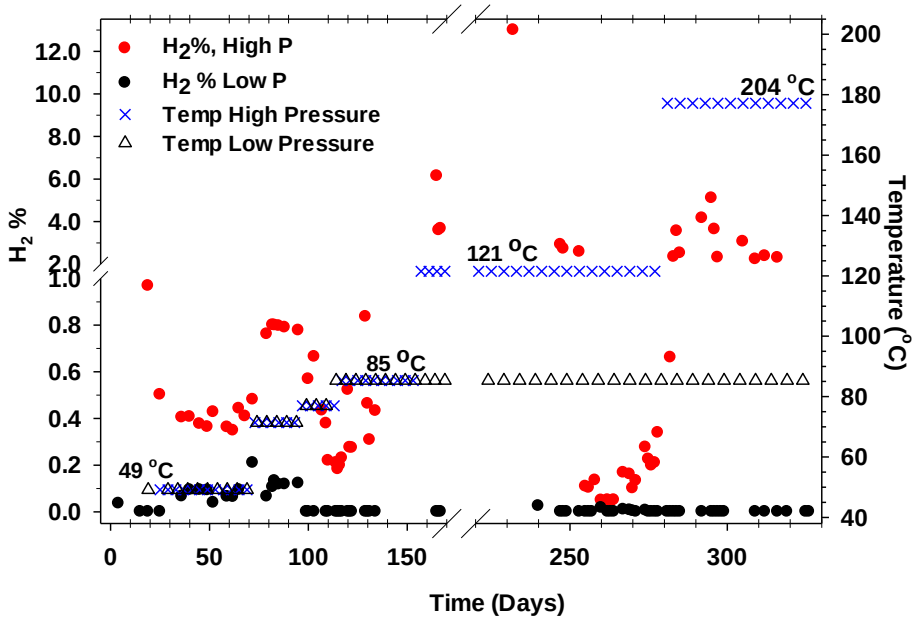

Figure 4-12. Hydrogen generation for the low- and high-pressure reactors as a function of time and temperature

Hydrogen production in both reactors may have been related to the production of volatile hydrocarbons and oxygenated chemical species that were also detected (Figure 4-13). Concentrations of volatile species in the high-pressure reactor were 4.5 times those in the low-pressure reactor. These volatiles in the high-pressure reactor may have reacted with each other, or with the MSW solids, generating H_2 as a byproduct and contributing to the elevated H_2 in the high-pressure reactor. Carbon monoxide (CO) was also detected and is a byproduct of reactions but not attributable to combustion because the atmosphere was anoxic. Volatiles and CO are also commonly encountered in the anoxic conditions within within ETLFs (Benson 2017) and CO may be produced by anaerobic biological activity as well (Bott and Thauer, 1987).

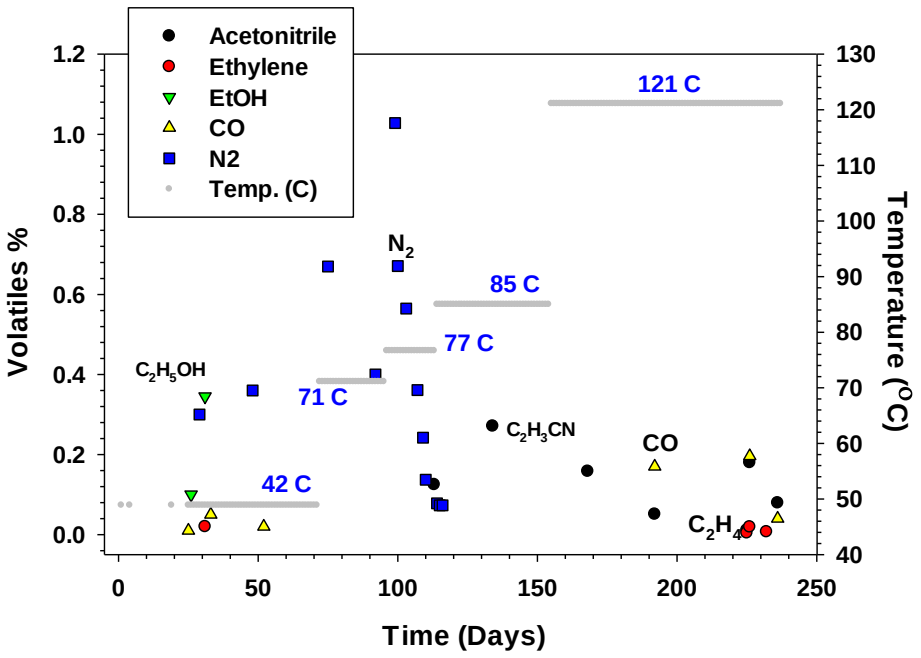

Figure 4-13. Concentrations of volatiles in the high-pressure reactor

4. Moisture Content

The changes in CH_4 and CO_2 concentration also appear related to changes in moisture content (Figure 4-14). Moisture content was calculated by mass balance using the initial moisture content of the MSW and moisture removed during gas sampling. Gases removed during sampling were assumed to be water-saturated, and they were replenished with dry CH_4 and CO_2.

Transitions in the CH_4 and CO_2 concentrations occurred at essentially the same moisture content in both reactors. For example, when the moisture content reached 47 % in both reactors, the CH_4 concentration began increasing and the CO_2 concentration began decreasing (primary gas ratio increased). This transition occurred with an increase in temperature. In contrast, when the moisture content reached 43.5%, there was an abrupt reversal in the CO_2 and CH_4 concentrations (day 125, Figure 4-14), without a change in temperature (constant at 85 °C or 185 °F until day 154). These transitions also occurred at the same time in both reactors, even though the reactors were operated at different pressures. This is consistent with H_2 production being independent of pressure as discussed above. The reversal in the trend also suggests that different mechanisms may be involved in CO_2 production and/or CH_4 consumption as the moisture content changes.

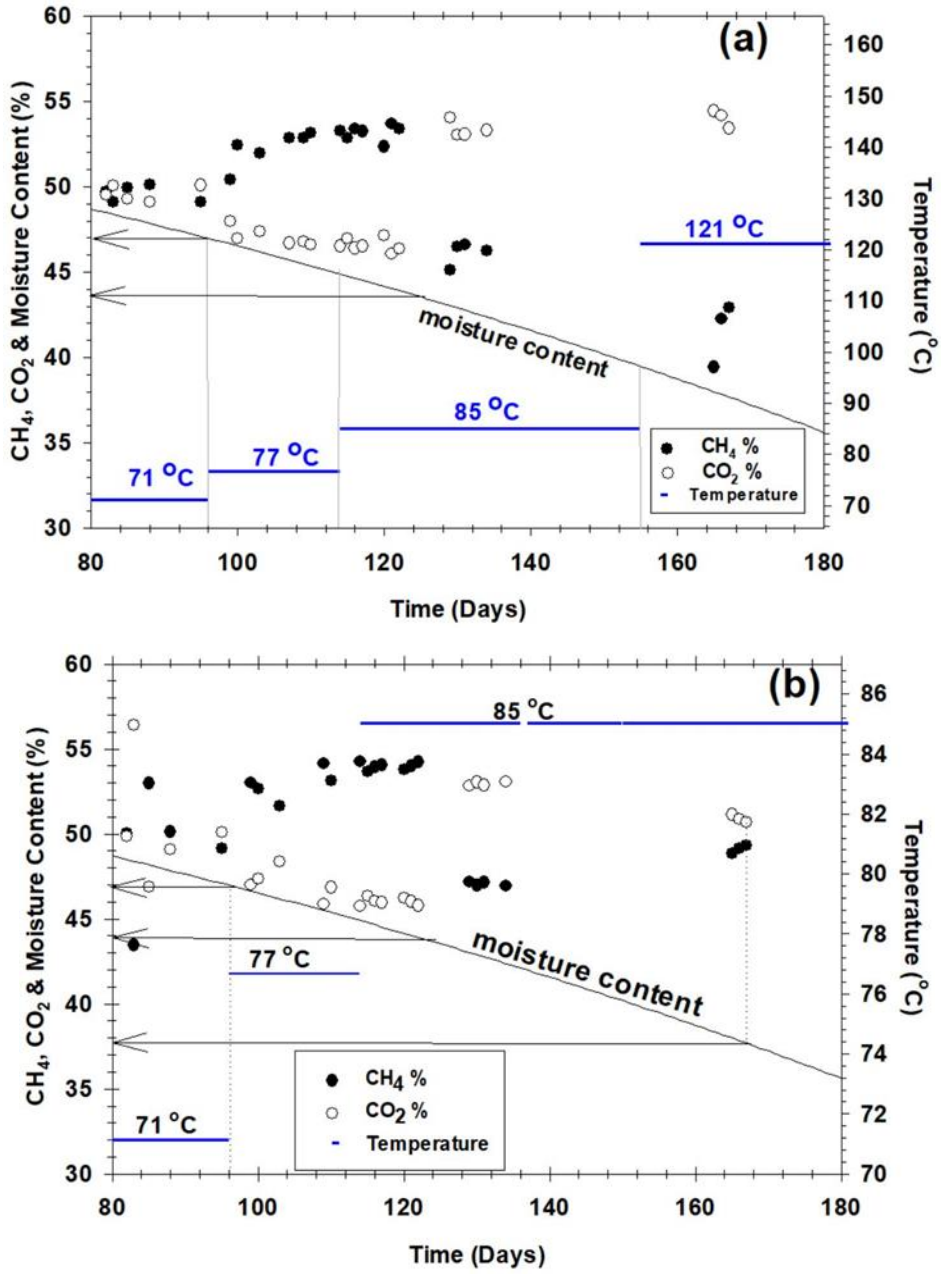

Figure 4-14. (a) High- and (b) low-pressure laboratory reactors demonstrating a temperature and water dependence on CH_4 and CO_2 concentrations. Initial moisture content in reactors was 55%. Low pressure reactor limited to 85 °C (185 °F) to maintain atmospheric pressure (0 kPa).

5. Energetics

Reactor testing in Phase 4 was conducted in the high-pressure reactor only using heat-flux control to evaluate the energetics of the reactions. By varying the heat flux, the reactor temperature varied in response to the processes occurring in the reactor. The intent was to quantify energy that might be associated with exothermic and endothermic reactions in the waste. The energy input was maintained for a period of time while monitoring temperatures

and gas composition. Different energy inputs were also evaluated. The temperature record is shown in Figure 4-15 along with the H_2 concentration and the energy input to the reactor. The record shows the temperature differential (ΔT), which is the difference in temperature between the inside of the reactor and room temperature, where room temperature represents a far field condition (i.e., $\Delta T = T_{reactor} - T_{far\ field}$).

The increase in temperature differential with time at constant energy inputs of 51.1, 56, 60, and 70 W is presented in Figure 4-15. The temperature data show that an exothermic reaction is occurring within the reactor (ΔT would remain constant for a given energy input in the absence of a reaction). There are other instances where a constant energy input resulted in near constant ΔT after equilibrium was established (e.g., 46.6, 58, final increment at 60 W). Importantly, H_2 production shows a steady increase for those energy input intervals, confirming an increase in the extent of MSW reactions as the input energy was increased.

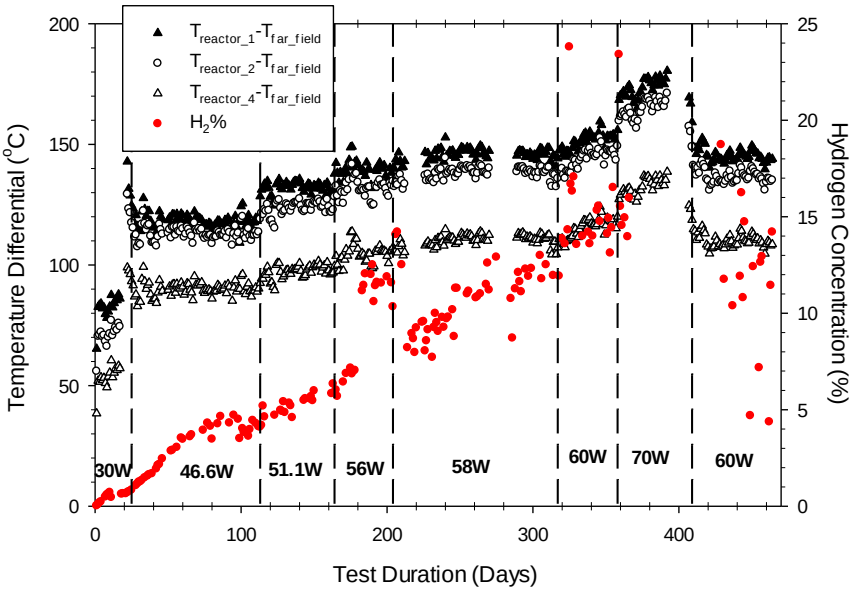

Figure 4-15. Temperature profiles for the constant heat flux test

CH_4, CO_2, and H_2 concentrations measured in the constant flux reactor are presented in Figure 4-16. The initial input energy of 30 watts was selected to bring the anticipated temperature of the reactor to near 85 °C (185 °F), where increasing CO_2 concentrations and decreasing CH_4 concentrations were recorded in the Phase 3 experiments. Initially, the CO_2 and CH_4 concentrations matched the 50-50 volumetric mixture that was used to pressurize the reactor to 382 kPa. As the experiment progressed, the CO_2 and CH_4 concentrations diverge, and the rate of divergence increased as the energy input increased. H_2 production occurred at a nearly constant rate except for intermittent points with much higher rates (e.g. with 56 W). Towards the end of the experiment, around 400 d, the CO_2 and CH_4 concentrations stabilized and H_2 production became erratic, suggesting that the reactions had completed. This suggests that CH_4 consumption and H_2 production are linked, but the mechanism is unclear.

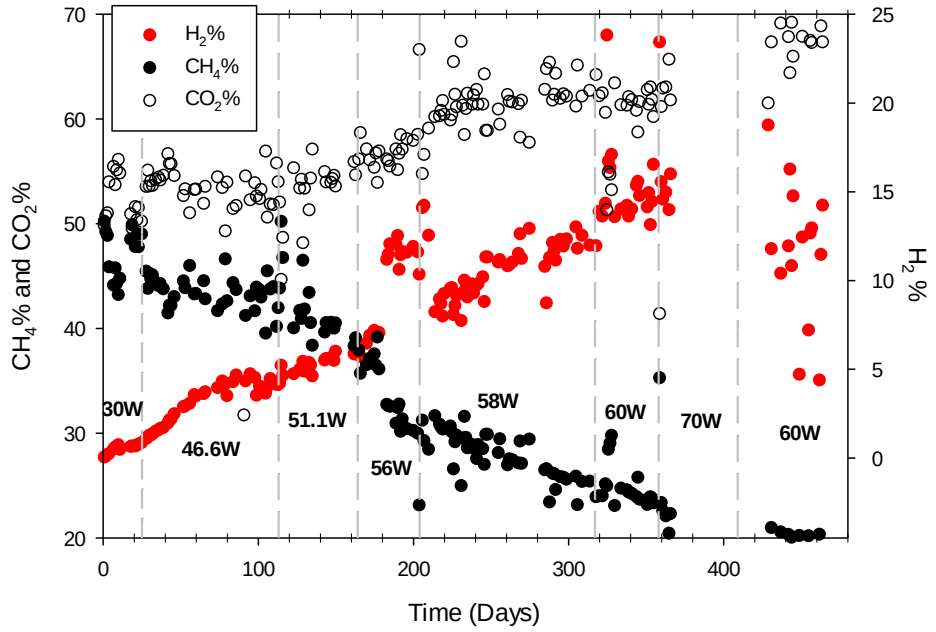

Figure 4-16. CH_4, CO_2, and H_2 concentration profiles for varying energy input. There is a data gap at 70 W due to an instrument malfunction

6. Implications

The reactor experiments conducted in this study under abiotic and anoxic conditions have shown the following phenomena:

- Charring of some materials occurs at elevated temperature under anoxic conditions without combustion.
- The primary gas ratio in MSW varies as temperature increases, ultimately decreasing at high temperatures.
- Hydrogen is produced under abiotic conditions as temperatures are elevated in MSW
- Volatile organics (C_2H_2 (ethylene), carboxylic acids and acetaldehyde) and carbon monoxide are produced when temperatures are elevated, suggesting that pyrolytic reactions are occurring.
- Mildly exothermic conditions occur in MSW under conditions of elevated temperature and constant energy input.

These observations are similar to the conditions observed in ETLFs, where anoxic conditions and elevated temperatures exist. The energetics that were observed in the reactor experiments suggest that exothermic reactions may occur in ETLFs, but they are modest. Thus, other sources of energy likely are responsible for heat accumulation leading to elevated temperatures in ETLFs.

C. Thermal Properties of Municipal Solid Waste

Thermal properties of MSW and their variation within a landfill, are needed to make heat transfer predictions such as those illustrated in Section A (Hanson et al. 2010, Yeşiller et al. 2016, Hao et al. 2017). Thermal properties of particulate materials, such as soil and MSW, are influenced by the relative proportions, composition, and connectivity of the solid, liquid, and gas phases (de Vries et al. 1963, Abu-Hamdeh and Reeder 2000, Abu-Hamdeh 2003, Fuchs et al. 2013, Nasirian et al. 2015). Thus, the thermal properties of MSW should vary with the composition, water content, and dry density. These attributes of MSW vary spatially within a landfill, particularly with depth.

This section describes the thermal properties of the synthetic waste described in Section B as measured in the laboratory using a guarded heat plate apparatus (thermal conductivity) and a needle probe (specific heat capacity). Fresh and fully degraded wastes were evaluated to ascertain how thermal properties may during the landfill's lifecycle. Tests were conducted on waste prepared at different water contents (6% - air dry, 25, 45, 60%) and under different vertical overburden stresses (2 - 400 kPa) to understand how the thermal properties of MSW vary systematically with operating conditions. Methods to estimate thermal properties of MSW were also explored, and recommendations for estimating thermal properties are provided.

Thermal conductivity (kT) describes the conduction of heat by a material in response to a spatial gradient in temperature. Specific heat capacity (Cs) refers to the amount of energy that must be added per unit mass to raise the temperature of the material by 1 ^{o}C. For porous materials with solid, liquid, and gas phases, the thermal conductivity and specific heat capacity reflect the composite property of a unit volume of material

1. Thermal Conductivity

Thermal conductivity of the waste is shown as a function of gravimetric water content at various overburden stresses in Fig. 4-17a (fresh waste) and Fig. 4-17b (degraded waste). Thermal conductivity increases monotonically with increasing water content for fixed overburden stress, and increases monotonically with overburden pressure at fixed water content for both fresh and degraded waste. For fresh waste, the rate of increase in thermal conductivity with increasing water content diminishes at higher water content, whereas for degraded waste the rate of increase in thermal conductivity appears to increase with increasing water content, at least for the range of stresses that were applied.

Thermal conductivity is shown as a function of water content in Fig. 4-18. Wetter wastes have higher thermal conductivity, and the degraded waste has comparable or modestly higher thermal conductivity than the fresh waste for the same water content. For a given water content and waste condition, higher thermal conductivities correspond to waste consolidated to a higher stress and with higher dry density.

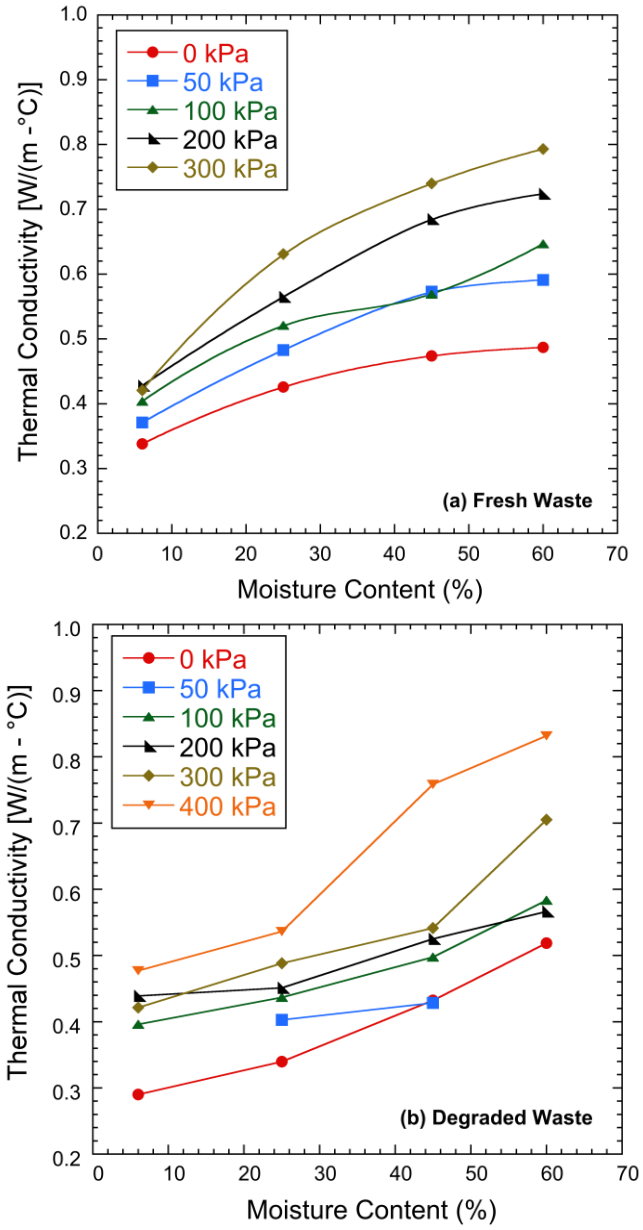

Figure 4-17. Thermal conductivity of synthetic MSW at gravimetric water contents of 6, 25, 45, and 60%: (a) fresh and (b) degraded.

The primary difference between the fresh and decomposed MSW is the food waste component, which was fully decomposed during anaerobic degradation. The food waste (and similar components) has low thermal conductivity relative to other components in the waste and comprises 23% of the total mass of fresh waste (see subsequently in Tables 6-2 and 6-6). Other primary components that are resistant to degradation (e.g., metal, plastic, and glass) remain after degradation and typically have significantly higher thermal conductivity (Tables 6-2 and 6-6). Consequently, degraded waste is comprised of more thermally conductive components, and therefore the overall thermal conductivity of the waste is higher, other factors being equal.

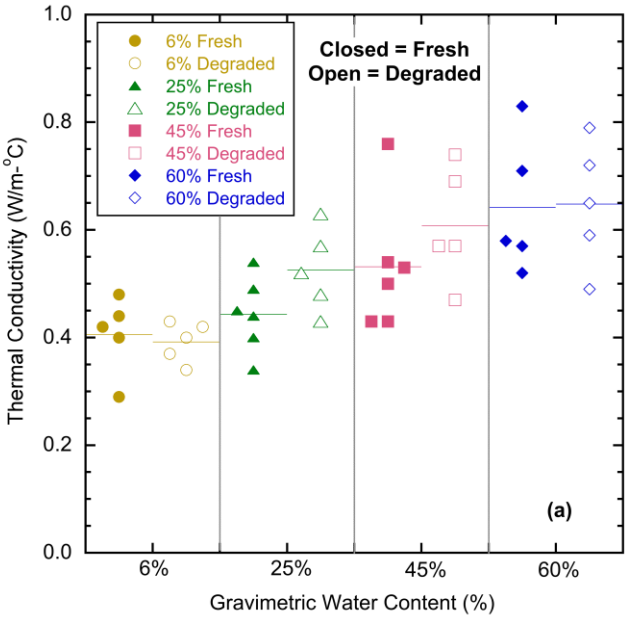

Figure 4-18. Dot plot for thermal conductivity of fresh and degraded MSW over a range of water contents. The center line in each group of dots represents the median.

The effect of dry density of the waste (due to increasing overburden stress) is shown in Fig. 4-19. As the dry density increases, the thermal conductivity generally increases for a given water content and waste condition. The effect of dry density on thermal conductivity is comparable for the fresh and degraded wastes, but is more significant for wetter wastes than for drier wastes. At the highest water contents, increasing dry unit weight resulted in an increase in thermal conductivity of 0.81 W/m-^{o}C per unit change increase in dry density, whereas thermal conductivity of the driest wastes increased by 0.45 W/m-^{o}C per unit change increase in dry density.

The trends with water content in Fig. 4-17 and 4-18 reflect the higher thermal conductivity of water (0.60 W/m-°C) relative to air (0.025 W/m-°C) in the void space as water content displaces air as the water content increases. For example, the thermal conductivity of the fresh MSW is 0.44 W/m-°C at a water content of 6% and overburden stress of 100 kPa, and increases to 0.65 W/(m-°C) when the water content is 60% at the same overburden stress. The trend with overburden pressure reflects a reduction in air-filled voids and greater solid-solid and solid-water contact with increasing overburden pressure.

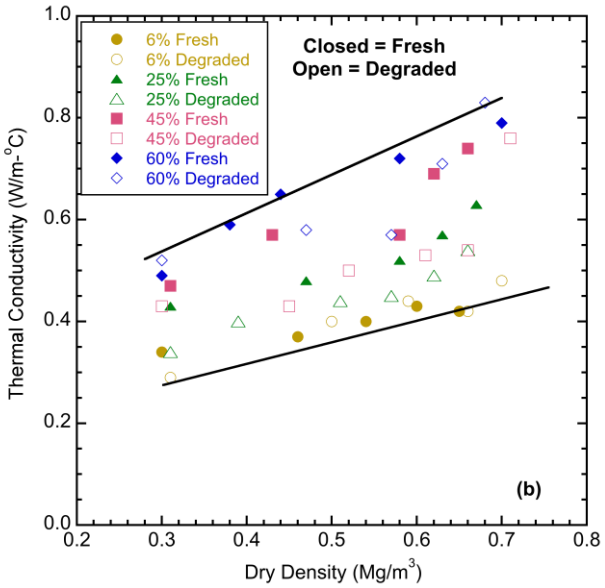

Figure 4-19. Thermal conductivity of fresh and degraded MSW as a function of dry density for different water contents.

Thermal conductivity of the fresh and degraded waste are shown as a function of confining stress in Fig. 4-20a (fresh) and Fig. 4-20b (degraded) in a format similar to that of increasing depth within a landfill (10 kPa ~ 1 m depth). The data indicate that thermal conductivity of waste increases with depth in a landfill due to greater dry density of the waste at higher confining stress for all water contents (Fig. 4-20). For example, the thermal conductivity of fresh MSW with 6% water content increases from 0.34 W/(m-°C) at 2 kPa confining stress (surface) to 0.65 W/(m-°C) at 300 kPa (~30 m deep). Similarly, the thermal conductivity of fresh MSW with 60% water content increases from 0.49 W/(m-°C) at 2 kPa to 0.79 W/(m-°C) at 300 kPa (~30 m deep) confining stress. Stress (or depth) has a similar effect on degraded waste. Thus, waste at depth will conduct heat more efficiently than waste near the surface under the same temperature gradient, all other factors equal. Waste at depth often is wetter and more degraded than waste closer to the surface, further increasing its thermal conductivity and the propensity to conduct heat (Bareither et al. 2012, Breitmeyer et al. 2020).

2. Specific Heat Capacity

Specific heat capacity was measured on fresh MSW at water contents of 25% and 60% after the final thermal conductivity test. Measurements were conducted at five different locations on the surface of the specimen. The measured specific heat capacities are shown in a dot plot in Fig. 4-21 for both water contents. Specific heat capacity of the fresh waste ranged from 1.68 to 2.64 kJ/(kg-°C) at 25% water content, and from 1.91 to 2.79 kJ/(kg-°C) at 60% water content. Higher specific heat capacity was obtained at higher water content because water has the highest specific heat capacity of all MSW components [4.18 kJ/(kg-°C)]. The variation in specific heat capacity within the specimen measured with the needle probe reflects the variety of components within the MSW, each of which has a unique specific heat capacity.

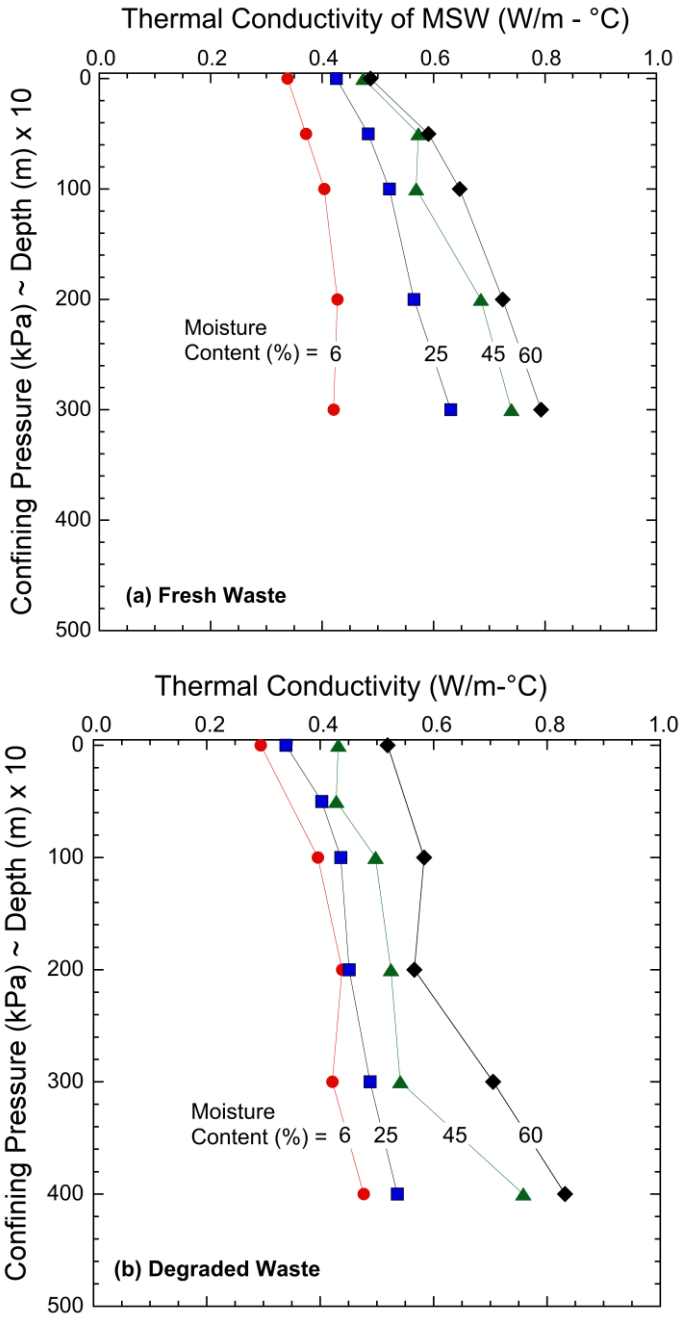

Figure 4-20. Thermal conductivity of synthetic MSW as a function of confining pressure and effective depth: (a) fresh and (b) degraded.

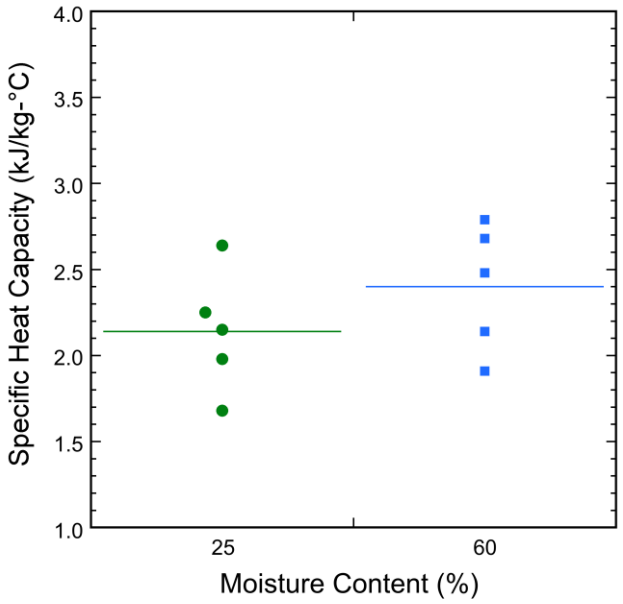

Figure 4-21. Specific heat capacity of fresh waste at water contents of 25% and 60%. The solid horizontal line in each group of dots is the median.

3. Predicting Thermal Properties

For a porous medium comprised of solid, liquid, and gas, the thermal conductivity has an upper and a lower limit as described in the review by Fuchs et al. (2013). The lower limit for thermal conductivity corresponds to heat flow through the various components in series (i.e., k_{TS}); the upper limit corresponds to parallel heat flow (k_{TP}) in the components (k_{TP}). Actual porous materials comprised of a heterogenous mixture of solid, liquid, and gas phases have thermal conductivities that fall between the upper and lower bounds defined by the series and parallel configurations. Thermal conductivities of heterogenous mixtures (k_{Tm}) can be represented by a mixing model that has the form:

$$k_{Tm} = \tilde{O} k_{Ti}^{f_i^{a_i}} \quad (4\text{-}1)$$

where ϕ_i and k_{Ti} are the volume fraction and thermal conductivity of the i^{th} phase and α_i is the mixing weight for the i^{th} phase (ϕ_s and α_s for solid phase, ϕ_l and α_l for liquid phase, ϕ_g and α_g for gas phase). For the case where $\alpha_s = \alpha_l = \alpha_g = 1$, Eq. 6 is the volume-fraction-weighted geometric mean thermal conductivity (Fuchs et al. 2013).

The specific heat capacity of a porous material generally is assumed to equal the mass-weighted sum of the specific heat capacity of each component (Hanson et al. 2008; Faitli et al. 2015):

$$C_s = \mathring{a} C_i m_i \quad (4\text{-}2)$$

where C_s is the specific heat capacity, C_i is the specific heat of the i^{th} component, and m_i is the mass fraction of each component in the MSW

Thermal conductivity of the fresh and degraded was predicted at each water content and overburden stress with Eq. 4-1 with a unique mixing weight for each phase and with the mixing weights $\alpha_i = 1$ (volume-weighted geometric mean). Volume fractions for the solid, liquid, and gas phases were computed for each water content and confining stress using the initial conditions and the compression data from each test. Thermal conductivity of the solid phase for each of the predicted models was computed using volume-weighted solid fractions in the waste (see Tables 6-7 and 6-8), with the thermal properties of the solid components obtained from the database in Trouve and Minnich (2012). Water was assigned a thermal conductivity of 0.6 W/(m-°C) and specific heat capacity of 4.18 kJ/(kg-°C). The gas phase was assumed to be air and assigned a thermal conductivity of 0.025 W/(m-°C) and specific heat capacity of 1.01 kJ/(kg-°C). Volume fractions of each phase in the fresh and degraded wastes are summarized in Tables 6-7 and 6-8 for different conditions. Mixing weights for Eq. 4-1 were obtained by fitting to the thermal conductivity data for fresh and degraded waste. Fitting was done using a least-squares minimization algorithm with the objective function defined as the mean square error between the predicted and measured thermal conductivities. The algorithm yielded $\alpha_s = 0.186$, $\alpha_l = 0.101$, and $\alpha_g = 0.354$ for thermal conductivities in units of W/(m-^{o}C).

Predicted and measured thermal conductivities are compared in Fig. 4-22. For both fresh and degraded waste, the geometric mean underpredicts the thermal conductivity appreciably. Predictions made with the mixing model are in good agreement with the measured thermal conductivities, which is anticipated given that the coefficients in the mixing model were obtained by fitting Eq. 4-1 to the thermal conductivity data.

An independent assessment of the mixing model was conducted by predicting thermal conductivities for MSW reported in Yoshida and Rowe (2003), Hanson et al. (2008), and Khire and Johnson (2018). The predicted and measured thermal conductivities are shown in Fig. 4-23. The mixing model appears to overpredict thermal conductivities at the lower end of the range (< 0.4 W/m-^{o}C), particularly for the data reported by Khire and Johnson (2018). In the upper range (> 0.4 W/m-^{o}C), the predictions are in agreement with the data. The over-prediction of lower thermal conductivities may reflect underweighting of waste with lower dry density in the data set used to fit the model relative to the data in Khire and Johnson (2018), as shown in Fig. 4-24. Khire and Johnson (2018) report more data with lower dry density and lower water content than in the data set used to fit the mixing model.

Specific heat capacity of the fresh synthetic MSW was estimated based on the mass fractions approach in Eq. 4-2 using the data in Tables 6-2 and 6-6. Similar calculations were made for the specific heat capacities reported for MSW in Yoshida and Rowe (2003). The predicted and measured specific heat capacities are compared in Fig. 4-25. Although the data set is sparse, there is good agreement between the specific heat capacities predicted with Eq. 4-2 and the measured specific heat capacities, suggesting that Eq. 4-2 has promise for predicting the specific heat capacity of MSW using mass fractions.

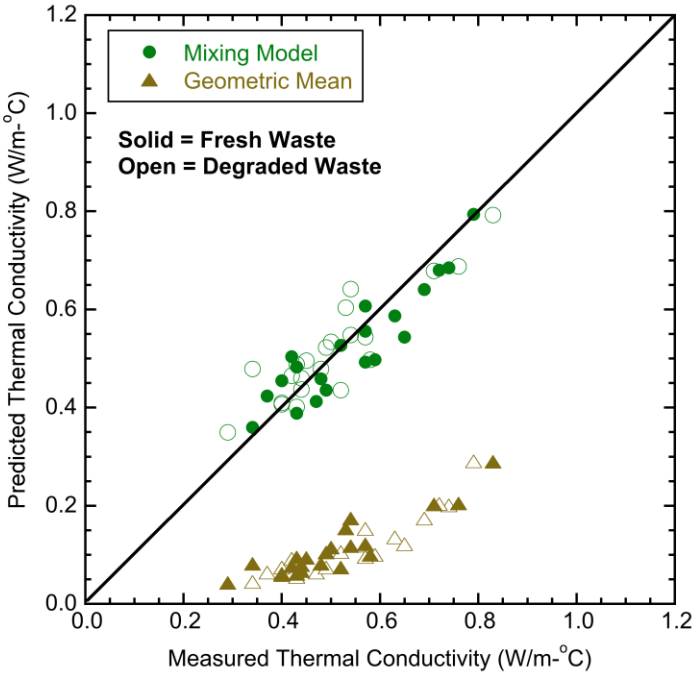

Figure 4-22. Predicted vs. measured thermal conductivity of fresh and degraded synthetic waste using geometric mean and mixing model with $\alpha_s = 0.186$, $\alpha_l = 0.101$, and $\alpha_g = 0.354$.

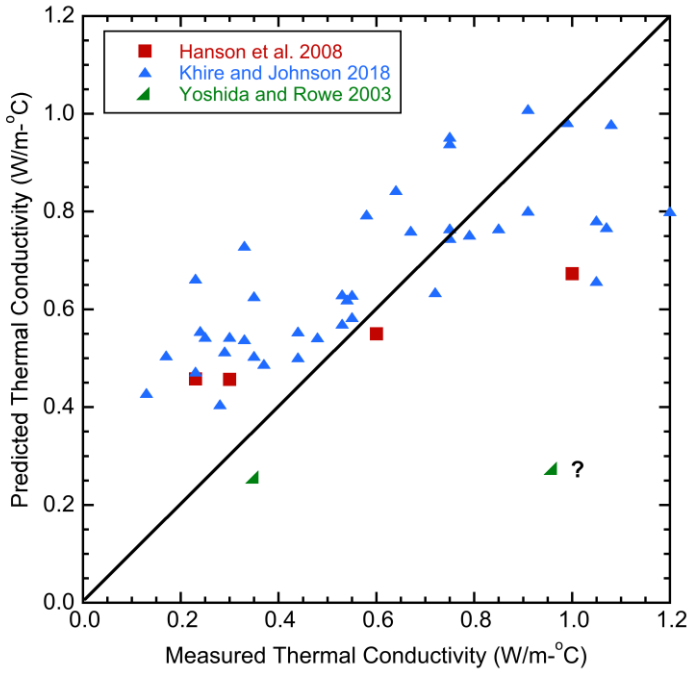

Figure 4-23. Thermal conductivity of MSW predicted with mixing model ($\alpha_s = 0.186$, $\alpha_l = 0.101$, and $\alpha_g = 0.354$) vs. measured thermal conductivity from other studies.

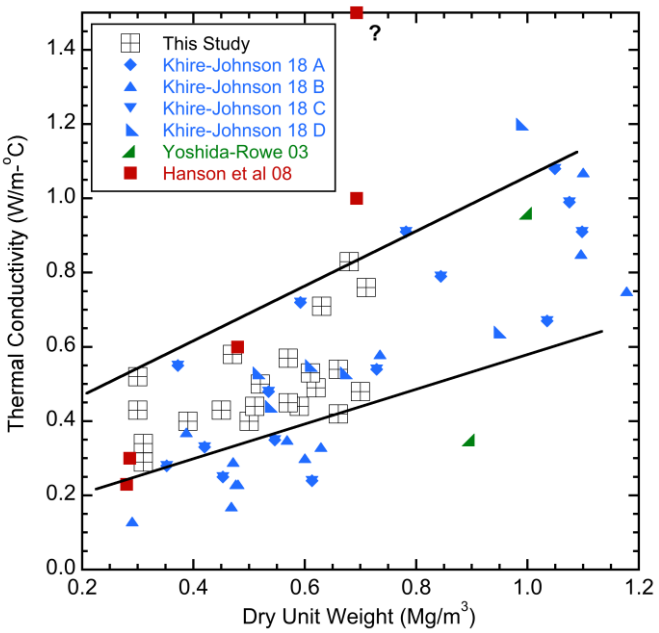

Figure 4-24. Thermal conductivity of waste as a function of dry unit weight from this study and other studies.

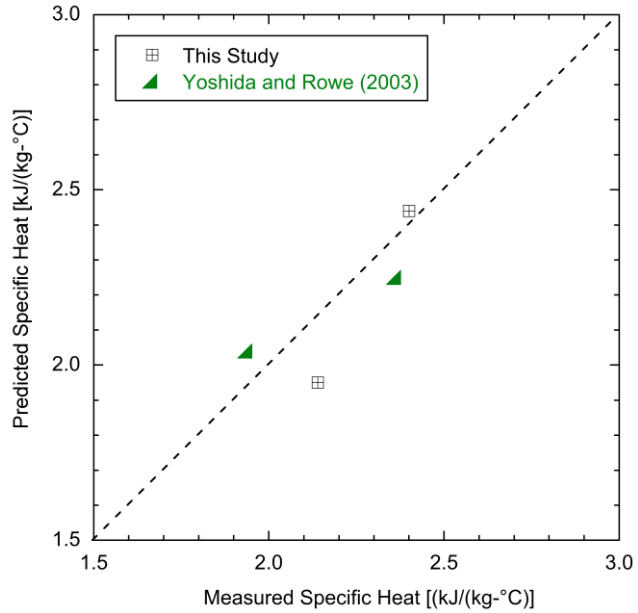

Figure 4-25. Predicted vs. measured heat capacities of fresh waste from current study and MSW from literature using mass-weighted model.

4. Implications

The findings from the thermal properties experiments conducted in this study have the following implications:

- Thermal conductivity of the fresh and degraded waste increases as the confining stress and water content of the waste increases, reflecting a decreasing fraction of less thermally conductive gas phase and greater fraction of more thermally conductive solid and liquid phases. Increasing the confining stress increases the dry density of the waste, resulting in greater particle contact and higher water saturation, both of which contribute to greater thermal conduction and higher thermal conductivity. This indicates that waste deeper in a landfill typically will be more thermally conductive than shallower waste.

- Thermal conductivity of decomposed waste is comparable to, or modestly higher than the thermal conductivity of fresh waste under similar conditions. The higher thermal conductivity is due to loss of less thermally conductive degradable waste during decomposition. A landfill should become modestly more conductive over time as degradation occurs.

- A volume-based mixing model for thermal conductivity was fit to the thermal conductivity data for fresh and degraded waste provides. This model can be used to make reasonable predictions of thermally conductivity, but may over-predict thermal conductivities for less thermally conductive conditions.

- Specific heat capacity of solid waste can be predicted reliably with a mass-weighted model.

D. Instrumentation for Elevated Temperature Landfills

Temperature and pressure are important parameters to be measured in ETLFs. Measuring these parameters over long periods of time to monitor trends is more valuable than one-time measurements. In addition, obtaining a wide spatial range of in-situ temperature and pressure data can be valuable for identifying heat sources, visualizing how the heat is distributed throughout the landfill, assessing how the distribution of temperatures within the landfill changes with time, evaluating stability, and understanding inhibition of gas collection.

Measuring gas and leachate temperatures is often effective as a way to first detect elevated temperatures in landfills. However, measuring in-situ waste temperatures is more valuable than measuring gas or leachate temperatures alone because movement of these fluids within the waste precludes definition of the temperature and pressure distribution as well as identification of hotter or cooler zones. Commercially available instruments to measure in-situ waste temperatures include thermistors, thermocouples, vibrating-wire (VW) temperature sensors, and fiber optic distributed temperature sensing (FODTS) systems. All of these instruments are typically installed in boreholes drilled into the waste. The initial cost of these instruments varies considerably. However, the installed cost is similar, because much of the total cost is associated with the initial drilling and installation, which is similar regardless of the type of instrument. Therefore, the instrumentation selected for any given landfill should be based on the advantages and disadvantages of each type of sensor, as discussed below.

Thermistors and thermocouples measure temperature at a point and can be read with simple and economical devices, but these devices may have calibration and durability challenges associated with the length and temperature of the cables. VW sensors offer good measurement stability and the data are not affected by cable length or cable temperature. Photographs of these temperature sensors are shown in Figure 4-26.

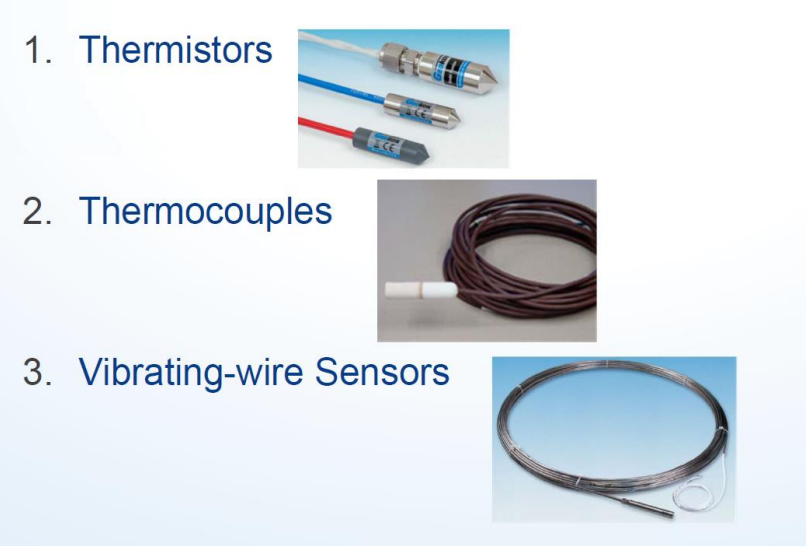

Figure 4-26. Point-Source Temperature Sensors

FODTS systems consist of cables that provide distributed sensing with high spatial resolution data every 0.25-m vertically along the cable, and the data are not affected by cable length or temperature. Analysis of wave length data from FODTS systems can be used to detect problems with the physical condition of the optical fibers and to assess data accuracy remotely, without removing any of the instrumentation. Santoprene® and Teflon® cable coatings provide extended durability for FODTS systems at temperatures as high as 200 °C. FODTS have proven to be more durable than many point source sensors, but still may have a service life of only a few years in harsh ETLF environments. Photographs of FODTS cables and a readout box are shown in Figure 4-27.

Figure 4-27. Fiber Optic Distributed Temperature Sensors (FODTS)

Installation of instrumentation in boreholes in ETLFs is challenging and requires attention to safety. Provisions are often needed to protect drillers and field personnel from pressurized hot gas and liquid expelled from boreholes during installation. Back-flow arresters are now available on some sonic drill rigs to reduce these hazards. Gas monitoring and situational awareness are paramount during all invasive procedures.

Point-source and FODTS instrumentation can be operated remotely using dataloggers equipped for data transmission. The use of dataloggers permits efficient data collection and analysis, and minimizes the need for personnel to visit the instrumentation. A FODTS remote sensing station is shown in Figure 4-28. Flexible mount fixtures at the waste surface, as shown in Figure 4-29, are often recommended to prevent cables from pinching or kinking after installation due to waste settlement.

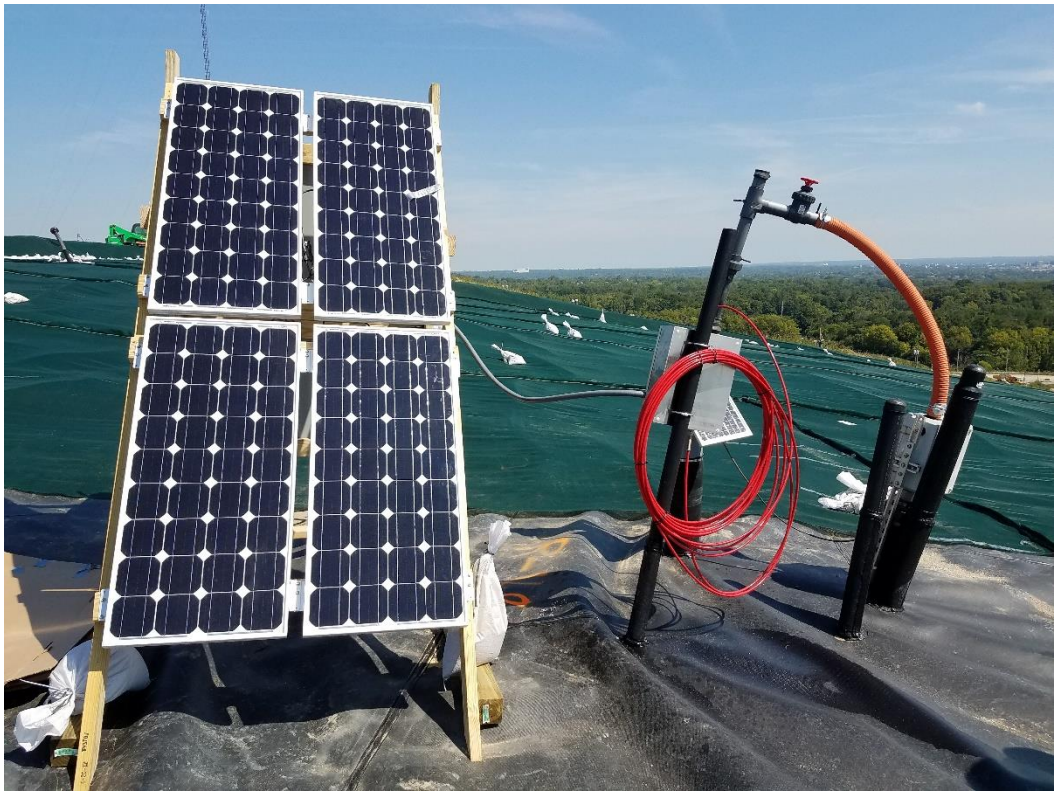

Figure 4-28. Remote Monitoring Station at a FODTS location.

Figure 4-29. Flexible Mounting and Extra Cable for FODTS Readout Box to prevent damage from settlement of waste.

Combined FODTS and VW systems often produce better resolution of spatially and temporally distributed data over longer time periods than other types of point sensors. The FODTS provides high resolution temperature data and the VW provides pressure data.

Figure 4-30 shows an example of a vertical profile showing temperatures measured at several different times as a function of depth in a landfill using FODTS. Figure 4-31 shows an example of pressures measured with VW sensors at several depths in a landfill as a function of time. Figure 4-32 illustrate how FODTS data are used to depict 3-dimensional (3D) isoshell distributions of temperatures in an exothermic zone in a landfill. These figures also show CH_4:CO_2 data for the gas being extracted within or near the exothermic isoshell zones.

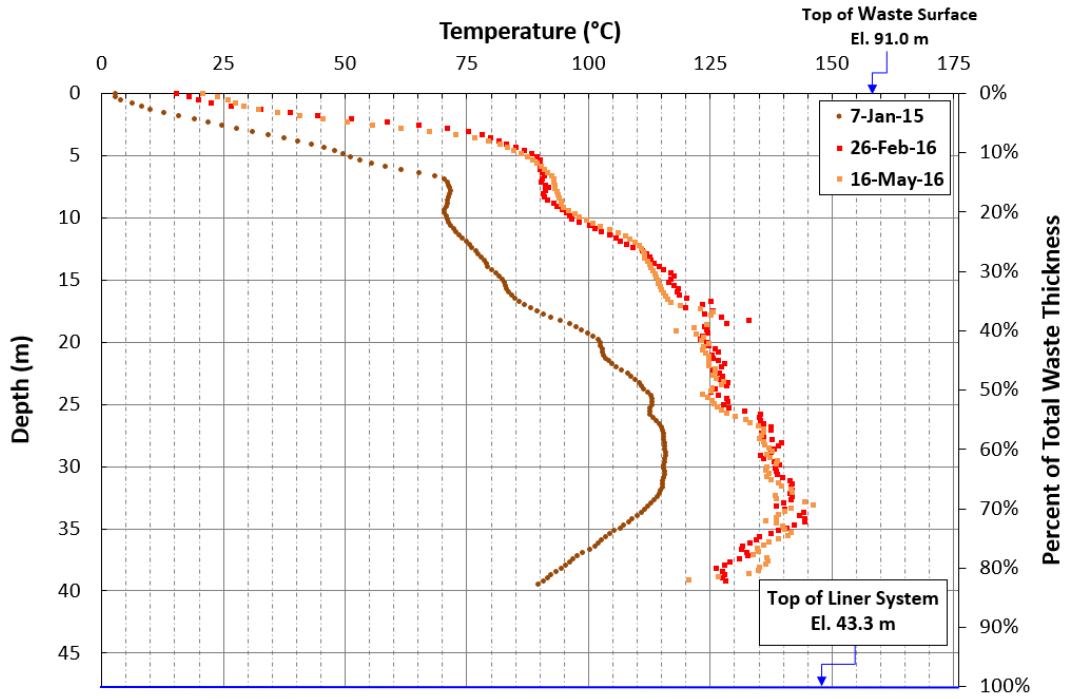

Figure 4-30. Vertical Profile of Temperatures Measured at Different Times as a Function of Landfill Depth.

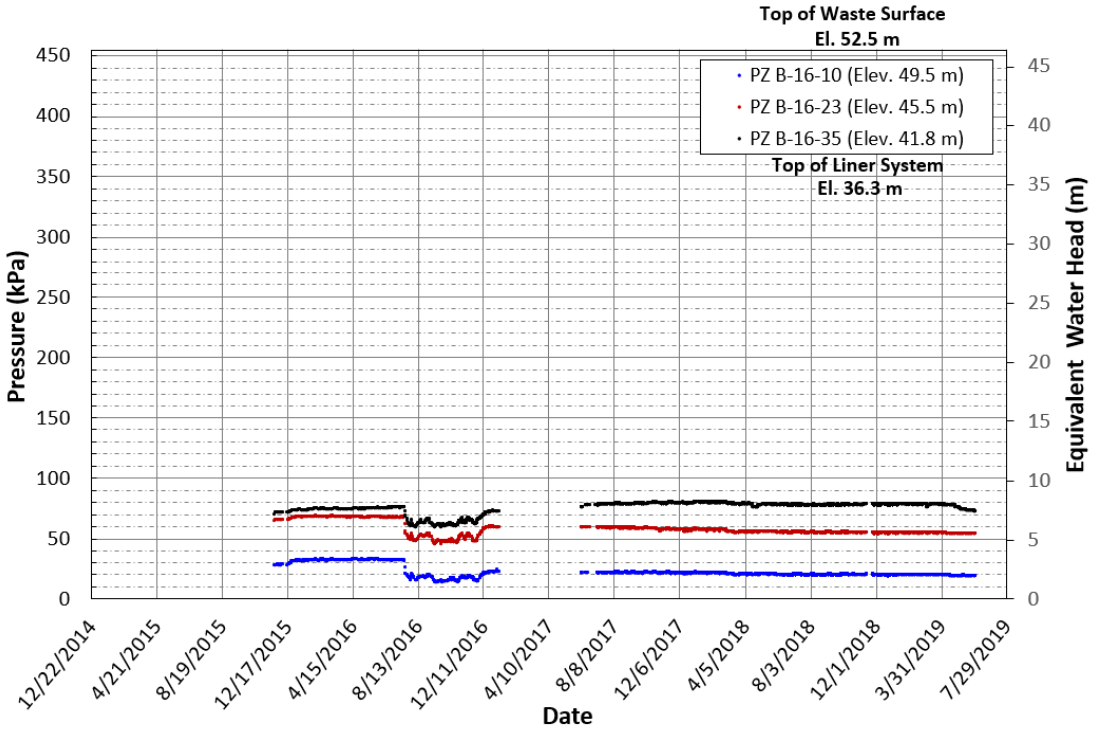

Figure 4-31. Pressure Measured in a Landfill Using VW Piezometers.

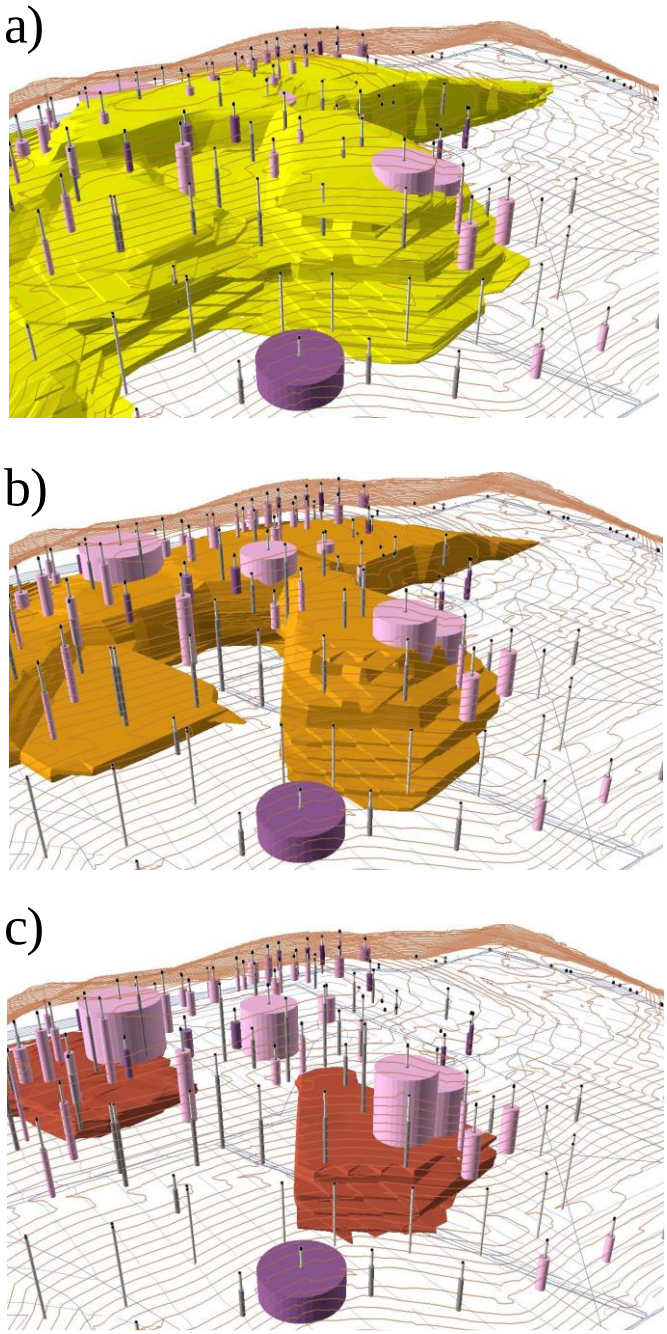

Figure 4-32. 3-Dimensional Distribution (Isoshell) of Temperatures (a) ≥ 35 °C (b) ≥ 65 (c) 150°C. Notes: Thin vertical lines are gas extraction wells, with screen intervals depicted by thicker grey portions. Purple cylinders represent higher CH_4:CO_2 ratio in gas than pink cylinders. The diameter of the pink and purple cylinders represent qualitative gas flowrate in wells (larger diameter being higher flow rates than smaller diameter cylinders).

V. Conclusions

- The project team established themselves as the authoritative technical experts on ETLFs through peer-reviewed publications, conference presentations, trade industry publications, webinars, continuing education, and meetings with various agencies and stakeholders. As a result, the technical, regulatory, and legal conversation about ETLFs has changed completely. When the project began, the common theme was fear regarding an unknown and highly unpredictable and potentially dangerous phenomenon. By the end of the project, the conversation shifted to confidence that the engineering community understands how to manage existing ETLFs and prevent future ETLFs.

- Members of project team are using knowledge developed through this project to assist owners resolve difficult conditions at their ETLFs and to improve the state-of-the-practice.

- Model simulations predicted that some wastes can release sufficient heat to alter the equilibrium state in MSW landfills, causing heat accumulation and elevated temperatures. Heat accumulation is exacerbated by conditions that hinder heat dissipation, such as very deep and very wide landfills cells where heat dissipation boundaries can be far from heat sources contributing to heat accumulation. Waste acceptance criteria, landfill geometry, waste placement criteria, and landfill operations should be considered in concert to prevent conditions that lead to excessive heat accumulation.

- Thermal properties of MSW used in heat transfer models like those described in this report can be estimated reliably if the density and water content of the MSW are known. Equations provided in this report can be used to make these predictions.

- The MSW pyrolysis experiments conducted in this study demonstrated that degradation of MSW under pyrolytic conditions creates charred materials and produces carbon monoxide, hydrogen, volatile organic compounds, and other gaseous byproducts. These pyrolysis byproducts are often observed in ETLFs because the MSW is undergoing pyrolysis - defined broadly as waste degrading thermally under anoxic and abiotic conditions. Some of these byproducts are also generated by MSW combustion, and in some cases improper inferences have been made that MSW in ETLFs is undergoing combustion. This improper inference must be avoided, as the actions taken to arrest combustion (e.g., shut down the gas system) can exacerbate heat accumulation in ETLFs and worsen existing conditions.

- Findings of the study indicate the importance of continuous review of landfill monitoring data for trends indicative of widespread elevated temperatures. Field data evaluated as part of this study demonstrate that ETLFs exhibit distinct characteristics that can be detected by monitoring programs. Early warning signs of a potential ETLF often are evident in temperature, fluid pressure, and leachate chemistry data. Continuous review and assessment of these data can assist in diagnosing ETLF

conditions, and provide data demonstrating how corrective actions are affecting an ETLF over time.

- Aggressive management of liquids and gases is necessary to prevent and control ETLFs. Liquid accumulation results in elevated hydrostatic pressure that is reported to increase the energetics of pyrolytic reactions. While the impact of increased pressure on thermal reactions could not be quantified, high hydrostatic pressure may also result in leachate seeps and flooded gas wells, both of which interfere with good management practice. Gases serve as volatile substrates for heat-generating reactions. Extracting gas aggressively removes a potential energy source in a landfill undergoing thermal abiotic reactions.

- While the initial hypothesis for the underlying cause of ETLFs focused on a trigger causing a self-propagating exothermic reaction, the findings of this study suggest that heat generating wastes can result in elevated temperatures and likely are the primary cause of ETLFs. For example, the modeling work highlighted the potential of ash, a waste commonly accepted in MSW landfills, as a heat source that could result in elevated temperatures similar to those observed in ETLFs. Strategies are needed to safely dispose of heat-generating wastes based on the reactivity of the waste and the relative quantity disposed. The models developed in this project can be used to estimate the mass of a given waste that can be disposed of without excessive heat accumulation. Use of these models is a viable approach for formulation of a waste acceptance strategy.

Ongoing Research

- EREF-funded research to develop methods to measure the heat generation potential of ash and aluminum under landfill-relevant conditions. A final report to EREF is expected in the second quarter of 2023.
- Research to understand factors that affect the extent of abiotic cellulose hydrolysis under landfill-relevant conditions. The research will be completed in late 2023.

VI. Materials and Methods

The methods that were used for model development, and measurement of abiotic thermal reactions and the thermal properties of MSW are presented in this section.

A. Model Development

The methods and governing equations that were used for development of the batch reactor model and the FEM-3DM are presented in this section. The material presented in the main body of the report is designed to provide the reader with an overview of the models and their governing equations without the distraction of detailed mathematical descriptions. Additional detail on model development is presented as Appendix D.

1. Batch Reactor Model

A model was developed to describe a single addition of MSW to a landfill, thus representing a relatively simple system for quantifying heat generation (Figure 6-1). The single addition of MSW was assumed to be a non-continuous and perfectly mixed closed

unit where biotic and abiotic reactions occur. Therefore, the landfill unit was modeled as a batch reactor. Based on the developed model, the temperature and concentrations do not vary spatially within the landfill unit, which was assumed to be surrounded by other waste with liquid and gas flux into and out of the unit volume. Water that enters with the waste as well as that from infiltration is considered. Since the system is closed and based on a single addition of MSW, gas and water movement only influence the transport of heat from the system but do not change the physical properties of the MSW. For this system, the outlet gas and liquid phases have the same temperature as the landfill unit. The model was developed to maximize flexibility with respect to user-specified input parameters in recognition of the site-specific nature of landfills as well as parameter uncertainty.

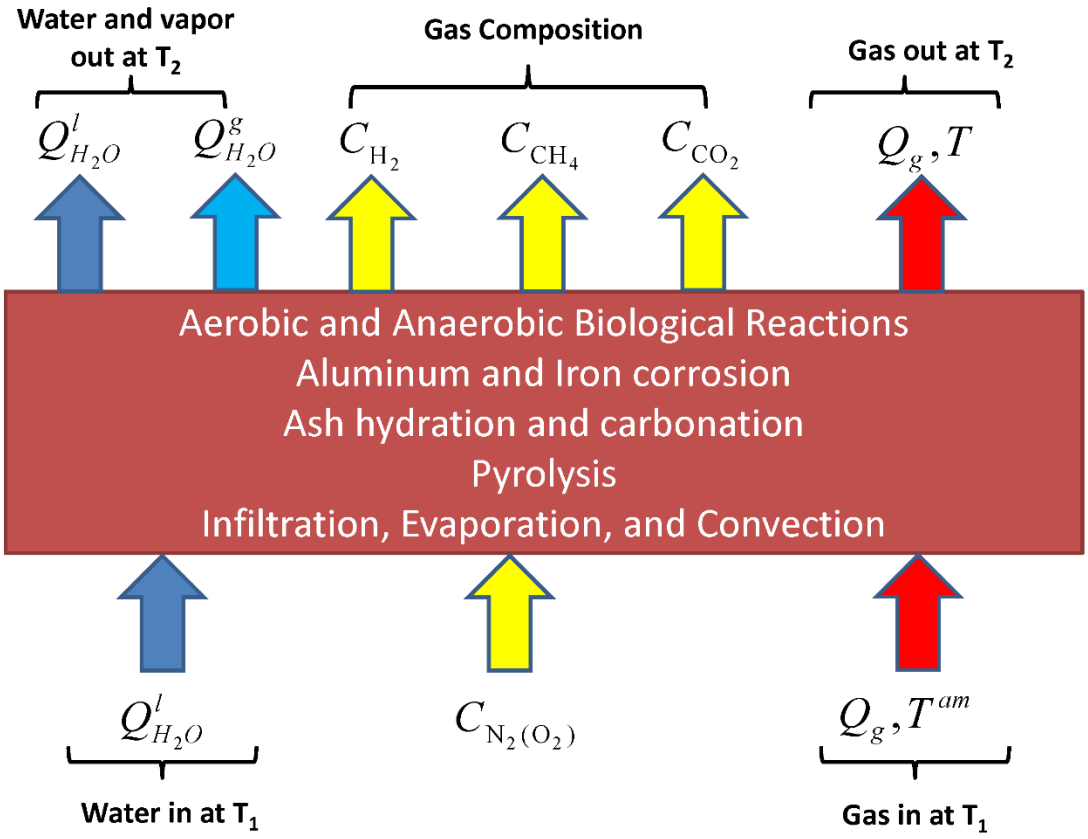

Figure 6-1. Schematic of the Landfill Batch Reactor Model. *Q* is flow rate, *T* is temperature, and *C* is concentration.

2. Governing Equations and Reactions

The model employs an energy balance, where heat accumulation is equal to the net heat influx and heat generation (Eq. 6-1).

$$\rho_s C_{p,s} V \frac{dT}{dt} = \sum_{i=anaer.\ metal,H_2,ash} R_i(-\Delta H_i)V + S_{O_2}(-\Delta H_{aer}) + \sum_{i=CH_4,CO_2} C_{p,i} R_i (T^{am} - T)V - \rho_{v,H_2O} L_{eva} \sum_{i=CH_4,CO_2,N_2} Q_i + \rho_{H_2O} C_{p,H_2O} A Q_{H_2O} (T^{am} - T) \quad (6\text{-}1)$$

where ρ_s and $C_{p,s}$ are the weighted average density and heat capacity of the buried waste, $V$and A are the volume and surface area of the landfill, R_i is the generation rate of the indicator species, ΔH_i is the heat (enthalpy change) of the chemical reactions, S_{O_2} is the biological O_2 consumption rate, ΔH_{aer} is the enthalpy change due to aerobic biodegradation, $C_{p,i}$ is the heat capacity of species *i*, T^{am} is the ambient temperature, *T* is the temperature in the landfill, ρ_{v,H_2O} is the density of saturated water vapor, L_{eva} is the latent heat of water evaporation ($-2400 \frac{kJ}{kg\ H_2O}$), ρ_{H_2O} and C_{p,H_2O} are the density and heat capacity of water, Q_i is the flow rate of gaseous component *i,* and Q_{H_2O} is the infiltration rate.

The left side of Eq. 6-1 represents heat accumulation in a landfill unit volume. The first term on the right side is the heat gain from chemical and anaerobic biodegradation reactions, the second term is the heat gain from aerobic biodegradation, and the third, fourth, and fifth terms are heat losses by convection, evaporation, and infiltration, respectively.

Convection includes gas and liquid transport through the landfill. The temperature of gases and liquid entering the system are user specified. Heat removal from the transport of landfill gas, which is comprised of CH_4, CO_2, and N_2, represents convection due to gas transfer. Determination of gas flow rates is described in the section on biodegradation reactions.

Liquid movement is based on infiltration, assuming that water percolates vertically through the landfill until it is removed in the leachate collection system. The model does not allow for liquid accumulation. Infiltration is based on an assumed rate of leachate generation [volume/(area-day)] (Table 6-1). The flow of gas and liquid in the landfill leads to convective heat transfer, which is proportional to the temperature difference between the landfill and inlet fluid temperatures. The effect of infiltration on landfill temperature can therefore be considered as the convection of water.

Phase changes of water will consume or release energy. Inlet LFG was assumed to be saturated with moisture at the initial gas temperature and LFG was assumed to remain saturated with increasing landfill temperatures. Thus, the evaporation of water from the waste to saturate LFG represents an energy sink. In contrast, if the temperature of refuse surrounding the landfill unit was cooler than the refuse in the unit, then as hot LFG flows to the surrounding waste, energy would be released due to condensation. In the batch reactor model formulation, variations in waste temperature and condensation could not be considered. These factors were incorporated in the FEM-3DM.

3. Aerobic and Anaerobic Biological Reactions

When waste is disposed in a landfill, some air (O_2 + N_2) is entrained at burial (Sanchez et al. 2010). This O_2 was assumed to be rapidly consumed and the resulting temperature increase is considered when specifying the initial waste temperature. As freshly buried waste is by definition near the landfill surface, heat loss will be high and the initial O_2 content was assumed to be an insignificant source of energy. Of more potential significance is the impact of air intrusion that may result from excess vacuum applied to the landfill's gas collection and control system (GCCS). Ideally, GCCS operation would not result in air intrusion; but the presence of N_2 in LFG suggests that some air intrusion occurs. The available O_2 was estimated from the LFG production rate (described below) and the user-specified N_2 concentration. Consequently, the volume of O_2 intrusion was estimated as 21/78 times the volume of N_2 based on the composition of air.

Several potential substrates may react with O_2. For simplicity, two are considered in this analysis, methane and cellulose (Eqs. 6-2 and 6-3). If the bacteria that convert CH_4 to CO_2 in the presence of O_2 (methanotrophs) survive without O_2, then aerobic methane oxidation (Eq. 6-2) is likely to dominate O_2 consumption. While the long-term survival of methanotrophs has not been tested in landfills, they have been reported to survive for ~170 years in deep, aged lake sediments (Rothfuss et al. 1997).

$$CH_4 + 2O_2 \rightarrow CO_2 + 2H_2O \qquad \Delta H = -27822 \frac{kJ}{kg\ O_2} \tag{6-2}$$

In contrast, if methanotrophs do not survive, then cellulose oxidation (Eq. 6-3) will likely govern. The effect of both substrates (CH_4 and cellulose) is considered in the Results.

$$(C_6H_{10}O_5)_n + 6nO_2 \rightarrow 6nCO_2 + 5nH_2O \qquad \Delta H = -17360 \frac{kJ}{kg\ cellulose} \tag{6-3}$$

The biological O_2 consumption rate was calculated using Eq. 6-4.

$$S_{O_2} = \frac{21}{78} \rho_{O_2} Q_{N_2} \tag{6-4}$$

where ρ_{O_2} is the density of O_2, and Q_{N_2} is the flow rate of N_2. Since aerobic reactions are much faster than anaerobic reactions, O_2 was assumed to be consumed instantaneously after entering the landfill.

The ΔH for the biological reactions in Eqs. 6-2 and 6-3 and below does not consider that some energy associated with substrate conversion is used for cell synthesis. As such, the enthalpies used in the model represent an upper limit on the amount of energy released.

Three biodegradable components of MSW (carbohydrates, protein, lipids) were considered as substrates for anaerobic (i.e., CH_4) generation. The stoichiometry and energetics for each substrate are presented in Eqs. 6-5 to 6-7, with carbohydrates (cellulose, hemicellulose, starch) represented as cellulose.

$$(C_6H_{10}O_5)_n + nH_2O \rightarrow 3nCH_4 + 3nCO_2 \qquad \Delta H = -1672 \frac{kJ}{kg\ cellulose} \tag{6-5}$$

$$8C_{16}H_{24}O_5N + 66H_2O \rightarrow 75CH_4 + 53CO_2 + 8NH_3 \qquad \Delta H = -1295 \frac{kJ}{kg\ protein} \tag{6-6}$$

$$2C_{16}H_{32}O_2 + 14H_2O \rightarrow 23CH_4 + 9CO_2 \qquad \Delta H = -1826 \frac{kJ}{kg\ lipids} \tag{6-7}$$

The rate of heat release was calculated from the rate of CH_4 generation as described here. In practice, US EPA's LFG emissions model (LandGEM) is typically used to estimate CH_4 generation and the default value for the CH_4 generation rate constant (k_m) in non-arid regions is 0.04 yr^{-1} (US EPA 1998, 2005). The LandGEM modeling approach was adopted here. Using k_m for MSW, de la Cruz and Barlaz (2010) described a method to estimate waste component specific decay rates (k_{mi}) for the major biodegradable components of MSW (food waste, grass, leaves, various types of paper). The CH_4 generation rate was calculated for each waste component using Eq. 6-8 and previously reported values for L_0 and k_{mi} for each waste component (Table 6-2). The CH_4 generation rate was then used with the stoichiometric relationships defined in Eqs. 6-5 to 6-7 to estimate the substrate biodegradation rate and subsequent rate of heat release. With the exception of food waste, all biodegradation was attributed to carbohydrates. The chemical composition of each waste component and mixed MSW is described in Tables 6-3 and 6-4.

$$Q_{ni} = f_{CH_4}(T) k_{mi} L_{0i} \sum_{p=0}^{n} \sum_{q=0.0}^{0.9} \frac{M_p}{10} e^{-k_{mi} t_{p,q}} \tag{6-8}$$

where Q_{ni} is the CH_4 generation rate in year n of biodegradable component i, $f_{CH_4}(T)$ is defined in Eq. A1, k_{mi} is the first-order decay rate constant of biodegradable component i, L_{0i} is the CH_4 generation potential of biodegradable component i, M_p is the waste mass placement in year p, q is an intra-annual time increment used to calculate CH_4 generation, and t is time. For the batch reactor model, only one mass of MSW was disposed at one time. As described in the following section, a waste disposal strategy and schedule was incorporated into the FEM-3DM.

While methanogens have been reported to survive at temperatures as high as 89°C, this is not typical (Amend and Shock 2001). Thermophilic methanogens in anaerobic digesters and methanogenesis from acetate are reported to have an upper temperate limit of ~75°C (Zinder et al. 1984, Nozhevnikova et al 1999, Sosnowski et al. 2003, Nielsen et al. 2004).

To account for the influence of temperature on CH_4 generation, an inhibition function $[f_{CH_4}(T)]$ was developed and is presented in Appendix D.

4. Chemical Reactions

Ash disposed in landfills typically contains several oxides/hydroxides including $CaO/Ca(OH)_2$, $MgO/Mg(OH)_2$, $Na_2O/NaOH$, K_2O/KOH, and P_2O_5 (Speiser et al. 2000, Rendek et al. 2007, Morales-Flórez et al. 2015). The hydration of CaO is illustrated in Eq. 6-9 and hydration of other oxides is given in Appendix D.

$$CaO + H_2O \rightarrow Ca(OH)_2 \qquad \Delta H = -1164 \frac{kJ}{kg\ CaO} \tag{6-9}$$

Ultimately, the generated hydroxides are converted to carbonates by reacting with CO_2, as described by Eq. 6-10 for $Ca(OH)_2$ and Appendix D for other hydroxides (Li et al. 2007).

$$Ca(OH)_2 + CO_2 \rightarrow CaCO_3 + H_2O \qquad \Delta H = -1718 \frac{kJ}{kg\ Ca(OH)_2} \tag{6-10}$$

Both water and CO_2 were assumed to be present in excess and both hydration and carbonation are explored in the results.

The presence of oxides versus hydroxides is specific to the waste source and the manner in which the ash is handled prior to disposal. As such, the user can specify the content of the ash and the fraction that is present as oxides and hydroxides (default values are presented in Table 6-5). The rates of ash hydration and carbonation were assumed to follow first-order consecutive reaction models (Eqs. 6-11 and 6-12).

$$R_{hyd} = c_{oxide} k_{hyd} \tag{6-11}$$

$$R_{crb} = c_{hydroxide} k_{crb} \tag{6-12}$$

where R_{hyd} and R_{crb} are the rates of ash hydration and carbonation, c_{oxide} and $c_{hydroxide}$ are the concentration of oxides and hydroxides in the ash, and k_{hyd} and k_{crb} are the reaction rate constants for hydration and carbonation, respectively.

Landfills receive Al and Fe in elemental form from both MSW and special wastes that may include Al processing waste and auto shredder residue (Calder and Stark 2010, Ahmed et al. 2014). Both Al and Fe have been reported to undergo corrosion reactions (Eqs. 6-13 and 6-14).

$$Al + 3H_2O \rightarrow Al(OH)_3 + \frac{3}{2}H_2 \qquad \Delta H = -15922\frac{kJ}{kg\ Al} \tag{6-13}$$

$$Fe + CO_2 + H_2O \rightarrow FeCO_3 + H_2 \qquad \Delta H = -1268\frac{kJ}{kg\ Fe} \tag{6-14}$$

The rate and extent of corrosion will be governed by the surface area of the metal as well as the presence of protective coatings or oxides, and environmental conditions. To model heat generation from the corrosion of Al and Fe, corrosion was assumed to occur uniformly across the metal surface at a rate specified in mm·yr^{-1}. To account for pitting type corrosion, which would not impact the entire surface, sensitivity analyses with reduced effective surface areas may be considered. As discussed in the Results, an improved understanding of metal corrosion under landfill relevant conditions is needed.

The content of Al and Fe in MSW was coupled with metal sheet thickness and metal density to estimate the total surface area available for corrosion. Three categories of Al were considered (containers, foil, other) to allow for three thicknesses and three alloys, while two categories with two thicknesses were considered for Fe (containers, other). The characteristics of each metal are presented in Table A2.

The reaction rates for anaerobic metal corrosion (Al and Fe) are described by Eqs. 6-15 and 6-16:

$$R_{Al}^{i} = \rho_{Al}\alpha_{Al}^{j}A_{Al}^{i} \tag{6-15}$$

$$R_{Fe}^{i} = \rho_{Fe}\alpha_{Fe}^{j}A_{Fe}^{i} \tag{6-16}$$

where R_{Al}^{i} and R_{Fe}^{i} are the reaction rates of metal source *i* (*i*=Al or Fe containers, Al foil, and other Al or Fe in Table A2), ρ_{Al} and ρ_{Fe} are the density of Al and Fe, α_{Al}^{j} and α_{Fe}^{j} are the corrosion rates of metal alloy *j*, and A_{Al}^{i} and A_{Fe}^{i} are the surface area of metal *i*.

Hydrogen is a product of metal corrosion and can be converted to CH_4 by hydrogenotrophic methanogens (Eq. 6-17). Since CO_2 is a major constituent in LFG, the H_2 generated was assumed to be consumed instantaneously at the rate at which it is generated subject to the temperature inhibition defined in Eq. A1.

$$4H_2 + CO_2 \rightarrow CH_4 + 2H_2O \qquad \Delta H = -20625\frac{kJ}{kg\ H_2} \tag{6-17}$$

Carboxylic acids are anaerobic biodegradation intermediates. When the microbial activity involved in waste decomposition is balanced, carboxylic acids do not accumulate and acid-base reactions are of little energetic consequence. However, there are scenarios in which carboxylic acids accumulate and the landfill pH may decrease to ~5. In this scenario, acidic leachate may percolate through the landfill and be neutralized by hydroxide ions generated by ash hydration and metal corrosion processes and/or the buffer capacity of the refuse. Acid-base neutralization was represented in the model with the simplifying assumption that all carboxylic acids are present as acetic acid (Eq. 6-18). Neutralization was assumed to be instantaneous and the concentration of acetic acid is user-specified.

$$CH_3COOH + OH^- \rightarrow CH_3COO^- + H_2O \qquad \Delta H = -57\frac{kJ}{mol} \tag{6-18}$$

5. Model Parameterization and Input Assumptions

The parameters required to describe the physical characteristics of the landfill and the waste are presented in Table 6-1. As there is considerable overlap between the batch reactor model and FEM-3DM, default model parameters for both models are presented in Table 6-1. MSW composition and physical properties are given in Table 6-2, while the chemical composition of the MSW was estimated from the composition of each waste component (Table 6-3). The biodegradable components in the waste include carbohydrates (25.4%), protein (4.4%) and lipids (8.3%), and the complete chemical composition is given in Table 6-4. The values in Tables 6-1 and 6-4 represent a base case.

Table 6-1. Default model parameters used to describe landfill characteristics[a]

Parameter	Unit	Value	Comments and citations
Initial mass	Mg	544	Daily waste mass for medium sized landfill (20% moisture) (BRM)
Waste intake rate (R_{int})	$kg \cdot yr^{-1}$	8.28×10^8	Yearly waste mass for medium sized landfill (2500 US tons per day) (FEM-3DM)
Depth	m	30	Assumption (BRM)
Infiltration rate	$m^3 \cdot m^{-2} \cdot yr^{-1}$	0.137	Value used in industry for landfills in regions receiving ~100 cm rain$\cdot yr^{-1}$
Infiltration time	yr	20	Assumed time prior to placement of low conductivity final cover (BRM)
Initial temperature	°C	40	Assumed in consideration of some self-heating associated with initial aerobic decomposition (BRM)
Initial temperature	°C	20	Assumed in consideration of some self-heating associated with initial aerobic decomposition (FEM-3DM)
Ambient temperature	°C	20	Assumed environmental temperature
Waste density	$kg \cdot m^{-3}$	890	Approximate industry average
Ash density	$kg \cdot m^{-3}$	1281	Approximate industry average
Waste heat capacity	$kJ \cdot kg^{-1} \cdot °C^{-1}$	1.32	Estimated as the sum of the heat capacity of individual components multiplied by their fractions (Yoshida et al. 1997). Default waste composition data given in Tables 6-2 to 6-4 and heat capacities given in Table 6-2.
Ash heat capacity	$kJ \cdot kg^{-1} \cdot °C^{-1}$	0.8	Liang et al. (2008)
Evaporation rate constant	day^{-1}	1	Assumption (FEM-3DM)
CH_4 generation rate constant (k_m)	yr^{-1}	component specific	Data for k_m given in Table 6-2.

Table 6-1. Default model parameters used to describe landfill characteristics[a] (continued)

Parameter	Unit	Value	Comments and citations
CH_4 Production potential (L_0)	m^3 $CH_4 \cdot Mg^{-1}$ waste	component specific	Data for L_0 given in Table 6-2.
N_2	%	2	Used to quantify air intrusion (BRM)
N_2	%	4	Used to quantify air intrusion (FEM-3DM)
Corrosion rate of Al (alloy 3004)	$mm \cdot yr^{-1}$	0.003	Eashwar et al. (1990)
Corrosion rate of Al (alloy 1100)	$mm \cdot yr^{-1}$	2.54×10^{-4}	Ezuber et al. (2008)
Corrosion rate of coated Al (alloy 3004)	$mm \cdot yr^{-1}$	5.17×10^{-4}	Shabani-Nooshabadi et al. (2009)
Corrosion rate of steel	$mm \cdot yr^{-1}$	5×10^{-4}	Smart et al. (2001) (BRM)
Corrosion rate of coated steel	$mm \cdot yr^{-1}$	2.54×10^{-4}	Smith et al. (1973) (BRM)
Rate of ash hydration	yr^{-1}	0.5	Assumption
Rate of ash carbonation	yr^{-1}	0.1	Assumed rate is 20% of hydration rate based on literature from other environments (Morales-Flórez et al. 2015)
Acetic acid concentration	$g \cdot L^{-1}$	35	Assumption (BRM)

a. BRM = batch reactor model only; FEM-3DM = finite elemental model reactor only.

Table 6-2. Characteristics of MSW as discarded

		Weight (%[a])	heat capacity (kJ/kg·°C)	Moisture (%)	L_0 (m^3 CH_4/Mg waste)[b]	k_m (yr^{-1})[c]
Food	Total	21.5	1.72[d]	79.0[e]	458.5[f]	0.096
	Carbohydrate[g]	22.4[g]	1.72[d]	79.0[e]		0.096
	Lipids[g]	38.9[g]	1.72[d]	79.0[e]		0.096
	Protein[g]	20.4[g]	1.72[d]	79.0[e]		0.096
Wood	Total	8.1	1.36[d]	10.3[h]	17.8[i]	0.03[j]
Plastics	PET	2.3				
	HDPE	3.1				
	PVC	0.5				
	LDPE/LLDPE	4.3	1.80[k]			
	PLA	0				
	PP	4.5				
	PS	1.4				
	other plastics	2.0				
Glass	Total	5.1	0.66[d]			
Metals	Ferrous	7.2	0.66[d]			
	Aluminum	1.7	0.93[d]			
	other nonferrous	0.4	0.93[d]			
Yard trimmings	Total	8.3	1.36[d]	60.0[l]		
	Grass[m]	2.5			194.8[n]	0.6[j]
	Leaves[m]	3.3			65.3	0.114
	Branches[m]	2.5			59.4[o]	0.03[j]
Paper	Newsprint	1.6	1.34[d]	6.0[l]	74.3	0.022
	Old corrugated containers (OCC)	2.1	1.34[d]	6.0[l]	195.1	0.013
	Mixed paper	11.6	1.34[d]	6.0[l]	148.7	0.021
Textile	Total	7.9	1.3[d]	10.0[l]		
	Cotton[p]	1.6			263.6[q]	0.02[q]
	Synthetic[p]	6.3				
Leather		2.2	1.59[k]			
Other		4.4	0.85[k]			
Total		100	1.32[r]	19.7		

a. Data were obtained from the U.S. EPA (2015). Tires were excluded as they are typically not buried in MSW landfills.
b. L_0, the CH_4 generation potential, from Hodge et al. (2016), unless otherwise noted.
c. CH_4 generation rate constants were obtained from Hodge et al. (2016), unless otherwise noted.

d. Heat capacities from Miller and Clesceri (2002).
e. Weighted average based on the moisture contents of various food wastes (grocery, restaurant, university dining hall, hotel) reported in Lopez et al. (2016).
f. Weighted average of carbohydrate (cellulose, starch, and hemicellulose), lipids, and protein. L_0 of carbohydrate, lipids, and protein were calculated by multiplying the stoichiometric methane potential (Eqs.6-5 to 6-7) by the fraction of the mass loss for each compound (Lopez et al. 2016). The stoichiometric yields of carbohydrates, lipid and protein were calculated to be 414.8, 1006.3 and 677.4 m^3 CH_4/dry Mg, respectively.
g. Values are the average content across several types of food waste reported in Lopez et al. (2016) and are reported as a percentage of food waste.
h. Weighted average based on the moisture contents of residential and commercial wood waste in Wang et al. (2011).
i. L_0 of wood is the average of red oak (33.3), radiata pine (0.5), spruce (7.5), medium density fiberboard (4.6), plywood (6.3), particle board (5.6), oriented strand board-hardwood (84.5), and oriented strand board, softwood (0) from Wang et al. (2011).
j. k of wood, grass, and branches were obtained from de la Cruz and Barlaz (2010).
k. Heat capacities from Hanson et al. (2013).
l. Moisture content from Staley and Barlaz (2009).
m. Weighted average based on relative contribution of grass (30.3%), leaves (40.1%), and brush (29.6%) (Oshins and Block 2000).
n. L_0 of grass from Levis and Barlaz (2014).
o. L_0 of branches from Wang and Barlaz (2016).
p. It was assumed that textiles are composed of 20% of cotton and 80% of synthetic (weight basis).
q. It was assumed that the L_0 and k of cotton are equal to the value of office paper.
r. The heat capacity of solid waste was calculated based as a weighted average.

Table 6-3. Chemical composition of biodegradable waste components[a]

Components		Carbohydrate[b] (%)	Lignin (%)	Protein (%)	Lipids (%)
Food[c]		22.44		20.38	38.90
Wood[d]		57.46	28.33		
Yard trimmings					
	Grass[e]	38.55	25.00		
	Leaves[e]	25.80	43.80		
	Branches[e]	53.80	32.60		
Paper	Newsprint[f]	70.15	15.25		
	OCC[f]	76.80	14.55		
	Mixed paper[g]	73.76	10.89		
Textile	Total				
	Cotton[h]	90.70	2.70		
	Synthetic				
Total[i]		**25.37**	**7.04**	**4.37**	**8.35**

a. Data given as % of dry weight except the total which is given as % wet weight for use in the model. Moisture contents are given in Table 6-2.
b. The carbohydrate content includes cellulose, hemicellulose, and starch.
c. Weighted average based on the chemical compositions of various food wastes (grocery, restaurant, university dining hall, hotel) reported in Lopez et al. (2016).
d. The weighted average values of wood were estimated based on the chemical compositions of residential and commercial wood waste in Wang et al. (2011).
e. The carbohydrate content of grass is the average of the carbohydrate for grass and grass-2 in Eleazer et al. (1997). The same approach was also applied to calculate the carbohydrate and lignin contents of leaves and branches.
f. The carbohydrate content of newsprint and old corrugated containers (OCC) was estimated based on the cellulose, hemicellulose, and lignin content of newsprint and CC in Wang et al. (2013).
g. The carbohydrate and lignin content of mixed paper is the average of the values for newsprint, OCC, and copy paper (CP) in Wang et al. (2013).
h. Data was obtained from Dorez et al. (2014).
i. Calculated from the chemical content in this table and the waste composition (as discarded) given in Table 6-2.

Table 6-4. Biodegradable and reactive constituents in MSW considered in model

Constituents	Content (wt. %)
Carbohydrate[a]	25.4
Lignin	7.0
Protein	4.4
Lipids	8.3
Al[b]	1.7
Fe[b]	7.2
Other constituents[c, d]	46.0

a. The carbohydrate content includes cellulose, hemicellulose, and starch.
b. The Al and Fe contents were obtained from the U.S. EPA as described in Table 6-2 (US EPA 2015).
c. Other constituents include plastics (18.0%), glass (5.1%), synthetic textiles (1.3%), and other materials.
d. For some simulations, the waste was assumed to include combustion ash (base case - 10%) and the composition of MSW was diluted accordingly. Ash composition is given in Table 6-5.

Table 6-5. Chemical constituents that undergo hydration and carbonation in municipal solid waste incinerator (MSWI) bottom ash samples[a]

Constituents	Weight (%)	Hydrated at burial (%)
CaO	19.49	0
MgO	2.59	0
Na_2O	4.52	0
K_2O	1.19	0
P_2O_5[b]	1.65	0
inactive constituents[c]	70.58	0

a. Values are the average content across 5 MSWI samples reported in Rendek et al. (2007) and are reported as a percentage of bottom ash.
b. Undergoes hydration only.
c. Other constituents include SiO_2, Al_2O_3, Fe_2O_3, TiO_2, and MnO.

6. Finite Element Model Development

The landfill was modeled as a square prism (Figure 6-2). The height of the landfill was assumed to be 80 m (unless otherwise noted) and its width and length are calculated based on daily waste disposal rate ($R_{\text{int}}\,\text{kg}\cdot\text{day}^{-1}$). The 80 m tall landfill is composed of 16 - 5 m high layers (Figure 6-2a). There are 9 cells in each layer for a total of 144 cells. Assuming a waste intake rate of 2500 tons/day (2.27×10^6 kg/day) and the time to fill each cell (t_{cell}) is 15 days, the volume of each cell is 38224 m^3 based on an assumed waste density (ρ_s) of 1500 lb/yd^3 (890 kg/m^3). The site fills in 2160 days or 5.9 years at 365 days per year. Therefore, the length and width of each cell is 87.4 m and the length and width of the landfill is 262.2 m. The waste placement strategy is illustrated in Figures 6-2b and 6-2c where MSW is buried in a systematic pattern within each layer and from layer to layer until the landfill is full.

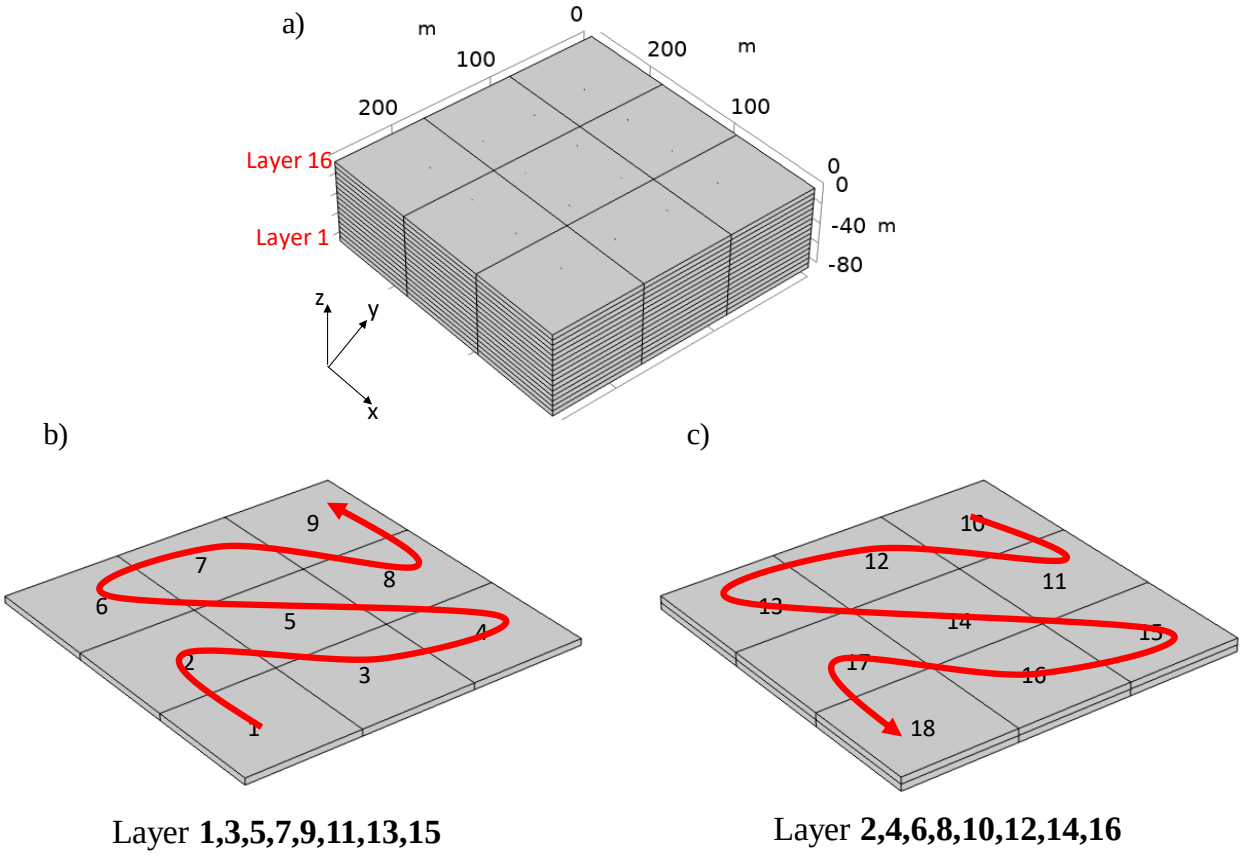

Figure 6-2. Geometry of the three-dimensional finite element model (a) and the waste disposal strategy (b and c). The burial sequences are marked as Cells 1 to 9 in odd layers and as Cells 10 to 18 in even layers.

The landfill is modeled as a three-phase (gas, liquid, and solid) system with the solid phase (MSW/other waste) modeled as a rigid porous medium of constant porosity. The composition of MSW that is placed in each cell can vary and this variation informs physical and thermal properties of each cell as well as the gas production rate. MSW composition is user-defined and the composition used for the batch reactor model was used here as well (Tables 6-2 to 6-4). The gas phase is a four-component mixture (H_2O, CO_2, N_2 and CH_4) while the liquid phase includes infiltrated rainwater and the intrinsic moisture in waste at the time of placement. The vertical perforated PVC gas wells are under vacuum and remove LFG at the gas generation rate. Assuming a gas well density of 0.43 wells per ha (1 well per acre), there are 16 evenly distributed gas wells; each 15 cm in diameter and 60 m in length.

The heat generation terms include aerobic and anaerobic biodegradation, ash hydration and carbonation, and Al corrosion and are the same as described for the batch reactor model. The incorporated heat transfer mechanisms include conduction, evaporation, and condensation, and liquid and gas convection. The FEM-3DM allows water to evaporate and hot gas from one location to move to a cooler location and condense with the release of energy. All phases have the same temperature at the thermal equilibrium state; thus, only one heat balance equation is required for the three-phase system. All parameters required to describe the physical characteristics of the landfill and the waste are presented in Table 6-1.

The detailed equations that describe the FEM-3DM and the solver used in the mode are presented in Appendix D.

B. Thermal Reactions of MSW under Abiotic Conditions

Four sets of experiments were conducted to evaluate the potential for MSW to undergo abiotic thermal reactions (Table 4-2). Phases 1 and 2 were used as baseline experiments of relatively short duration to obtain initial data and to establish conditions for the longer duration study (~1 year). Phase 1 experimentation was in a high-pressure system (382 kPa) using a N_2 (UHP grade, Praxair) atmosphere at 70 °C (158 °F). The pressure (382 kPa) was selected based on reported field investigations indicating elevated pressure in some ETLFs. The temperature was kept constant, and the N_2 environment was used to understand MSW behavior in an inert environment. Testing lasted four months after which the contents were removed and characterized. Biological inhibitors were not used Phase 1 as biological activity was considered dormant at the temperatures tested. However, biological inhibitors were added in subsequent phases as a precaution against biological activity. In Phase 2, the reactor system was again pressurized with N_2 to 382 kPa and the temperature was increased incrementally from 50 °C to 200 °C (122 to 392 °F).

Phase 3 replicated the high-pressure system in Phases 1 & 2 but included a low (atmospheric) pressure reactor as a control. The headspace in Phase 3 was a 50:50 mixture of CO_2 and CH_4. The temperature was initially set to 50°C (122 °F) and subsequently increased in steps to predetermined targets up to ~200°C (392 °F). The majority of the study was performed between 50 and 121 °C (122 to 250 °F), however two higher temperatures [177°C (350 °F) and 204°C (400 °F)] were used to study the effect of extreme temperature on H_2 concentration. In Phase 4 reactors were operated at a specific energy

input which allowed the temperature to vary but made it possible to explore the energy input required to initiate an exothermic pyrolytic reaction. A controlled energy input was achieved through the same heater assembly (Parr Instruments Model 4913) as used in Phases 1 – 3, but in Phase 4, the voltage was controlled to a pre-determined set point.

A synthetic MSW was used for all the experiments. It was comprised of plastic, wood, metal, paper, fabric, and other wastes, consistent with the average MSW composition in the United States as described in the EPA waste characterization report (U.S. EPA 2015) (Table 6-6). The waste had a Carbon (C), Hydrogen (H), Nitrogen (N), and Oxygen (O) content of 52.0, 7.6, 1.6, 38.8 wt.%, respectively. The density of the uncompacted waste that was charged into the reactors was about 180 kg/m^3 and the reactors contained 200 to 600 gm of waste depending on the experiment.

The sample loading procedure was to charge the reactor with wet waste followed by a purge with the pressurizing gas to eliminate air from the vessel. To wet the waste, it was soaked for 2 hr in deionized water plus a biological inhibitor (Phases 2 – 4) to ensure that the sample was saturated prior to reactor loading. The initial moisture content of the waste was 55 % (mass water/total mass). Biological reactions were eliminated by the addition of 2,2-dibromo-3-nitrilopropionamide (DBNPA) (0.02 gm per gm MSW) and streptomycin (0.0008 gm/gm MSW).

1. Reactor Assembly

For the tests conducted at 382 kPa, a high-pressure reactor with a high temperature vessel assembly was used (Parr Instruments Model 4642) (Figure 6-3). The same reactor was used in all four phases for the testing at 382 kPa. The vessel has an internal volume of 2 liters and has multiple ports for gas exchange. The vessel was sealed with a high-temperature flexible graphite gasket using 47 N-m of torque, allowing a maximum pressure rating of 13 MPa. The reactor pressure was maintained using a backpressure regulator and measured using a transducer on the cover of the vessel. The reactor waste mass and headspace temperatures were measured by a J-type thermocouple (Omega Engineering, HJQIN-18G-18) inserted into a thermowell of the reaction vessel. The thermocouple also served as the reference for the proportional-integral-derivative temperature controller (Parr Instruments Model 3825). The temperature controller served to heat and control the temperature via a heater assembly (Parr Instruments Model 4913) which encases the reactor vessel. For low-pressure studies, a glass reactor (Chemglass Life Sciences) was used with the same setup and connections as the high-pressure reactor with the exception that there was no back-pressure regulator required.

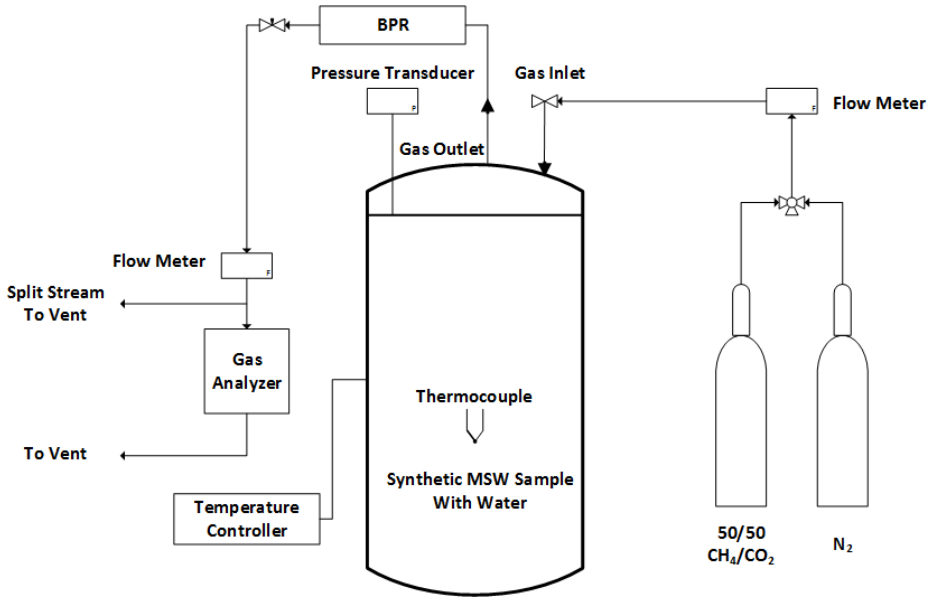

Figure 6-3 Schematic of high-pressure reactor used for all experiments (BPR = back pressure regulator)

2. Reactor Monitoring

The reactor outlet was connected to a micro-gas chromatograph (model 3000, Inficon) used for online analysis of the evolved gas. Gas was extracted through a needle valve mounted on the reactor head assisted by the internal microGC pump. The microGC was equipped with a thermal conductivity detector (TCD) and two columns, a Mol-Sieve column for the separation of helium (He), H_2, oxygen (O_2), N_2, CH_4, CO and a Plot-U column for the separation of CO_2, ethylene (C_2H_4), ethane (C_2H_6) and propylene/propane (C_3H_6/C_3H_8). This allowed for the separation of all permanent gases that would be produced during the course of the experiment. The extracted gas was injected into the GC without any pretreatment/cleaning except condensation of trapped moisture.

Table 6-6 Composition of MSW used in the reactors

Component	Normalized Discards Composition (%)	Notes
Newsprint	1.63	SONOCO MRF (Raleigh NC)
Office Paper	0.76	SONOCO MRF (Raleigh NC)
Magazines	0.40	SONOCO MRF (Raleigh NC)
Corrugated Containers	2.13	SONOCO MRF (Raleigh NC)
Other Paper	10.57	SONOCO MRF (Raleigh NC)
Aluminum Cans	0.35	SONOCO MRF (Raleigh NC)
Steel Cans	0.34	SONOCO MRF (Raleigh NC)
Other Metals	6.05	NC State Machine Shop, CCEEE
PET Containers	1.22	SONOCO MRF (Raleigh NC)
HDPE Containers	1.01	SONOCO MRF (Raleigh NC)
Other Plastics	15.91	SONOCO MRF (Raleigh NC)
Glass Containers	3.76	SONOCO MRF (Raleigh NC)
Other Glass	1.40	SONOCO MRF (Raleigh NC)
Rubber and Leather	3.98	Goodwill
Textiles	7.89	Goodwill
Food Waste	21.65	Synthetic formulation (rabbit food)
Yard Waste	8.36	NC State recycling center
Wood	8.17	NC State recycling center (untreated); Home depot (treated)
Other	4.43	Proportionate from other components above

C. Thermal Properties Characterization

Thermal conductivity of the waste was measured using a thermal conductivity cell (TC) with a guarded hot-plate apparatus as shown schematically in Fig. 6-4a. The chamber was a cylinder of chlorinated polyvinyl chloride (CPVC) with an internal diameter of 300 mm. The temperature gradient was applied by the temperature differential between a hot plate at the base and a cold plate at the top. Joule heating was used for the hot plate, with the temperature maintained ± 0.5 ^{o}C using a temperature controller. The cold plate was maintained at lower temperature by circulating cool water through the plate. The base and sides of the cell were covered with a ceramic blanket to minimize heat loss during the test. Different overburden pressures were applied using a hydraulic ram attached to the upper plate in the cell. Waste compression was measured with two linear variable differential transformers (LVDTs).

Total heat flux from the hot plate was recorded by monitoring the total time on-stage. Temperatures within the cell at the surfaces of the hold and cold plates were monitored using Type-T thermocouples attached to a solid-state multiplexer. Data were collected using a using LabVIEW program and data acquisition card using a PC. Thermal conductivity (k_T) was calculated from the heat flux (Q) and temperature difference between the upper and lower plates using:

$$k_T = \frac{Q\,L}{T_h - T_c} \tag{6-19}$$

where T_h is the temperature in hot plate, T_c is the temperature in cold plate, and L is the thickness of the waste between the plates. The hot plate was set at 50 °C and the cold plate was set at 4°C for all experiments. The cell was covered with a ceramic blanket to minimize the loss of heat during the test.

Synthetic waste was tamped into the cylinder in a 100-mm-thick layer using a wooden tamper to an initial dry density of approximately 0.3 Mg/m^3, corresponding to loose waste near the surface. Prior to placement, the waste was mixed with deionized (DI) water using a spray bottle and trowel to a target gravimetric water content of 25, 45, or 60% (dry weight basis). Air-dry waste (water content = 6%) was also tested. The moistened waste was placed in a sealed plastic bag and tempered for 24 hr prior to testing to ensure uniformity. Measurements in the TC were conducted at sequentially higher normal stresses to simulate different depths within a landfill (e.g., 2, 50, 100, 200, 300, and 400 kPa). Vertical load was applied by a piston controlled using a LabVIEW system. A linear variable differential transformer was used to measure compression of the MSW after applying the normal stress. Thermal conductivity measurements were initiated once compression of the waste became negligible under the imposed stress.

Specific heat capacity of the fresh synthetic MSW waste was measured using with a dual needle sensor (Fig. 6-4b). One needle is used for heating and the other for sensing the increase in temperature associated with heat from the adjacent heating needle. The temperature data were interpreted with the line-source solution methodology described in Bristow et al. (1994). The needles were 1.3-mm in diameter and 30 mm long, with 6 mm spacing. Specific heat capacity tests were conducted on fresh synthetic MSW at 25% and 60% water content.

Thermal conductivities of the fresh and degraded wastes for different stresses and water contents are summarized in Tables 6-7 and 6-8.

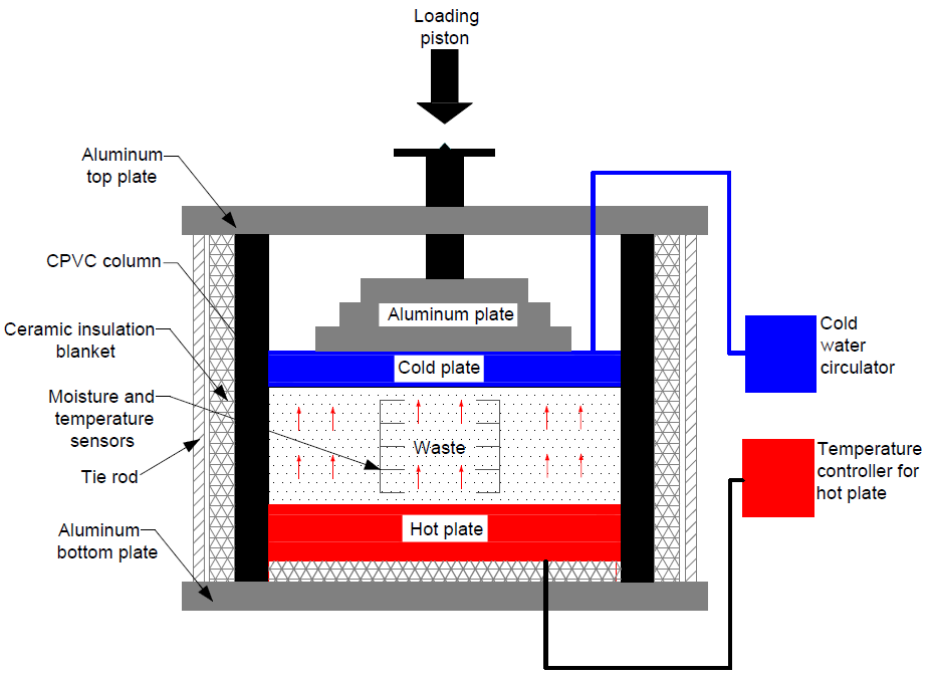

(a)

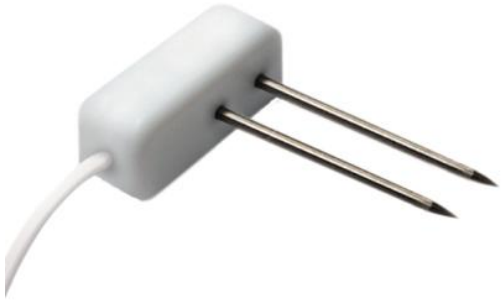

(b)

Figure 6-4. Schematic of thermal conductivity cell to measure thermal conductivity of waste at various confining stresses (a) and dual needle probe used for measuring specific heat capacity (b).

Table 6-7. Thermal conductivity of fresh waste.

Confining Pressure (kPa)	Gravimetric Water Content of Test Specimen (%)							
	6		25		45		60	
	Dry Density (Mg/m^3)	Thermal Conductivity W/(m-°C)	Dry Density (Mg/m^3)	Thermal Conductivity W/(m-°C)	Dry Density (Mg/m^3)	Thermal Conductivity W/(m-°C)	Dry Density (Mg/m^3)	Thermal Conductivity W/(m-°C)
2	0.30	0.34	0.31	0.43	0.31	0.47	0.30	0.49
50	0.46	0.37	0.47	0.48	0.43	0.57	0.38	0.59
100	0.54	0.40	0.58	0.52	0.58	0.57	0.44	0.65
200	0.60	0.43	0.63	0.57	0.62	0.69	0.58	0.72
300	0.65	0.42	0.67	0.63	0.66	0.74	0.70	0.79

Table 6-8. Thermal conductivity of degraded waste.

Confining Pressure (kPa)	Gravimetric Water Content of Test Specimen (%)							
	6		25		45		60	
	Dry Density (Mg/m^3)	Thermal Conductivity W/(m-°C)	Dry Density (Mg/m^3)	Thermal Conductivity W/(m-°C)	Dry Density (Mg/m^3)	Thermal Conductivity W/(m-°C)	Dry Density (Mg/m^3)	Thermal Conductivity W/(m-°C)
2	0.31	0.29	0.31	0.34	0.30	0.43	0.30	0.52
50	-	-	0.39	0.40	0.45	0.43	-	-
100	0.50	0.40	0.51	0.44	0.52	0.50	0.47	0.58
200	0.59	0.44	0.57	0.45	0.61	0.53	0.57	0.57
300	0.66	0.42	0.62	0.49	0.66	0.54	0.63	0.71
400	0.70	0.48	0.66	0.54	0.71	0.76	0.68	0.83

Note: Hyphen indicates no test was conducted.

VII. Acknowledgements

The principal investigators acknowledge EREF for their financial support of this research and for the numerous landfill owners and their consultants who engaged with the research team during this project. Their insights and field observations helped to ensure that the project incorporated the latest information from full-scale landfills.

VIII. References

Abu-Hamdeh, N. Thermal properties of soils as affected by density and water content. *Biosyst Eng*. 2003, 86(1), 97-102.

Abu-Hamdeh, N., and Reeder, R. Soil thermal conductivity effects of density, moisture, salt concentration, and organic matter. *Soil Sci. Soc. Am. J.* 2000. 64(4), 1285-1290.

Ahmed, N., Wenzel, H., Hansen, J. B. Characterization of Shredder Residues Generated and Deposited in Denmark. *Waste Manage.* 2014, *34*, 1279–1288.

Amend, J. P., Shock, E. L. Energetics of Overall Metabolic Reactions of Thermophilic and Hyperthermophilic Archaea and Bacteria. *FEMS Microbiol. Rev.* 2001, *25*, 175–243.

Amestoy, P. R., Duff, I. S. and L'excellent, J. Y. Multifrontal parallel distributed symmetric and unsymmetric solvers. *Comput. Method. Appl. M.*, 2000, 184(2-4), 501-520.

Bareither, C., Breitmeyer, R., Benson, C., Barlaz, M., and Edil, T. Deer Track Bioreactor Experiment: Field-scale evaluation of municipal solid waste bioreactor performance, *J. Geotech. Geoenvironmental Eng.* 2012, 138(6), 658-670.

Benson, C. Characteristics of gas and leachate at an elevated temperature landfill, *Geotechnical Frontiers 2017, Waste Containment, Barriers, Remediation, and Sustainable Geoengineering, GSP No. 276*, ASCE, T. Brandon and R. Valentine, eds. 2017, 313-322.

Bott, M. and R.K. Thauer (1987). Proton-motive-force-driven formation of CO from CO2 and H2 in methanogenic bacteria. European Journal of Biochemistry 168(2), 407-412.

Breitmeyer, R., Benson, C., and Edil, T. Effect of changing unit weight and decomposition on unsaturated hydraulic properties of municipal solid waste In bioreactor landfills, *J. Geotech. Geoenvironmental Eng.* 2020,146(5): 04020021.

Bristow, K., Kluitenberg, G., and Horton, R. Measurement of soil thermal properties with a dual-probe heat-pulse technique, *Soil Sci. Soc. Am. J.* 1994, 58, 1288-1294.

Calder, G. V., Stark, T. D. Aluminum Reactions and Problems in Municipal Solid Waste Landfills. *Practice Periodical of Hazardous, Toxic, and Radioactive Waste Management* 2010, *14*, 258–265.

Ciuta, S., Patuzzi, F., Baratieri, M., Castaldi, M. J. Biomass Energy Behavior Study during Pyrolysis Process by Intraparticle Gas Sampling. *J. Anal. Appl. Pyrol.* 2014, *108*, 316–322.

de la Cruz, F. B. D. la, Barlaz, M. A. Estimation of Waste Component-Specific Landfill Decay Rates Using Laboratory-Scale Decomposition Data. *Environ. Sci. Technol.* 2010, *44*, 4722–4728.

Curtiss, C. F. and Hirschfelder, J. O. Integration of stiff equations. *Proc. Natl. Acad. Sci.*, 1952, 38(3), 235-243.

Dorez, G., Ferry, L., Sonnier, R., Taguet, A., and Lopez-Cuesta, J. M. Effect of Cellulose, Hemicellulose and Lignin Contents on Pyrolysis and Combustion of Natural Fibers." *J. Anal. Appl. Pyrol.*, 2014, 107, 323–331.

Eashwar, M., Subramanian, G., Chandrasekaran, P. Marine Fouling and Corrosion Studies in the Coastal Waters of Mandapam, India. *Bulletin Electrochem.* 1990, *6*, 699–702.

Eleazer, W. E., Odle, W. S., Wang, Y.-S., and Barlaz, M. A. Biodegradability of Municipal Solid Waste Components in Laboratory-Scale Landfills. *Environ. Sci. Technol.*, 1997, 31, 911–917.

El-Fadel, M., Findikakis, A. N., Leckie, J. O. Estimating and Enhancing Methane Yield from Municipal Solid Waste. *Hazard. Waste Hazard. Mater.* 1996a, *13*, 309–331.

El-Fadel, M., Findikakis, A., Leckie, J. Numerical Modelling of Generation and Transport of Gas and Heat in Sanitary Landfills II. Model Application. *Waste Management Res.* 1996b, *14*, 537–551.

El-Fadel, M., Findikakis, A., Leckie, J. Numerical Modelling of Generation and Transport of Gas and Heat in Landfills I. Model Formulation. *Waste Management Res.* 1996c, *14*, 483–504.

Ezuber, H., El-Houd, A., El-Shawesh, F. A Study on the Corrosion Behavior of Aluminum Alloys in Seawater. *Mater. Design* 2008, *29*, 801–805.

Faitli, J., Magyar, T., Erdélyi, A., and Murányi, A. Characterization of thermal properties of municipal solid waste landfills. *Waste Mgmt.*, 2015, 36, 213-221.

Fuchs, S, Schütz, F., Förster, H., and Förster, A. Evaluation of common mixing models for calculating bulk thermal conductivity of sedimentary rocks: Correction charts and new conversion equations, *Geothermics*. 2013, 47, 40-52.

Fytanidis, D. K., Voudrias, E. A. Numerical Simulation of Landfill Aeration Using Computational Fluid Dynamics. *Waste Manage.* 2014, *34*, 804–816.

Garg, A., Achari, G. A Comprehensive Numerical Model Simulating Gas, Heat, and Moisture Transport in Sanitary Landfills and Methane Oxidation in Final Covers. *Environ. Model. Assess.* 2010, *15*, 397–410.

Gawande, N., Reinhart, D. R., Yeh, G. T. Modeling Microbiological and Chemical Processes in Municipal Solid Waste Bioreactor, Part I: Development of a Three-Phase Numerical Model BIOKEMOD-3P. *Waste Manage.* 2010, *30*, 202–210.

Gholamifard, S., Duquennoi, C., Eymard, R. A Multiphase Model of Bioreactor Landfill with Heat and Gas Generation and Transfer. In *Eurotherm Seminar No. 81 Reactive Heat Transfer in Porous Media, Ecole des Mines d'Albi,* 2007.

Gholamifard, S., Eymard, R., Duquennoi, C. Modeling Anaerobic Bioreactor Landfills in Methanogenic Phase: Long Term and Short Term Behaviors. *Water Res.* 2008, *42*, 5061–5071.

Grillo, R. J. Energy Recycling-Landfill Waste Heat Generation and Recovery. *Current Sustainable/Renewable Energy Reports* 2014, *1*, 150–156.

Halder, A., Dhall, A. and Datta, A. K. Modeling transport in porous media with phase change: applications to food processing. *J. Heat Trans.*, 2011, 133(3), 031010.

Hanson, J.L., Liu, W.L. and Yesiller, N., 2008. Analytical and numerical methodology for modeling temperatures in landfills. In *GeoCongress* 2008: Geotechnics of Waste Management and Remediation (pp. 24-31).

Hanson, J. L., Yeşiller, N. and Oettle, N. K. Spatial and temporal temperature distributions in municipal solid waste landfills. *J. Environ. Chem. Eng.*, 2010, 136(8), 804-814.

Hanson, J. L., Yeşiller, N., Onnen, M. T., Liu, W. L., Oettle, N. K. and Marinos, J. A. Development of numerical model for predicting heat generation and temperatures in MSW landfills. *Waste Manage.*, 2013, 33(10), 1993–2000.

Hao Z, Sun, M., Ducoste J., Benson, C. Luettich, S., Castaldi, M, and Barlaz, M. Heat generation and accumulation in municipal solid waste landfills, *Environ. Sci. & Tech.* 2017, *51*, (21), 12434-12442.

Hao Z, Barlaz, M., Ducoste J. Finite Element Modeling of Landfills to Estimate Heat Generation, Transport and Accumulation, *J. Geotech. Geoenviron. Eng.,* 2020, *in revision.*

Hodge, K., Levis, J., deCarolis, J., and Barlaz, M. Systematic Evaluation of Industrial, Commercial, and Institutional Food Waste Management Strategies in the United States. *Environ. Sci. Technol.*, 2016, 50, 8444–8452.

Hosford, W. F. and Duncan, J. L. The Aluminum Beverage Can. *Sci. Am.*, 1994, 271, 48–53.

Hozumi, H. Theoretical Study on Heat Transport Phenomena in a Sanitary Landfill. In *Proceedings Sardinia 97, Sixth International Landfill Symposium*, 1997, 13–17.

Jafari, N. H., Stark, T. D., Thalhamer, T. Spatial and Temporal Characteristics of Elevated Temperatures in Municipal Solid Waste Landfills. *Waste Manage.* 2017, *59*, 286–301.

Khire, M. and Johnson, T. Thermal properties of municipal solid waste from landfills located in sub-humid and humid locations, *Proc. Global Waste Management Symposium*. 2018, Penton Media, New York.

Kwon, E. E., Castaldi, M. J. Urban Energy Mining from Municipal Solid Waste (MSW) via the Enhanced Thermo-Chemical Process by Carbon Dioxide (CO_2) as a Reaction Medium. *Bioresource Technol.* 2012, *125*, 23–29.

Levis, J. W. and Barlaz, M. A. Landfill Gas Monte Carlo Model Documentation and Results." Report to ICF for the U.S. EPA Waste Reduction Model (WARM), USEPA: Washington, D.C., 2014. http://www4.ncsu.edu/~jwlevis/Landfill_WARM-2014.pdf.

Li, H., Sanchez, R., Joe Qin, S., Kavak, H. I., Webster, I. A., Tsotsis, T. T., Sahimi, M. Computer Simulation of Gas Generation and Transport in Landfills. V: Use of Artificial Neural Network and the Genetic Algorithm for Short- and Long-Term Forecasting and Planning. *Chem. Eng. Sci.* 2011, *66*, 2646–2659.

Li, X., Bertos, M. F., Hills, C. D., Carey, P. J., Simon, S. Accelerated Carbonation of Municipal Solid Waste Incineration Fly Ashes. *Waste Manage.* 2007, *27*, 1200–1206.

Liang, P., Wang, Z. and Bi, J. Simulation of coal pyrolysis by solid heat carrier in a moving-bed pyrolyzer. *Fuel*, 2008, 87(4-5), 435–442.

Lopez, V. M., Florentino, B., and Barlaz, M. A. Chemical Composition and Methane Potential of Commercial Food Wastes. *Waste Manage.*, 2016, 56, 477–490.

Luettich, S. M., Yafrate, N. Measuring Temperatures in an Elevated Temperature Landfill. *Geo-Chicago* 2016, 162–176.

Miller, P. A. and Clesceri, N. L. Waste Sites as Biological Reactors: Characterization and Modeling. CRC Press, Florida, 2002.

Morales-Flórez, V., Santos, A., Romero-Hermida, I., Esquivias, L. Hydration and carbonation reactions of calcium oxide by weathering: kinetics and changes in the nanostructure. *Chem. Eng. J.* 2015, *265*, 194–200.

Nasirian, A., Cortes, D., and Dai, S. The physical nature of thermal conduction in dry granular media. *Géotechnique Letters*. 2015, 5,1-5.

Ng, C., Feng, S., Liu, H. A Fully Coupled Model for Water-Gas-Heat Reactive Transport with Methane Oxidation in Landfill Covers. *Sci. Total Environ.* 2015, *508*, 307–319.

Nielsen, H., Mladenovska, Z., Westermann, P., Ahring, B. K. Comparison of Two-Stage Thermophilic (68 °C/55 °C) Anaerobic Digestion with One-Stage Thermophilic (55 °C) Digestion of Cattle Manure. *Biotechnol. Bioeng.* 2004, *86*, 291–300.

Nozhevnikova, A., Kotsyurbenko, O., Parshina, S. Anaerobic Manure Treatment under Extreme Temperature Conditions. *Water Sci. Technol.* 1999, *40*, 215–221.

Neusinger, R., Drach, V., Ebert, H. P., Fricke, J. Computer Simulations That Illustrate the Heat Balance of Landfills. *Int. J. Thermophys.* 2005, *26*, 519–530

Oshins, C. and Block, D. Feedstock Composition at Composting Sites. *Biocycle*, 2000, 41, 31–34.

Rendek, E., Ducom, G. and Germain, P. Assessment of MSWI bottom ash organic carbon behavior: A biophysicochemical approach. *Chemosphere*, 2007, 67(8), 1582–1587.

Saad, Y. and Schultz, M. H. GMRES: A generalized minimal residual algorithm for solving nonsymmetric linear systems. *SIAM J. Sci. Comput.*, 1986, 7(3), 856-869.

Sanchez, R., Tsotsis, T. T., Sahimi, M. Computer Simulation of Gas Generation and Transport in Landfills. IV. Modeling of Liquid-Gas Flow. *Chem. Eng. Sci.* 2010, *65*, 1212–1226.

Shabani-Nooshabadi, M., Ghoreishi, S., Behpour, M. Electropolymerized Polyaniline Coatings on Aluminum Alloy 3004 and Their Corrosion Protection Performance. *Electrochim. Acta* 2009, *54*, 6989–6995.

Smart, N. R., Blackwood, D. J., Werme, L. *The Anaerobic Corrosion of Carbon Steel and Cast Iron in Artificial Groundwaters*, SKB Technical Report TR-01-22, Swedish Nuclear Fuel and Waste Management Co: Stockholm, 2001, pp 1-46.

Smith, C., Compton, K., Coley, F. Aerobic Marine Bacteria and the Corrosion of Carbon Steel in Sea-Water. *Corros. Sci.* 1973, *13*, 677–685.

Sosnowski, P., Wieczorek, A., Ledakowicz, S. Anaerobic Co-Digestion of Sewage Sludge and Organic Fraction of Municipal Solid Wastes. *Adv. Environ. Res.* 2003, *7*, 609–616.

Speiser, C., Baumann, T., Niessner, R. Morphological and Chemical Characterization of Calcium-Hydrate Phases Formed in Alteration Processes of Deposited Municipal Solid Waste Incinerator Bottom Ash. *Environ. Sci. Technol.* 2000, *34*, 5030–5037.

Staley, B. F. and Barlaz, M. A. Composition of Municipal Solid Waste in the United States and Implications for Carbon Sequestration and Methane Yield. *J. Environ. Eng.*, 2009, 135, 901–909.

Rees, J. F. Optimisation of Methane Production and Refuse Decomposition in Landfills by Temperature Control. *J. Chem. Technol. Biotechnol.* 1980, *30*, 458–465.

Rendek, E., Ducom, G., Germain, P. Assessment of MSWI bottom ash organic carbon behavior: A biophysicochemical approach. *Chemosphere* 2007, *67*, 1582–1587.

Rothfuss, F., Bender, M., Conrad, R. Survival and Activity of Bacteria in a Deep, Aged Lake Sediment (Lake Constance). *Microbial Ecol.* 1997, *33*, 69–77.

Trouve, A. and Minnich, T. Thermal properties database, Report submitted for Award Number 2008-DN-BX-K167 to the US Dept of Justice, Washington DC, 2012.

U.S. Packaging & Wrapping LLC. (2017). "Thickness of Aluminum Foil." <http://www.uspackagingandwrapping.com/blog/Thicknessof-Aluminum-Foil.html> (Apr. 09, 2017)

U.S. EPA, *Landfill Gas Emissions Model (LandGEM) Version 3.02 User's Guide*, U.S. Environmental Protection Agency: Washington, D.C., 2005, http://www.epa.gov/ttncatc1/dir1/landgem-v302-guide.pdf

U. S. EPA, *Compilation of Air Pollutant Emission Factors, AP-42, Volume 1: Stationary Point and Area Sources, 5th ed., Supplement E, Chapter 2.4: Municipal Solid Waste Landfills*, U.S. Environmental Protection Agency: Washington, D.C., 1998.

U.S. EPA. Municipal Solid Waste Generation, Recycling, and Disposal in the United States: Facts and Figures for 2013, United States Environmental Protection Agency: Washington, DC, 2015.

Van Brundt, M. E., Barlaz, M. A., Castaldi, M. J., Green, R., Lewis, T. and Dottellis, J., 2020, "Field Testing of Municipal Waste Combustor Ash for Heat Generation Potential," Global Waste Management Symposium, Feb. 24 – 26, Indian Wells, CA.

de Vries, D. Thermal properties of soils. In *Physics of Plant Environment*, W. van Wijk, ed. North-Holland Publishing Company, Amsterdam.1963, 210-235.

Wang, X., Padgett, J. M., de la Cruz, F. B., and Barlaz, M. A. Wood Biodegradation in Laboratory-Scale Landfills. *Environ. Sci. Technol.*, 2011, 45, 6864–6871.

Wang, X., Padgett, J. M., Powell, J. S., and Barlaz, M. A. Decomposition of Forest Products Buried in Landfills." *Waste Manage.*, 2013, 33, 2267–2276.

Wang, X. and Barlaz, M. A. Decomposition and Carbon Storage of Hardwood and Softwood Branches in Laboratory-Scale Landfills. *Sci. Total Environ.*, 2016, 557, 355–362.

White, J., Robinson, J., Ren, Q. Modelling the Biochemical Degradation of Solid Waste in Landfills. *Waste Manage.* 2004, *24*, 227–240.

Yeşiller, N., Hanson, J.L. and Yee, E.H. Waste heat generation: A comprehensive review. *Waste Manage.*, 2015, 42, 166-179.

Yeşiller, N., Hanson, J., Kopp, K., and Yee, E. Heat management strategies for MSW landfills, *Waste Mgmt.* 2016, 56, 246–254.

Yoshida, H. and Rowe, R. Consideration of landfill liner temperature. *Proc. Sardinia 2003, Ninth International Waste Management and Landfill Symposium*, Christensen, T. et al. eds., CISA, Italy, 2003.

Yoshida, H., Tanaka, N. and Hozumi, H. Theoretical study on heat transport phenomena in a sanitary landfill. In Proc., 6th Int. Landfill Symp, Vol. 1, Calgiari, Italy, 1997, 110-119.

Zinder, S., Anguish, T., Cardwell, S. Effects of Temperature on Methanogenesis in a Thermophilic (58 °C) Anaerobic Digestor. *Appl. Environ. Microbiol.* 1984, *47,* 808–813.

IX. Appendices

A. List of Related Publications

Peer-Reviewed Articles

Luettich, S.M. and Yafrate, N.J., "Measuring Temperatures in an Elevated Temperature Landfill", American Society of Civil Engineers (ASCE) Special Publication *Proceedings for Geo-Congress,* Chicago, August 2016.

Hao, Z., Sun, M., Ducoste, J. J., Benson, C. H., Luettich, S., Castaldi, M. J. and M. A. Barlaz, 2017, "Heat Generation and Accumulation in Municipal Solid Waste Landfills *Env. Sci. & Technol.*, 51, p. 12434 – 42.

Benson, C. (2017), Characteristics of Gas and Leachate at an Elevated Temperature Landfill, *Geotechnical Frontiers 2017, Waste Containment, Barriers, Remediation, and Sustainable Geoengineering, GSP No. 276*, ASCE, T. Brandon and R. Valentine, eds., 313-322.

Hao, Z., Sun, M, Ducoste, J. and M. A. Barlaz (2017), A Model to Describe Heat Generation and Accumulation at Municipal Solid, *Geotechnical Frontiers 2017, Waste Containment, Barriers, Remediation, and Sustainable Geoengineering, GSP No. 276*, ASCE, T. Brandon and R. Valentine, eds.

Hao, Z., Barlaz, M. A. and J. J. Ducoste, 2020, "Finite Element Modeling of Landfills to Estimate Heat Generation, Transport and Accumulation, *J Geotech. Geoenviron. Engr.* in revision.

Tian, K. and Benson, C. 2020, Thermal Properties of Municipal Solid Waste, *J Geotech. Geoenviron. Engr.* in review.

Tupsakhare, S., Moutushi, T., Castaldi, M.J., Barlaz, M.A., Luettich, S. and Benson, C.H., 2020, The Impact of Pressure, Moisture and Temperature on Pyrolysis of Municipal Solid Waste under Simulated Landfill Conditions and Relevance to the Field Data from Elevated Temperature Landfill," *Science of the Total Environment*, 723, 138031.

Moutushi, Tasnuva, Swanand S. Tupsakhare, and Marco J. Castaldi. "Abiotic decomposition of municipal solid waste under elevated temperature landfill conditions." Science of The Total Environment 823 (2022): 153685.

<u>Conference Presentations and Workshops</u>

Luettich, S., "Elevated Temperature Landfills – Challenges for Civil and Environmental Engineers", Presentation to Boston Society of Civil Engineers at Northeastern University, April 2017.VA DEQ – 2016

Hao, Z., Sun, M., Ducoste, J., Luettich, S., Castaldi, M., Benson, C. H. and M. A. Barlaz, 2016, "Understanding and Predicting Temperatures in Municipal Solid Waste Landfills," Global Waste Management Symposium, Indian Wells, CA, January 31 - February 3.

Barlaz, M. A., "A Model to Describe Heat Generation and Accumulation in Municipal Solid Waste Landfills," US EPA Workshop on Understanding Heat Generation at Municipal Solid Waste Landfills, April 19-20, 2017, Cinc. OH.

Luettich, S., "The Importance of Knowing How Temperatures are Measured in Elevated Temperature Landfills (ETLFs), Presentation at USEPA Roundtable Meeting on

Understanding Elevated Temperatures at Municipal Solid Waste Landfills", Cincinnati, Ohio, April 2017.

Barlaz, M. A., "A Model to Describe Heat Accumulation at Municipal Solid Waste Landfills," University of Toronto, Sept. 12, 2017.

Luettich, S., Yafrate, N., "Elevated Temperatures in Landfills – Challenges Facing the Solid Waste Community", Presentation to Solid Waste Association of North America (SWANA) - Southern New England Chapter, Oct 2017.

Hao, Z., Sun, M, Ducoste, J. and M. A. Barlaz (2017), A Model to Describe Heat Generation and Accumulation at Municipal Solid, Geotechnical Frontiers 2017, Waste Containment, Barriers, Remediation, and Sustainable Geoengineering, GSP No. 276, ASCE, T. Brandon and R. Valentine, eds.

Tupsakhare, S., Moutushi, T., Castaldi, M.J., Barlaz, M.A., Luettich, S. and Benson, C.H., Pyrolytic reactions in municipal solid waste landfills: Theory, Experiment and Connection to Field Observations, Global Waste Management Symposium, Indian Wells, CA Feburary 25, 2018

Hao, Z., Ducoste, J. and M. A. Barlaz, 2018, "Heat Generation and Accumulation in Municipal Solid Waste Landfills," Global Waste Management Symposium, Indian Wells, CA, February 11 - 14.

Yafrate, N., Luettich, S., Varsho, J., Davis, G., 2018, Elevated Temperature Landfills (ETLFs) – Temperature and Pressure Monitoring Instrumentation, Global Waste Management Symposium, Indian Wells, CA, February 11 - 14.

Barlaz, M. A. and C. H. Benson, "Biological and Chemical Reactions Contributing to Heat Generation in Landfills: Current Research and Model Simulations," Elevated Temperature Landfill Workshop, Nov. 7, 2018, Env. Research and Edcn. Fndn., Columbus, OH.

Barlaz, M. A. and N. Jafari, "Laboratory testing for Heat Generation Potential and Applications to Field Conditions," Elevated Temperature Landfill Workshop, Nov. 7, 2018, Env. Research and Edcn. Fndn., Columbus, OH.

Hao, Z., Ducoste, J. and M. A. Barlaz, 2020, "A Finite Element Model Describes Heat Generation, Transport, and Accumulation in Elevated Temperature Landfills," Global Waste Management Symposium, Feb. 24 – 26, Indian Wells, CA. (Top student poster award)

Marco J. Castaldi, Swanand Tupsakhare, Tasnuva Motoushi, Energy Analysis of Elevated Temperature Landfill Processes at the Laboratory Scale, Global Waste Management Symposium, Indian Wells, CA Feburary 25, 2020

Swanand Tupsakhare, Tasnuva Moutushi, Marco J. Castaldi, Pyrolytic Reactions in MSW Landfills: Theory, Experiment & Connections to Field Observations, 4th MatER Meeting "Innovation & Technologies in Waste Recovery", May 27-28, Piacenza, Italy

Tasnuva Moutushi, Swanand Tupsakhare, Marco J. Castaldi; Abiotic and Oxygen-Free Pyrolytic Decomposition of Municipal Solid Waste under Elevated Temperature Landfill Conditions, 9th International Conference on Engineering for Waste and Biomass Valorisation, June 27-30, 2022 Copenhagen, Denmark

Webinars

Luettich, S., Barlaz, M., Benson, C. H and Castaldi, M., Elevated Temperature Landfills, what do We Currently Know/What Still Needs to be Defined, June 2015

Luettich, S., Barlaz, M., Benson, C. H and Castaldi, M., Exothermic Reactions in elevated Temperature Landfills: Field Observations & Laboratory Experiments, December 14, 2016.

Trade Magazine Articles

Barlaz, M., Benson, C., Castaldi, M., and Luettich, S. (2016), Diagnosing and Understanding Elevated Temperature Landfills, Part 1 - Characteristics and Management Challenges, *Waste360*, Penton Media, New York.

Barlaz, M., Benson, C., Castaldi, M., and Luettich, S. (2017), Diagnosing and Understanding Elevated Temperature Landfills, Part 2 – Biological Reactions, *Waste360*, Penton Media, New York.

Barlaz, M., Benson, C., Castaldi, M., and Luettich, S. (2017), Diagnosing and Understanding Elevated Temperature Landfills, Part 3 – Chemical Reactions, *Waste360*, Penton Media, New York.

Yafrate, N., Luettich, S., "Elevated Temperature Landfills (ETLFs) – Challenges Facing the Solid Waste Community", em Magazine, Air & Waste Management Association (A&WMA), March 2017, pp. 18-23.

B. Previous models on heat generation in landfills

Table A1. Previous models on heat generation in landfills

Reference	Description
El-Fadel et al. (1996b)	• Described heat generation rate by incorporating a kinetic expression into a gas generation-microbial growth model • Assumed a proportional relationship between heat generation rate and acetic acid formation rate
El-Fadel et al. (1996c)	• Predicted methane production in consideration of biochemical and temperature feedback loops • Landfill temperature appears to be controlled by 1) total gas generation at specific depths; and 2) the imposed boundary condition at the landfill surface
Yoshida and Hozumi (1997)	• Developed a 1-D model to simulate the temperature distribution in a landfill • Incorporated heat transport and generation from biological decomposition • Predicted temperatures of ~70 ºC caused by anaerobic biodegradation • Methane production was affected by temperature
Gholamifard et al. (2007)	• Developed a moisture-dependent biodegradation model • Simulated temperatures in a lab-scale bioreactor landfill with leachate recirculation • The calculation of heat generation rate was based on the methane production rate • Demonstrated an initial decrease in temperature with leachate injection, but was unable to predict the sharp rise in temperature thereafter • The additional heat generation was hypothesized to be related to aerobic biodegradation
Gholamifard et al. (2008)	• Developed a coupled biological and heat transport model • Predicted a vertical gradient of 1−10 °C/m between different layers • The maximum temperature in the deepest layer was 55 °C
Neusinger et al. (2005)	• Simulated the thermal behavior of landfills by coupling heat and gas transfer • Heat generation from biochemical reactions • Heat transport in the solid matrix and heat transfer between fluids and the solid phase were not considered • The maximum temperatures (in the center of the landfill) was ~80 °C

Table A1. Previous models on heat generation in landfills (Continued)

Reference	Description
Gawande et al. (2010)	• Developed a generalized biochemical process model BIOKEMOD-3P • Simulated bioreactor landfill operation in a completely mixed condition • The heat generation rate was related to biological reactions
Garg and Achari (2010)	• Developed a model to simulate gas, heat, and moisture transport through a landfill • Heat generation was related to the methane production and consumption rates • Gas generation and transport equations were coupled to a heat balance
Ng et al. (2015)	• Developed a model that incorporated water-gas-heat coupled reactive transport in unsaturated soil • Included a proportional relationship between heat generation rate and methane oxidation rate • Incorporated heat convection, heat conduction, and heat source from methane oxidation

C. Additional results of simulations of the FEM-3DM

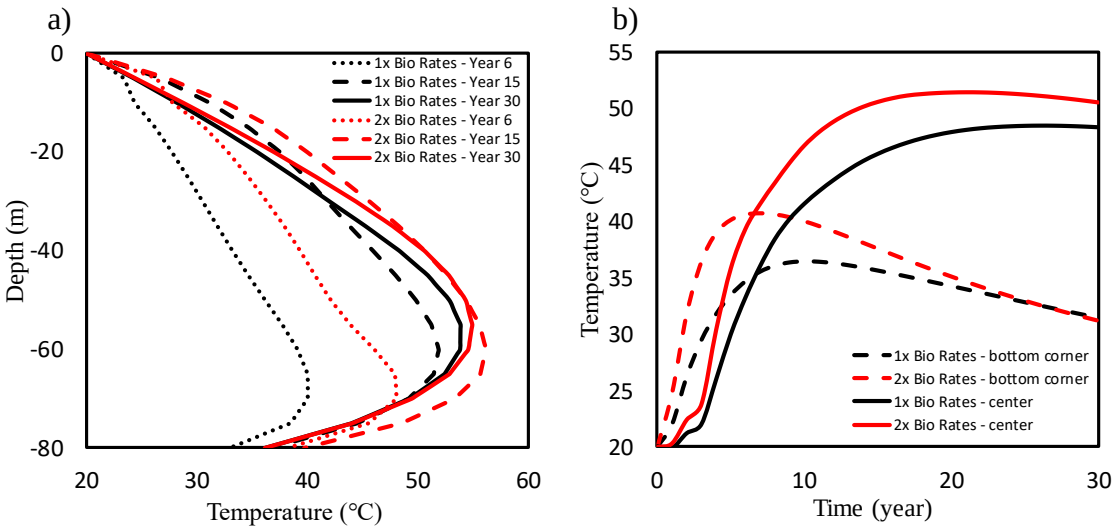

Figure A1. Temperature profiles and evolution for MSW only with doubled decay rates. A. vertical profiles in the center; b. temperature evolution at the geometric center of the landfill.

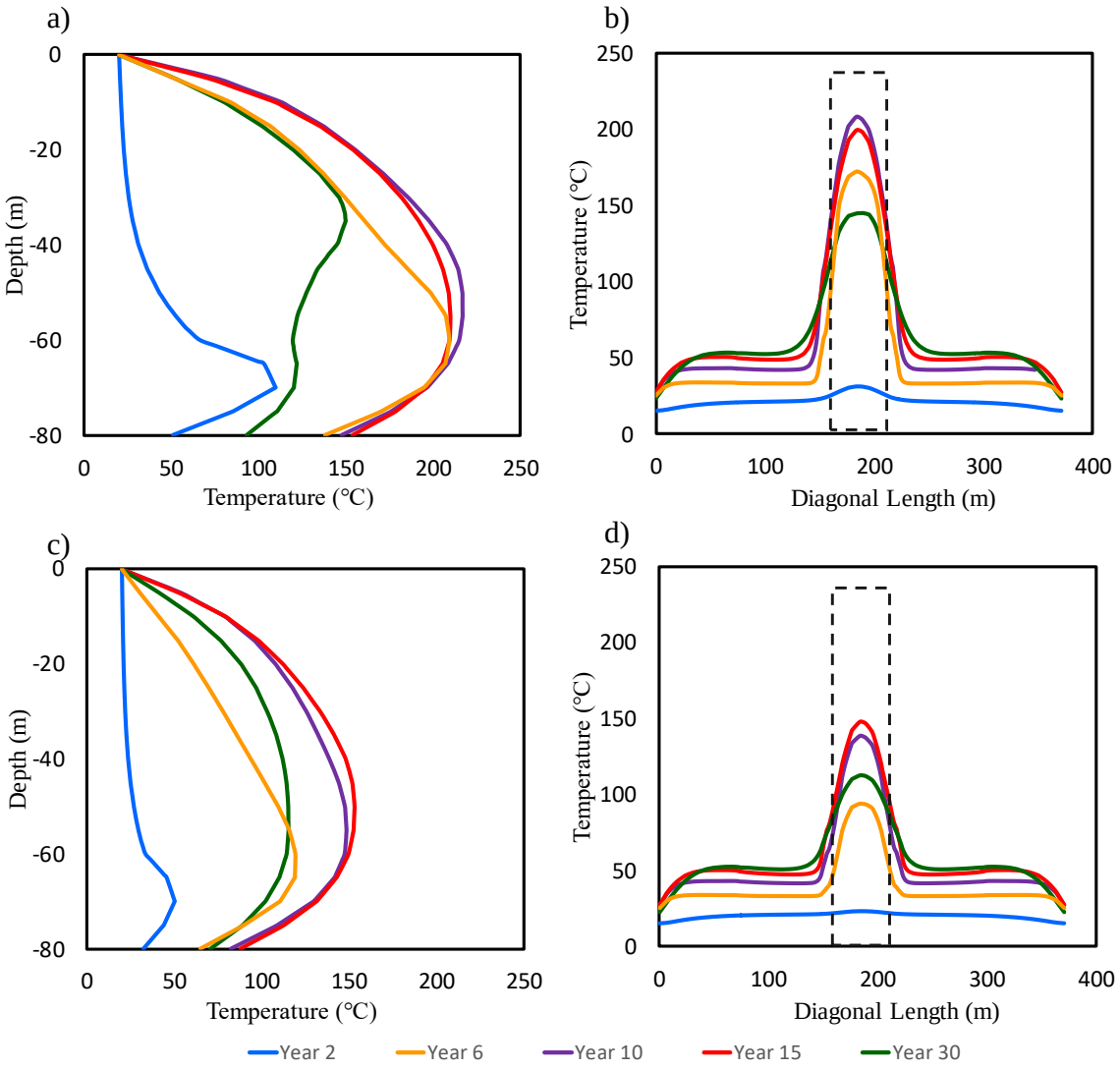

Figure A2. Temperature profiles for a landfill with an ash column (dashed line) in the center (a and b: hydration and carbonation; c and d: carbonation only. a. and c. vertical profiles in the center of the landfill; b. and d. horizontal profiles at 40 m in the diagonal cross section)

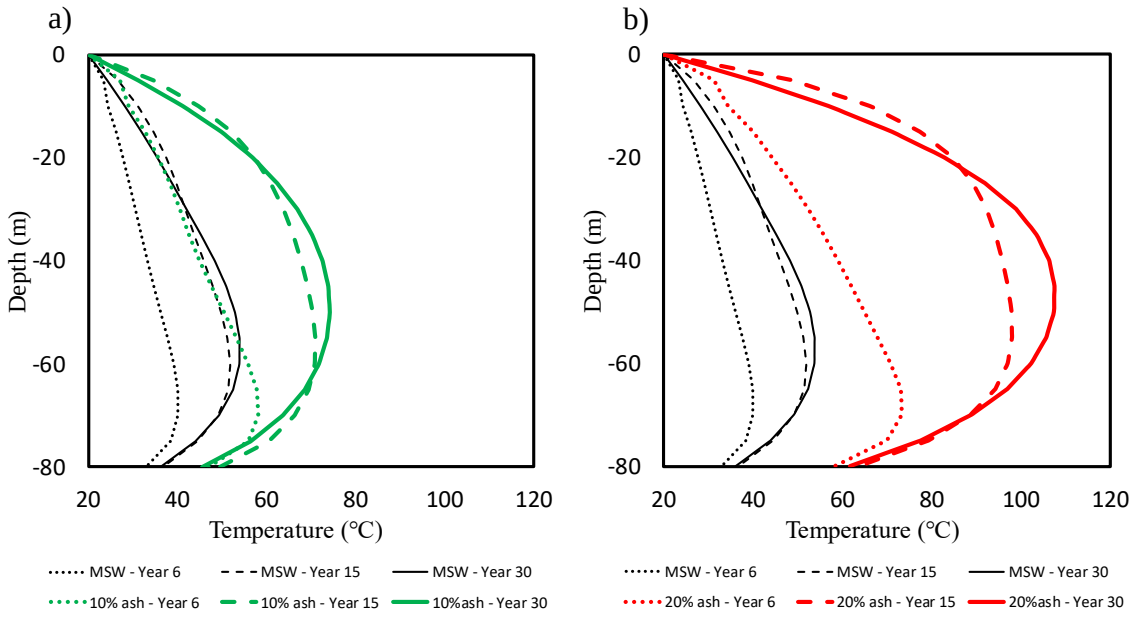

Figure A3. Temperature profiles for 10% (a) and 20% (b) ash-MSW mixtures

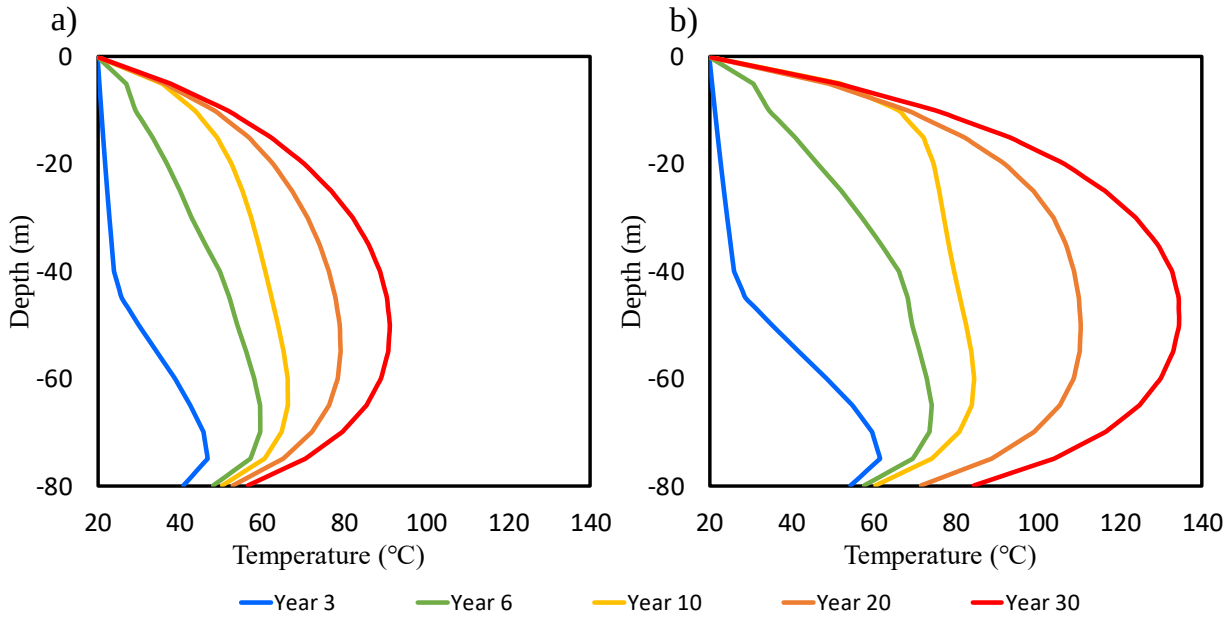

Figure A4. Temperature profiles for Al-MSW mixture with 1.7 % (a) and 3.4% (b) Al

D. Supplemental Information to Document Model Development

Temperature Inhibition function used in batch reactor model.

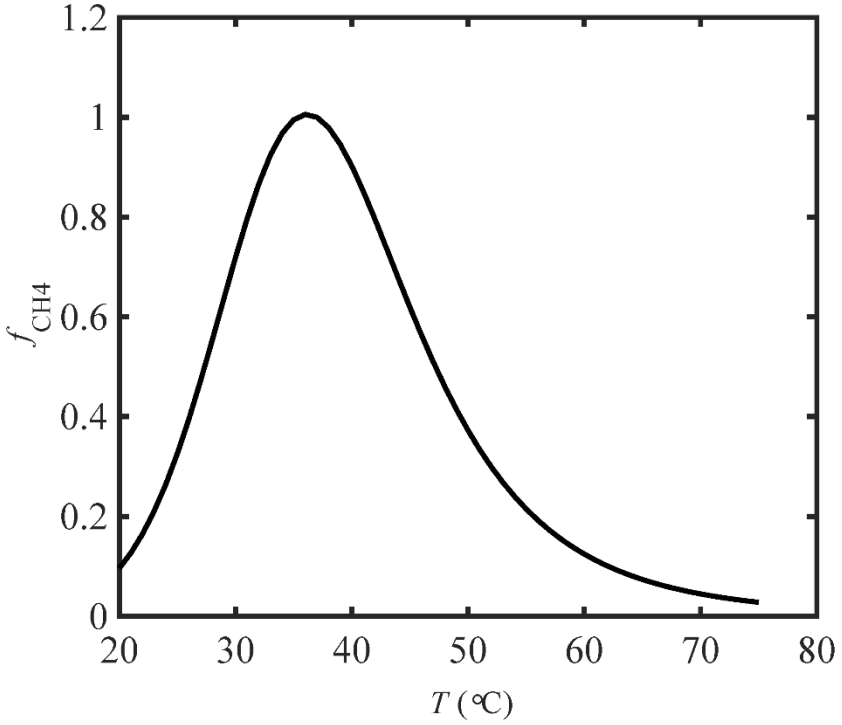

Figure A5. Inhibition function described in Eq. A1.

$$f_{CH_4}(T) = 4\frac{T^6}{K_T^6+T^6}\frac{K_T^7}{K_T^7+T^7} \quad \text{(A1)}$$

where T is temperature and K_T is a constant (37 ºC). The inhibition function is 1 at 37 ºC and diminishes as the temperature increases.

Hydration reactions of the oxides in ash

$$MgO + H_2O \rightarrow Mg(OH)_2 \qquad \Delta H = -933\frac{kJ}{kg\ MgO} \quad \text{(A2)}$$

$$Na_2O + H_2O \rightarrow 2NaOH \qquad \Delta H = -2484\frac{kJ}{kg\ Na_2O} \quad \text{(A3)}$$

$$K_2O + H_2O \rightarrow 2KOH \qquad \Delta H = -2173\frac{kJ}{kg\ K_2O} \quad \text{(A4)}$$

$$P_2O_5 + 3H_2O \rightarrow 2H_3PO_4 \quad \Delta H = -1445 \frac{kJ}{kg\ P_2O_5} \tag{A5}$$

Carbonation reactions of the hydroxides

$$Mg(OH)_2 + CO_2 \rightarrow MgCO_3 + H_2O \quad \Delta H = -1390 \frac{kJ}{kg\ Mg(OH)_2} \tag{A6}$$

$$2NaOH + CO_2 \rightarrow Na_2CO_3 + H_2O \quad \Delta H = -2112 \frac{kJ}{kg\ NaOH} \tag{A7}$$

$$2KOH + CO_2 \rightarrow K_2CO_3 + H_2O \quad \Delta H = -1704 \frac{kJ}{kg\ KOH} \tag{A8}$$

Characteristics of aluminum and ferrous metal considered in model

Table A2. Average thicknesses of metals from containers and other sources

Product Category	Percent of Metal (%)	Thickness (mm)	Coated Side	Alloy Type
Al containers[a]	25[b]	0.076[c]	1	3004
Al foils and closures	15[b]	0.016[d]	0	1100
Other Al[e]	60[b]	0.85[f]	0	3004
Fe containers	5[g]	0.32[h]	1	Steel
Other Fe[i]	95[g]	0.75[j]	0	Steel

a. Al containers include beer, soft drink and other cans.
b. Weight percent of total Al discards from the U.S. EPA (2015).
c. Data were obtained from Hosford and Duncan (1994).
d. Data were obtained from U.S. Packaging & Wrapping LLC (2017).
e. Other Al includes durable/nondurable goods and other Al sources.
f. The value is the average thickness of commercial embossed coated Al sheet for refrigerator inner panels.
g. Weight percent of total Fe discards from the U.S. EPA (2015).
h. The value is the average thickness of steel cans from ArcelorMittal.
i. Other Fe includes durable goods and other Fe sources.
j. The value is the average thickness of steel pre-coated sheets for home appliances.

Governing Equations for FEM-3DM

Gas phase balance

The reactions and transport of the gas phase by diffusion and convection are calculated using Eq. A9 to A11.

$$\varepsilon \frac{\partial c_{g,i}}{\partial t} + \boldsymbol{u_g} \cdot \nabla c_{g,i} = \nabla \cdot \left(D_i \nabla c_{g,i}\right) + S_{g,i} \quad \text{(A9)}$$

where ε is the porosity, $c_{g,i}$ is the concentration of gas species i (i = CH_4, CO_2, and H_2O), $\boldsymbol{u_g}$ is the gas phase velocity defined by Darcy's Law (Eqs. A11 and A12), D_i is the diffusion coefficient of gas species i, S_{g,CH_4} and S_{g,CO_2} are the source/sink term of reactions of gas species i, which is estimated using a modified version of the US EPA's LandGem model that incorporates waste-specific methane production potentials and decay rates as described in Eq. 6-8 (US EPA 2005 and 2015; Hao et al. 2017). S_{g,H_2O} is the amount of water that evaporates into the gas phase or condenses into the water phase as described in Eq. A10 (Halder et al. 2011).

$$S_{g,H_2O} = \varepsilon K_{evap}(a_{H_2O} c_{sat} - c_{g,H_2O}) \quad \text{(A10)}$$

The gas phase velocity is calculated based on Darcy's Law as shown in Eqs. A11 and A12.

$$\rho_g \nabla \cdot \left(\boldsymbol{u_g}\right) = \sum_{i=CH_4,CO_2,N_2} M_i S_{g,i} \quad \text{(A11)}$$

$$\boldsymbol{u_g} = -\frac{\eta}{\mu_g} \nabla P \quad \text{(A12)}$$

where ρ_g is the density of the gas phase, M_i is the molecular weight of gas species i, η and μ_g are the permeability of MSW and viscosity of the gas phase, respectively, and P is pressure.

Liquid Phase Balance

Infiltrated water balance

The model formulation assumes that there is no water accumulation and that infiltrated water is continuously removed by the leachate collection system.

Intrinsic moisture balance

To simulate evaporation and condensation, the vapor balance equation (Eq. A9) is coupled with the balance equation of intrinsic moisture given by Eq. A13, assuming that there is no exchange between the infiltrated and intrinsic moisture.

$$(1-\varepsilon)\frac{\partial c_{H_2O(iw)}}{\partial t} = \nabla \cdot \left(D_{H_2O(iw)} \nabla c_{H_2O(iw)}\right) - \varepsilon K_{evap}(a_{H_2O} c_{sat} - c_{H_2O(g)}) \quad \text{(A13)}$$

where $c_{H_2O(iw)}$ and $D_{H_2O(iw)}$ are the concentration and diffusion coefficient of intrinsic moisture in the waste, respectively. When the current vapor concentration, c_{g,H_2O}, is less

than the saturated vapor concentration at local temperature $a_{H_2O}c_{sat}$, evaporation occurs. Condensation occurs when $a_{H_2O}c_{sat}$ is greater than c_{g,H_2O}.

Solid (reactive wastes) Balance

The consumption of biodegradable waste and ash hydration/carbonation is described by first order reactions (Eq. A14) and the rate of Al corrosion is expressed in Eq. 6-15.

$$\frac{\partial c_{s,i}}{\partial t} = -\sum_{\substack{i=MSW,\\ ash}} R_{s,i}\, c_{s,i} \qquad \text{(A14)}$$

where $c_{s,i}$ and $R_{s,i}$ are the concentration and reaction rate of component *i*, respectively. The parameters of waste composition and characteristics are given in Tables 6-2 to 6-4, and ash and metal characteristics are given in Tables 6-5 and A2, respectively.

Heat balance

The landfill system heat balance is given by Eq. A15. The first and second terms on the left side of Eq. A15 describe heat accumulation and convective heat loss, respectively. The first and second terms on the right side represent heat conduction and heat source/sink terms due to chemical reactions, and evaporation and condensation.

$$\left[(1-\varepsilon)\rho_s C_{ps} + \varepsilon\rho_f C_{pf}\right]\frac{\partial T}{\partial t} + (\rho_f C_{pf} u_f)\nabla T = \nabla\{\left[(1-\varepsilon)\kappa_s + \varepsilon\kappa_f\right]\nabla T\} + \sum_{\substack{i=bio,\\ chem,\\ condens.}} Q_i \qquad \text{(A15)}$$

where ρ_s, C_{ps}, and κ_s are the density, heat capacity, and thermal conductivity of the solid phase, ρ_f, C_{pf}, and κ_f are the density, heat capacity, and thermal conductivity of the infiltrated phase, T is temperature, and Q_i includes the heat source/sink terms of evaporation and condensation, and biotic and abiotic reactions. The impact of gas transfer on temperature (convection and conduction) is negligible compared to the liquid and solid phases as $\rho_f C_{pf}$ is four orders of magnitude greater than $\rho_g C_{pg}$.

The source/sink terms of heat and mass balance equations

The methods to calculate CH_4 generation and substrate biodegradation rates are the same as those described for the batch reactor model and presented in the main body of the report. However, an updated temperature inhibition function was adopted for use with the FEM-3DM based on the availability of additional experimental data.

To account for the influence of temperature on CH_4 generation, an inhibition function, $f_{CH_4}(T)$, was developed based on the normalized experimental CH_4 potential of waste

samples obtained from an actual landfill (unpublished data). The fitted inhibition function and the normalized experimental data are shown in Eq. A16 and Figure A6.

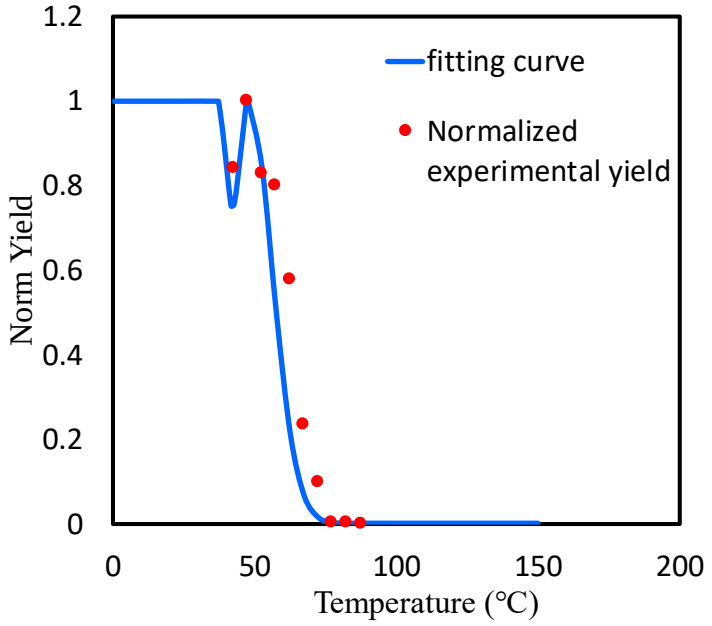

Figure A6. Inhibition function and normalized experimental CH_4 potential described in Eq. A16

$$f_{CH_4}(T) = \begin{cases} 1 & T < 37℃ \\ \dfrac{1}{\left\{e^{\left[-\left(\frac{36.4-47.5}{5.7}\right)^2\right]}+1\right\}}\left\{e^{\left[-\left(\frac{T-47.5}{5.7}\right)^2\right]}+e^{\left[-\left(\frac{T-36.4}{5.62}\right)^2\right]}\right\} & 37℃ \le T \le 47.5℃ \\ e^{\left[-\left(\frac{T-47.5}{12}\right)^2\right]} & T > 47.5℃ \end{cases} \quad \text{(A16)}$$

The heat gain/loss due to condensation and evaporation (phase change, Q_{PC}) is estimated using Eq. A17

$$Q_{PC} = -\Delta H_{vap} K_{evap} (a_{H_2O} c_{sat} - c_{H_2O(g)}) \quad \text{(A17)}$$

where ΔH_{vap} is the enthalpy of phase change of water.

During the waste burial period, the landfill working surface is exposed to the atmosphere. The exposure leads to an additional heat loss mechanism due to gas convection (Eq. A18).

$$Q_{conv\_air} = \begin{cases} -\frac{A_{cell}}{V_{cell}} h_{air} (T - T_{atm}) & \text{cells exposed to the atmosphere} \\ 0 & \text{other cells} \end{cases} \quad \text{(A18)}$$

where Q_{conv_air} is the heat loss rate due to air convection, A_{cell} and V_{cell} are the surface area and volume of the cell exposed to the atmosphere, h_{air} is the estimated convective heat transfer coefficient of air, and T_{atm} is the atmospheric temperature (default of 20 ℃).

Boundary and initial conditions

The domain and boundaries that applied in the model are illustrated in Figure A7. Figure A7a displays the domain of the landfill, which is used in the initial and source/sink terms of heat and mass transfer processes. Figures A7b to A7d are the specific boundaries for heat balance equations and are also no-flow boundaries for the mass balance equations. Figure A7e displays the surface of the gas wells which is used for the boundary conditions of heat and mass transfer related to gas wells.

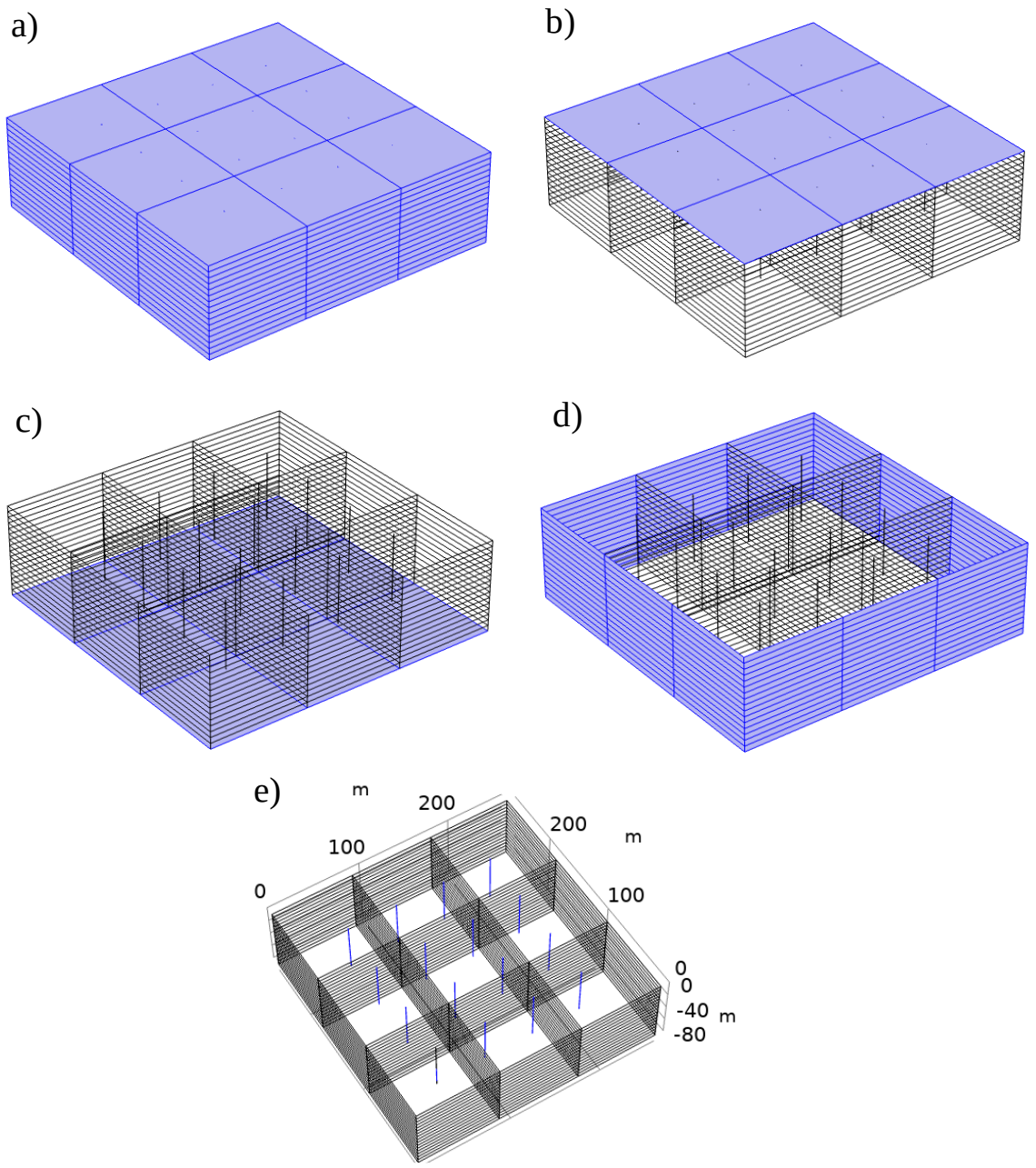

Figure A7. Domain and boundaries applied in the model. Vertical gas wells are illustrated in the center of each cell.

Initial conditions

For Darcy's equation, the initial pressure is defined as atmospheric pressure. A uniform initial temperature (20 °C) and uniform gas, water and solid initial concentrations are assumed throughout the landfill domain (Figure A7a) and the expressions are described by Eqs. A19 to A21.

$$c_{g,i}(x, y, z, 0) = 0 \qquad \text{(A19)}$$

$$c_{H_2O(iw)}(x,y,z,0) = \frac{\omega\rho_w}{M_w} \quad \text{(A20)}$$

$$c_{s,i}(x,y,z,0) = c_{s,i,0} \quad \text{(A21)}$$

where $c_{H_2O(iw)}$ is the concentration of intrinsic moisture in the waste, ρ_w and M_w are the density and molecular weight of water, respectively, and $c_{s,i,0}$ is the initial concentration of biodegradable substrate component *i*.

Boundary conditions for the mass balance equations

The landfill surface boundaries (Figures A7b to A7d) are no-flux boundaries for the gas, liquid and solid phases as described by Eqs. A22 to A24. For the gas balance equation (Eq. A9), LFG can only be transported out from the gas well surface boundary (Figure A7e) as shown in Eq. A25.

$$-\mathbf{n}\cdot(-D_{g,i}\nabla c_{g,i}) = 0 \quad \text{(A22)}$$

$$-\mathbf{n}\cdot(-D_{H_2O(iw)}\nabla c_{H_2O(iw)}) = 0 \quad \text{(A23)}$$

$$-\mathbf{n}\cdot(-D_{s,i}\nabla c_{s,i}) = 0 \quad \text{(A24)}$$

$$-\mathbf{n}\cdot(-D_{g,i}\nabla c_{g,i}) = k_{c,i}(c_{ext,g,i} - c_{g,i}) \quad \text{(A25)}$$

In Eqs. A22 to A25, **n** is the outward normal vector, $k_{c,i}$ is the mass transfer coefficient for convection which is equal to the LFG removal velocity defined in Eq. A26, and $c_{ext,g,i}$ is the concentration of gas species *i* (*i* = CH_4, CO_2, and $H_2O_{(g)}$) as it leaves the landfill. Since the LFG removal rate is equal to the LFG generation rate, the magnitude of the gas well velocity vector is estimated from Eq. A26.

$$u_{GW} = -22.4[L/mol]\frac{V_{LF}}{A_{GW}}\sum_{\substack{i=CH_4,\\ CO_2,\\ N_2}} S_{g,i} \quad \text{(A26)}$$

where u_{GW} is the magnitude of the gas well velocity vector, V_{LF} is the landfill volume, and A_{GW} is the total surface area of gas wells.

For the Darcy's equation (Eqs. A11 and A12), an outlet boundary condition is applied to the gas well surface boundary (Figure A7e) and the expression is given in (Eq. A27). An atmospheric pressure boundary condition is applied on the top boundary (Figure A7b).

$$-\mathbf{n}\cdot\boldsymbol{u_g} = -u_{GW} \quad \text{(A27)}$$

The negative velocity on the right side of Eq. A27 denotes that the LFG flows out of the landfill domain.

Boundary conditions for the heat balance equation

The top boundary of the landfill (Figure A7b) is exposed to the atmosphere with a constant temperature (20 ℃). Assuming the landfill domain is beneath the earth surface, a convective heat flux boundary condition (Eq. A28) is applied to the side and bottom boundaries (Figures A7c and A7d). The side and bottom boundaries are defined by a soil temperature that is 5 m outside of the landfill domain.

$$-\mathbf{n} \cdot \left[(1-\varepsilon)\kappa_s + \varepsilon\kappa_f\right]\nabla T = h_{soil}(T_{soil} - T) \tag{A28}$$

where h_{soil} is the heat transfer coefficient defined in Eq. A29, and T_{soil} is the soil temperature 5 m from the side and bottom boundaries (default of 15 ℃).

The heat transfer coefficient of the soil layer (h_{soil}) is estimated using Eq. A29

$$h_{soil} = \frac{\kappa_{soil}}{l_{soil}} \tag{A29}$$

where κ_{soil} is the thermal conductivity of soil and l_{soil} is the thickness of the soil layer.

An outflow boundary condition is used to describe the removal of heat from the gas well surface (Figure A7e), given by Eq. A30. Convection is assumed to be the only heat transfer mechanism occurring across the gas well surface boundary.

$$-\mathbf{n} \cdot \left[(1-\varepsilon)\kappa_s + \varepsilon\kappa_f\right]\nabla T = 0 \tag{A30}$$

Mesh/solvers utilized in the model

The governing partial differential equations for mass and heat transfer were discretized and solved by the nonlinear solvers provided in COMSOL Multiphysics^{TM} 5.4 software package. Non-uniform tetrahedral-triangle mesh elements with different mesh sizes were applied, with greater mesh densities near the gas wells to capture the thin mass and heat boundary layers close to edges. The finer mesh can compute gradients in state variables being tracked by the model. Model simulations were performed to represent a 30-year period (1-year intervals) by a time-dependent solver with the BDF (Backward Differentiation Formula) method (Curtiss and Hirschfelder, 1952). The discretized linear systems were solved by direct methods MUMPS (MUltifrontal Massively Parallel Sparse direct solver) (Amestoy et al., 2000) and GMRES (Generalized Minimum RESidual) iterative methods (Saad and Schultz, 1986). Each simulation required four days on a Dell workstation with 128 GB RAM and an Intel Xeon Gold 5122 CPU.